Technische Universität Berlin

Institut für
Werkstoffwissenschaften
und -technologien

- Metallphysik -

René Valéry Martins

Experimental Investigation of Plastically Deformed Al-Alloy Samples Using High Energy Synchrotron Radiation

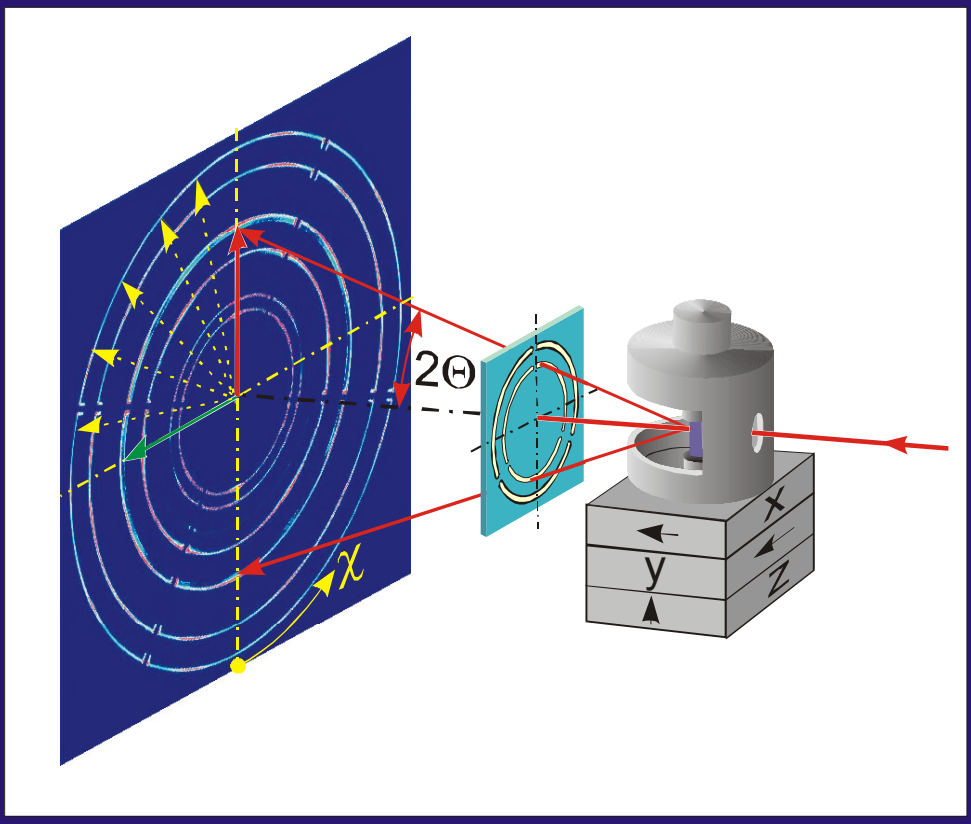

Experimental Investigation of Plastically Deformed Al-Alloy Samples Using High Energy Synchrotron Radiation

Experimental Investigation of Plastically Deformed Al-Alloy Samples Using High Energy Synchrotron Radiation

von
Diplom-Ingenieur
René Valéry MARTINS
aus Berlin

Von der Fakultät III
-Fakultät für Prozesswissenschaften-
der Technischen Universität Berlin
zur Erlangung des akademischen Grades

Doktor der Ingenieurwissenschaften
-Dr.-Ing.-

genehmigte Dissertation

Promotionsausschuss:

Vorsitzender:	Prof. Dipl.-Ing. Dr. U. STAHL
Berichter:	Prof. Dr. rer. nat. W. REIMERS
Berichter:	Priv. Doz. Dr.-Ing. A. PYZALLA

Tag der wissenschaftlichen Aussprache: 17. Mai 2002

Berlin 2002
D83

Cover picture:

Scheme of the experimental setup with the torsion deformation device, the conical slit system, and a 2D-detector, allowing the dynamic in-situ observation of the strain and texture evolution within the sample.

ABSTRACT

René Valéry MARTINS

Experimental Investigation of Plastically Deformed Al-Alloy Samples Using High Energy Synchrotron Radiation

Die vorliegende Arbeit befasst sich mit der Untersuchung des Dehnungszustandes und der Textur von ein-, zwei-, und dreiachsig plastisch verformten metallischen Proben. Die untersuchten Proben bestehen aus der nicht aushärtbaren einphasigen Al-Legierung AlMg3 und in einigen Fällen aus der zweiphasigen PM-Legierung AlSi25Cu4Mg3. Die Realisierung der verschiedenen Veformungszustände erfolgte durch Zug- und Stauchverformung (einachsig), Torsionsverformung von zylindrischen Hohlproben (zweiachsig) und die Torsionsverformung von zylindrischen Vollproben (dreiachsig).

Für die zerstörungsfreien Untersuchungen des Eigendehnungszustandes der ein- und zweiachsig verformten Proben konnten etablierte zerstörungsfreie Röntgenbeugungs-verfahren, die auf der Anwendung hochenergetischer Synchrotronstrahlung basieren, angewendet werden. Für die zerstörungsfreien Messungen an den zylindrischen Vollproben, die eine starke Verformungsinhomogenität über den Querschnitt aufweisen, wurde ein neuartiges Messverfahren entwickelt, das erstmalig die dynamische in-situ Beobachtung der Textur und des Dehnungszustandes mit hoher räumlicher Auflösung im Probeninnern gestattet. Dieses Verfahren basiert auf der erstmaligen Kombination eines mikrofokussierten hochenergetischen Synchrotronstrahls, wie er an der Beamline ID11 der ESRF zur Verfügung steht, einer neuentwickelten konischen Schlitzzelle, sowie eines grossflächigen Röntgendetektors. Für die Datenanalyse wurden neuartige Verfahren angewendet, die die Entwicklung eines kompletten Programmpakets erforderten. Zusätzlich zu den Analysen mit Beugungsverfahren wurden licht- und transmissionselektronenmikroskopische Unter-suchungen der Probenmikrostruktur vorgenommen.

Die Ergebnisse der Kristallitmikrodehnungsmessungen zeigen für den unter diesem Aspekt erstmals betrachteten dreiachsigen Verformungszustand teilweise wesentlich höhere Werte, als im Falle einachsiger Verformung, was bedeutet, daß die Kristallitmikrodehnungen bei der Betrachtung dieses Dehnungszustandes nicht vernachlässigt werden dürfen. Weiterhin zeigen die Untersuchungen der Torsionsvollproben, dass die beobachteten Dehnungen für die <220> Kristallrichtung häufig ein zu den Dehnungen der anderen untersuchten Kristallrichtungen entgegengesetztes Vorzeichen aufweisen. Dies ist insbesondere für die axiale Dehnungskomponente der Fall. Die Beobachtung des sog. Swift Effekts, d.h. der Längenänderung tordierter Proben, konnte in Korrelation mit den Ergebnissen der hkl spezifischen Kristallitdehnungen und der radial abhängigen Textur gebracht werden. Die erstmals radial- und verformungsabhängig beobachtete Torsionstextur zeigt deutlich die Evolution der verschiedenen idealen Orientierungen, sowie die Rotation einzelner idealer Orientierungen. Die mikrostrukturellen Untersuchungen ergaben das Vorhandensein von drei typischen Verformungsmikrostrukturtypen in den Torsionvollproben.

ABSTRACT

René Valéry MARTINS

Experimental Investigation of Plastically Deformed Al-Alloy Samples
Using High Energy Synchrotron Radiation

In the present work experimental investigations of the texture and strain state were carried out on plastically deformed samples, made from non-age hardenable, single phase Al-alloy AlMg3 and from the two phase PM-alloy AlSi25Cu4Mg1. The samples were deformed uniaxially (in tension and compression), biaxially (torsion of tubular samples), and triaxially (free end solid torsion).

Well-established, non-destructive, diffraction techniques, based on the use of high energy synchrotron radiation, were applied for the observation of the residual strain state in the uni- and biaxially deformed samples. For the investigations of the solid torsion samples, which show a strong deformation gradient in the bulk, a novel, non-destructive, strain and texture scanning technique was successfully developed and applied. It allowed unprecedented dynamic in-situ observation with high spatial resolution of the texture and strain state within the sample. The technique combines, for the first time, a microfocussed high energy synchrotron beam (as available at the beamline ID11 at the ESRF), a newly developed conical slit system, and a large area detector for fast data acquisition. Novel data analysis techniques were applied and a complete data analysis software package was developed. In addition to the techniques based on x-ray diffraction, investigations of the deformation microstructure were carried out by applying microscopical techniques (optical microscopy, TEM).

The results for the crystallite microstrain analyses show in some cases much larger values for the triaxial deformation (not previously studied) than in the case of uniaxial deformed samples, proving that, in general, the crystallite microstrains cannot be neglected for deformations of higher dimensionality. The investigation of intergranular strains in the solid torsion samples showed that the 220 direction exhibits often the opposite sign to the strains observed for the other reflections. This is particularly the case for the axial strain component. The observation of the so-called Swift effect (i.e. the length change of plastically deformed torsion samples) was correlated with the results of the hkl specific crystallite microstrains and the local, radially dependent texture evolution. For the first time, the radially and deformation dependent texture evolution within the sample was investigated and showed clearly the development and partial rotation of ideal torsion texture orientations. From the investigations of the microstructure, three typical types of deformation microstructure could be identified.

ACKNOWLEDGEMENTS

The work presented here was realized during my three years employment as a Ph. D. thesis student at the European Synchrotron Radiation Facility (ESRF) in Grenoble, France.

I wish to thank Prof. Dr. rer. nat. W. Reimers for refereeing the thesis, his encouragement, and his interest in this work.

Many thanks go to Priv. Doz. Dr.-Ing. A. Pyzalla, not only for refereeing but also for numerous fruitful discussions and suggestions.

I would like to thank Prof. Dipl.-Ing. Dr. U. Stahl for assuming the chairmanship of the thesis committee and for the particular interest he showed for this work.

Thanks are also due to Prof. Dr. rer. nat. H. Schubert for his interest in this thesis.

I greatly acknowledge the ESRF for employing me as a Ph. D. thesis student and for the financial support. At this place I particularly would like to thank Åke Kvick for his support during all my time at the ESRF.

I acknowledge the use of the ESRF facilities and the allocation of beamtime for my research and the help from all the ESRF staff. In particular I would like to thank, representing BM16 and ID15 staff, Andy Fitch, Michela Brunelli, and Jonathan Wright, Klaus-Dieter Liss, and Veijo Honkimäki, Heinz Graafsma, and Anna Puig Molina, for squeezing me into their inhouse beamtime schedule and for their technical assistance. In this context I also wish to express my thanks towards Thomas Buslaps who more than once agreed to my “plundering” of the “ID15 Mechanics Pool”.

My special thanks go to all the people from my “home” beamline ID11. In particular to Michel Rossat, Jean-Michel Reynal, and Roland Taffut for all technical matters and to Andy Goetz for his unfailing computing assistance. I wish to thank particularly Ann Terry for the correction of the manuscript. Critical questions and discussions with Stephan Grigull were a great help in making some aspects of the work clearer. Larry Margulies can be held responsible for a cheerful office, his help during experiments, and many helpful discussions. Thanks also to Gavin Vaughan, Guido Heunen, and Caroline Curfs for the nice time on ID11.

I greatly acknowledge Carlos Tomé for providing the VPSC5 code and Stuart Ansell for actually getting it to run on a Linux machine.

An extra paragraph has to be reserved for Ulrich Lienert. He was my direct supervisor during my first two years at the ESRF. Many thanks are due to him for his enthusiasm and encouragement, his numerous suggestions and his patience in explaining and re-explaining how to use a synchrotron in the right way.

I wish to thank all the members of the collaborating group, formerly at the Hahn-Meitner-Institut, Berlin, now at the Technical University Berlin, for fruitful discussions and suggestions. In particular I wish to thank Boris Lehrer for the preparation of the TEM specimens and Christian Bohne for performing the conventional x-ray measurements.

M. Pyzalla has to be gratefully acknowledged for the manufacturing of tubular torsion samples.

The last but not the least thanks go to my family and friends for their never failing support and encouragement over all these years.

Risø, May 2002 René Valéry Martins

Im Ganzen haben wir also jetzt 623,13±1,04. – Wenn ich mir überlege, wieviel Fehlerquellen in unserem Verfahren verborgen liegen – ach, ihr Götter!

Arno Schmidt, *ENTHYMESIS oder W. I. E. H.*

TABLE OF CONTENTS

0 ABBREVIATIONS AND SYMBOLS

$\langle X \rangle^a$	angle brackets indicate averaging of X over a
α	phase index
A_5	ultimate strain with respect to gauge length $L_0=5D_0$
APS	Advanced Photon Source, USA
a	lattice parameter
at.%	atomic %
B	zone axis
bcc	base centered cubic
BW	band width
C	crystal system
CCD	charge coupled device
ccw	counter clockwise
cw	clockwise
d	lattice spacing
d_0	stress-free lattice parameter
DIC	differential interference contrast
DIN	Deutsches Institut für Normung
ε	strain in one direction
$\boldsymbol{\varepsilon}$	strain tensor
ε_{ij}	strain tensor component
ε^e	strain due to elastic interaction
ε^p	strain due to plastic interaction
ε^{pl}	plastic strain
ε_{vM}	von Mises strain
EBSD	Electron Backscattered Diffraction
EN	European Norm
EPSC	elasto plastic self consistent
ESRF	European Synchrotron Radiation Facility in Grenoble, France
f(g)	orientation distribution function
fcc	face centered cubic

Φ	Euler angle
φ	natural strain
φ	angle in sample system
$\varphi 1$	Euler angle
$\varphi 2$	Euler angle
FWHM	full width at half maximum
h	horizontal
hcp	hexagonal closed packed
HMI	Hahn-Meitner-Institut Berlin, Germany
ISO	International Standards Organization
J	multiplicity factor
L	laboratory system
l	longitudinal
L_0, l_0	deformation section / gauge length of undeformed sample
λ	wavelength
λ	rotation angle around scattering vector
m.r.d.	multiples of random distribution
NIST	National Institute of Standards and Technology
$\mathbf{n}$	surface normal vector
ODF	orientation distribution function
Ω	volume of grain, crystallite group or phase
ω	angle in laboratory system
ψ	angle in sample system, angle in $\sin^2\psi$ plots
PM	Powder Metallurgical
PSF	point spread function
PTFE	Polytetrafluoroethylene
q	scattering vector (bisector of incident and diffracted beam)
r	compliance tensor
$R_{p0.2}$	0.2% yield strength
R_m	tensile strength
RC	relaxed constraint
$\boldsymbol{\sigma}$	stress tensor
σ_{ij}	stress tensor component

σ^{H}	hydrostatic stress
σ^{D}	deviatoric stress
σ^{I}	residual stress of kind I
σ^{II}	residual stress of kind II
σ^{III}	residual stress of kind III
$\sigma^{II,e}$	elastic interaction stress
$\sigma^{II,p}$	plastic interaction stress
σ^{L}	load stress
S	sample system
S1, S2, S3	axes of sample system
SC	self consistent
SEM	Scanning Electron Microscopy
τ^{crss}	critical resolved shear stress
τ_0	critical shear stress for VPSC5 model
Θ	BRAGG angle
Θ_0	hardening rate for VPSC5 model
ϑ	twist angle
TEM	transmission electron microscope/microscopy
V	volume
v	vertical
VPSC	visco plastic self consistent model
WIMV	Williams-Imhof-Matthies-Vinel (algorithm for calculation of ODF)
wt.%	weight %
XEC	x-ray elastic constant
Z	atomic number
z	anisotropy factor

Einstein's suffix notation is used for tensor operations.

1 INTRODUCTION

The understanding of the behaviour of metallic polycrystalline aggregates under plastic deformation is of major importance for the prediction of material and product properties, such as texture, residual stress state, and tensile strength. The lifetime of engineering parts, for example, can be increased when the residual stress state is influenced in such a way that its superposition with the load stress compensates for peak stresses. By modelling thermo-mechanical processes, such as hot extrusion, it is possible to optimize the processing parameters and to predict the mechanical properties of the end product.

However, these modelling attempts are often hampered in their general application by the lack of appropriate experimental data for the verification and optimization of the models. Especially for the case of triaxial deformations, which represent the most general but also the most complex deformation state, almost no experimental data is available. Nevertheless, the knowledge of the triaxial strain state and the texture are of major importance for the explanation and interpretation of phenomena such as stress corrosion cracking, peak stresses, and fatigue. Dynamic in-situ observations on complex (i.e. triaxial) plastic deformations are missing until now. However, they would contribute to a better understanding of deformation mechanisms and the relation between microscopic and macroscopic material behaviour.

In the past, most experimental data has been obtained primarily by diffraction techniques using laboratory x-rays or neutrons. The application of these techniques for in-situ observations is limited by a long data acquisition time, the poor spatial resolution (neutrons) or the fact that the access to sub-surface regions or the bulk requires the sample destruction (laboratory x-rays). The construction of 3rd generation synchrotron sources, like the ESRF or the APS, opened new perspectives and opportunities for investigations of texture and strain, complementary to the conventional experimental approaches.

The main effort in the present work is concentrated on the development of a novel strain and texture scanning technique. It takes advantage of the high photon flux and penetration depth of a monochromatic focussed high energy synchrotron beam by combining it, for the first time, with a newly developed conical slit system and fast data acquisition using large area x-ray detectors, making the data collection two

orders of magnitude faster than the use of conventional point detectors. This angular dispersive technique allows the simultaneous (dynamic) in-situ investigation of the complete local strain tensor and the local texture within samples with steep deformation gradients in the bulk. For the data evaluation, new analysis methods are applied requiring the development of a complete software package.

Experiments are performed on uniaxially (tension, compression), biaxially (tubular torsion samples) and triaxially (solid torsion samples) deformed standard samples made from AlMg3 and AlSi25Cu4Mg1. For the investigation of the uniaxially and biaxially deformed samples, well established diffraction techniques, using high energy synchrotron radiation (energy dispersive, angular dispersive + point detector), are applied. The investigation of solid torsion samples entails particular problems which are related to the steep deformation gradient within the sample. This requires, therefore, the application of the new high spatial resolution strain and texture scanning technique. The data presented relate mainly to the non-destructive (partially dynamic in-situ) determination of the texture and the stress / strain state in the bulk of the samples. In some cases, the experimental observations are compared to model predictions. In addition to these diffraction experiments, investigations of the deformation microstructure were made by applying microscopical techniques (optical microscopy, TEM).

2 LITERATURE REVIEW AND THEORETICAL BACKGROUND

2.1 x-rays and x-ray diffraction

Electromagnetic radiation of a wavelength λ shorter than that of ultra violet light is called x-radiation. X-rays are generated by the acceleration or deacceleration of electrons. Standard laboratory x-ray tubes provide x-rays with a wavelength in the range of λ = 0.2 to 2.7Å. X-rays interact strongly with metallic materials and the penetration depth for the radiation from these sources is usually limited to a few μm in metals.

3rd generation synchrotrons [Marga 1986] like the ESRF are state of the art instruments. They provide highly collimated x-rays of very high brilliance (about 10^{20}photons / s / mm^2 / mrad^2 / 0.1%BW) and a wide wavelength spectrum going up to several hundred keV. The x-rays in a synchrotron are generated by forcing the electrons to travel in the storage ring at almost relativistic speed on a curved trajectory, thus emitting photons. This is usually done by bending magnets (BM) or insertion devices (ID) [Neu 1993]. For an in-vacuum undulator insertion device typical values for the beam divergence are: horizontal divergence ≈ 88μrad, vertical divergence ≈ 5μrad.The conversion between wavelength λ and energy E is given by:

$$\lambda = \frac{h \cdot c}{e \cdot E} \tag{2.1}$$

λ: Wavelength; h: Planck constant; c: Speed of light; e: Electron charge magnitude; E: Energy

X-ray diffraction is based on the elastic coherent scattering of the radiation when interacting with the electron shell of the atoms constituting a crystalline structure. The relationship between monochromatic radiation and the lattice spacing of a given set of planes, denoted by the Miller indices hkl, is given by the Bragg equation [Brag 1913]:

$$d^{hkl} = \frac{n \cdot \lambda}{2 \cdot \sin\theta^{hkl}} \tag{2.2}$$

d^{hkl}: Lattice spacing; Θ^{hkl}: hkl specific Bragg angle; n: Order of reflection

Recording the intensity of the diffracted beam at different Θ positions permits conclusions to be drawn e.g. on the microstructure, strains, and orientation of the irradiated crystal(s).

When white x-radiation is used the energy spectrum can be monitored with an appropriate detector, placed at a fixed Bragg angle. The relation of the hkl specific energy to the lattice spacings is then given by equation 2.3, derived from equations 2.1 and 2.2.

$$d^{hkl} = \frac{hc}{2 \cdot \sin\theta \cdot e \cdot E^{hkl}} \tag{2.3}$$

2.2 Plastic deformation of metals

2.2.1 General aspects

The main mechanism for plastic deformation of crystallites is the slip of crystal planes that occurs when the critical resolved shear stress τ^{crss} [e.g. Sch 1935] in at least one slip system is exceeded. A slip system is defined by a slip plane {hkl} and a slip direction <uvw>. Each slip system has its characteristic τ^{crss}. The stress caused in an individual slip system by an external load can be calculated via the generalized Schmid's law [Ack 1996]. The slip usually occurs on the closest packed plane along the closest packed direction which is the {111}<110> system for the case of the fcc crystal structure. In materials with a high stacking fault energy like Al and Al-alloys, other deformation mechanisms like twinning or the generation of stacking faults play an insignificant role in plastic deformation at room temperature. Higher deformation temperatures facilitate cross-slip and activate other slip systems [Hug 2000]. The main parameters of the plastic deformation of crystallites are the yield locus, the elastic modulus, and the work hardening. All these parameters are usually anisotropic with respect to the crystallite. During plastic deformation, dislocations are generated that accumulate either at the grain boundaries or form characteristic dislocation patterns within the crystallite. Strongly plastically deformed grains break up into subgrains [Bay 1992]. Plastic deformation results in grain rotations (i.e. change of texture) and deformation inhomogeneities, which cause internal stresses (see following sections). Microstructural aspects for AlMg3, the most common system presented here, will be treated in chapter 2.5.1.

2.2.2 Plasticity models

The first plasticity models, which are still important nowadays, were proposed by Sachs [Sac 1928] and Taylor [Tay 1938] for single phase metals. Sachs assumes a homogeneous stress for all crystallites while Taylor assumes homogeneous strain. The Sachs model is based on the selection of one single slip system and is considered as a "lower bound" model. The Taylor model requires at least five independent slip systems in order to assure the compatibility of the grains and is considered as an "upper bound" model [e.g. Hou 1993]. The main drawbacks of the models are the strain incompatibilities between grains in the Sachs model and the stress incompatibilities in the Taylor model, predicted textures are too sharp and too many slip systems are activated in case of the Taylor model. Based on these models various improved theories have been suggested such as the relaxed constraint (RC) [e.g. Hon 1979] and the self-consistent (SC) models [e.g. Leb 1993]. A Taylor-Bishop-Hill-type plasticity model [Bis 1951a,b] combined with a Voigt-type elastic model [Voi 1928] for the simulation of texture induced crystallite microstrains (see chapter 5) was employed by Aris [Ari 2000a], based on a work by van Acker [Ack 1996]. Other models that have been successfully used for the simulation of crystallite microstrains are the elasto-plastic self-consistent (EPSC) and the visco-palstic self-consistent (VPSC) models by Lebensohn and Tomé [Leb 1993, Tom 1991].

2.2.3 Formulæ for describing macroscopic specimen deformation

In the following, the different ways of calculating the macroscopic deformation of test specimens subjected to compressive, tensile, and torsional deformation will be addressed.

The so-called engineering strain, ε_e, is calculated in the case of uniaxial deformation according to:

$$\varepsilon_e = \frac{l - l_0}{l_0} \tag{2.4}$$

l: Length after deformation; l_0: Initial length

In case of small strains a summing of the strain of several deformation steps is possible when using the formulation of the true strain or natural strain φ, which is for uniaxial deformation, defined as:

$$\varphi = \ln(1+\varepsilon_e) = \ln\left(\frac{l}{l_0}\right) \tag{2.5}$$

The torsional deformation, γ, of cylindrical specimens is given by:

$$\gamma = \frac{r}{l_0} \cdot \hat{\vartheta} \tag{2.6}$$

r: Radius of deformation section; $\hat{\vartheta}$: Twist angle in radians

The resulting strain value is sometimes expressed in %.

In order to allow a comparison of the magnitude of strain to uniaxial deformation, the equivalent or von Mises strain can be calculated with equation 2.7 [Shr 1982], thus allowing the calculation of the resulting natural or true strain (equation 2.8).

$$\varepsilon_{vM} = \gamma / \sqrt{3} \tag{2.7}$$

$$\varphi = \ln\left(1 + \frac{\gamma}{\sqrt{3}}\right) \tag{2.8}$$

2.3 Texture

Most metallic engineering materials are polycrystalline. Each of the crystallites that constitute the polycrystalline body or sample has a distinct orientation with respect to the sample coordinate system. The sample coordinate system can be chosen in such a way that it coincides with the principal directions of a previous deformation (e.g. for rolling deformation the normal, transverse, and rolling direction or in the case of torsion the axial, shear / tangential, and radial direction). The orientation of all crystallites with respect to a given sample coordinate system is called texture. The texture is described by the orientation distribution function (ODF) of the volume fraction, V, of the crystallites with the individual orientation, g, [e.g. Bun 1997]:

$$f(g) = \frac{dV/V}{dg} \tag{2.9}$$

The orientation, g, can be expressed, for example by Euler angles, although different definitions exist within this notation. An overview of different Euler angle conventions can be found in [Wen 1998]. Here the Bunge convention for the Euler angles φ1, Φ, and φ2, shown in figure 2.1, will be used.

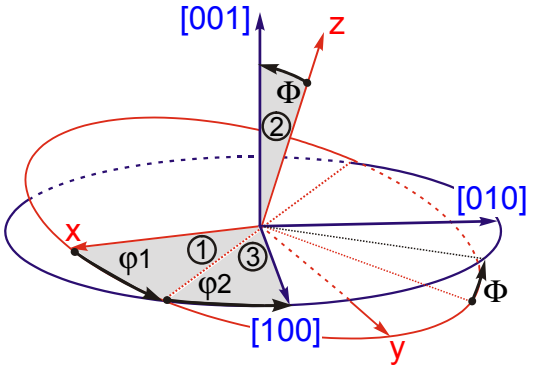

Figure 2.1: Definition of Euler angles in Bunge convention. The rotations in the order 1, 2, and 3 bring the sample coordinate system xyz into congruence with the crystal coordinate system given by the axes [100], [010], and [001].

f(g)≡1 when all crystallites are randomly oriented within the sample. This case is called random texture (some authors refer to this case as "no texture" or "untextured"). In general, the individual crystallites have direction dependent properties (e.g. elastic and plastic properties). But a polycrystal consisting of a sufficiently large amount of randomly oriented anisotropic crystallites shows isotropic properties. The texture can change due to heat treatments or deformation of the body for example. Characteristic non-random textures are the result and the sample cannot be considered anymore as isotropic. The texture can therefore have a large impact on the properties of engineering components.

Texture is commonly measured by diffraction methods, employing laboratory x-rays, synchrotron x-rays or neutrons. By recording the integrated intensity of a specific reflection {hkl} at different sample inclinations (commonly denoted by ψ or α) and azimuth angles (commonly denoted by φ or β) [e.g. Bun 1969], a two dimensional projection of the intensity distribution of that {hkl} reflection can be obtained. These so-called polefigures [e.g. Wen 1985] only contain statistical information of the orientation distribution (macrotexture) and allow no conclusions to be made about individual grain orientations and their neighbours (microtexture). The ODF represent the macrotexture and cannot be measured directly. Among the numerous determination methods, the one most commonly used nowadays is based on the representation of the ODF by a series of generalized spherical surface harmonics. Their coefficients can be calculated based on the measured polefigures [e.g.

Roe 1965, Bun 1969, Mat 1982]. A quantitative measure for the texture is the texture index, F_2, which is defined as [Bun 1982]:

$$F_2 = \frac{1}{8 \cdot \pi^2} \sum_i [f(g_i)]^2 \Delta g_i \qquad (2.10)$$

$f(g_i)$: OD value at orientation $g_i = (\varphi 1, \Phi, \varphi 2)$

Δg_i: Cell volume in orientation space (usually 5°x5°x5°)

In the case of cubic crystal symmetry, at least three (possibly incomplete) polefigures of independent reflections {hkl} are required for the calculation of the ODF. After the calculation polefigures can be recalculated for the desired reflections {hkl} to represent parts of the texture. A complete representation of the ODF is possible by sectioning the Euler space, commonly in $\varphi 1$ or $\varphi 2$ sections.

The microtexture at the surface of a material can be determined by TEM, SEM or EBSD techniques [Schw 1991]. In bulk materials it can be non-destructively measured by x-ray tracking techniques [Juu 2000].

2.4 Residual strains and stresses, theoretical groundwork

2.4.1 Equilibrium conditions

Considering a body that is free of external forces and neglecting for example acceleration terms, the variation of stress within its volume is described by the equilibrium differential equation of [Nye 1985]:

$$\sum_{j=1}^{3} \frac{\partial \sigma_{ij}}{\partial \mathbf{x}_j} = 0 \qquad (2.11)$$

where σ_{ij} are the stresses resulting from the forces acting in direction of $\mathbf{x}_j$ on the elements within the body . For the free surfaces of this body equation 2.12 holds with $\mathbf{n}_j$ being the surface normal vector.

$$\sigma_{ij} \cdot \mathbf{n}_j = 0 \qquad (2.12)$$

It follows from equations 2.11 and 2.12 that the average of any stress over the whole body is zero.

$$\frac{1}{V}\int_V \sigma_{ij}\,dV = 0 \qquad (2.13)$$

where V is the volume of the entire body. For multiphase materials equation 2.13 becomes:

$$\sum_{\alpha=1}^{n} \left\langle \sigma_{ij} \right\rangle^{\alpha} \cdot f^{\alpha} = 0 \qquad (2.14)$$

< > indicates the average over the phase α and f_α is the volume fraction of phase α.
Every stress tensor can be transformed to a tensor in a system of principal axes, i.e. a tensor where only the off-diagonal components must have zero values. The diagonal components are then called the principal stress components [Nye 1985]. Hydrostatic and deviatoric stress / strain components are defined as [Noy 1987]:

$$\sigma^{H} = (\sigma_{11} + \sigma_{22} + \sigma_{33})/3 \quad \text{and} \quad \sigma_{ii}^{D} = \sigma_{ii} - \sigma^{H} \qquad (2.15)$$

Per definitionem the deviatoric part holds equation 2.16, in other words, the trace of the tensor is zero and therefore no volume change occurs due to the deviatoric part.

$$\sum_{i=1}^{3} \sigma_{ii}^{D} = 0 \qquad (2.16)$$

2.4.2 Residual stresses

General approach

All stresses within a body, which is free of external forces, are called residual stresses (RS). External forces acting upon a body cause load stresses (LS), resulting in a superposition of LS and RS within the body.
A commonly used subdivision of RS into RS of kind I, II, and III was introduced by [Mac 1973] under the aspect of the range of effect of the specific RS. In anglo-saxon publications, RS of kind I are usually called macrostresses and RS of kind II and III microstresses.

Residual macrostress

The macrostresses, or RS of kind I, can cause a macroscopic deformation of the body when their value changes or when parts of the body are removed. Macrostresses act on all phases and grains. They are defined according to equation 2.17 with $\mathbf{x}$ signifying the position within the sample and V the considered volume.

$$\sigma^{I} = \frac{1}{V}\int_{V} \sigma\ (\boldsymbol{x})\ dV \tag{2.17}$$

The volume V has to be large enough to represent the macroscopic material consisting of crystallites of different orientations and phases. The macrostress has to equilibrate over the whole body (see equations 2.13 and 2.14).

Residual microstresses

Microstresses are all the RS acting on a smaller volume scale than the macrostress. They include the RS of kind II and III.

RS of kind II act on the scale of single grains. They are defined as the deviation of the average stress $\sigma(\mathbf{x})$ in one crystallite from the macrostress σ^{I} [Hau 1997]:

$$\sigma^{II} = \frac{1}{V_{cryst.}} \int_{V_{cryst.}} [\sigma\ (\boldsymbol{x}) - \sigma^{I}]\ dV \tag{2.18}$$

They can be caused by differences in elastic moduli or thermal expansion coefficients of the grains or phases. In the case of a multiphase material the average of the RS^{II} over one phase α are expressed by angle brackets: $<\sigma^{II}>^{\alpha}$. They compensate when averaged over all phases.

RS of kind III vary on the subgrain scale. They are defined as the local deviations of the stress within the grain from the σ^{II} (see equation 2.19) [Hau 1997].

$$\sigma^{III}(\boldsymbol{x}) = \sigma\ (\boldsymbol{x}) - \sigma^{I} - \sigma^{II} \tag{2.19}$$

RS^{III} are, for example, caused by the variation of the dislocation density within a grain.

Figure 2.2 gives an overview of the different kinds of residual stresses.

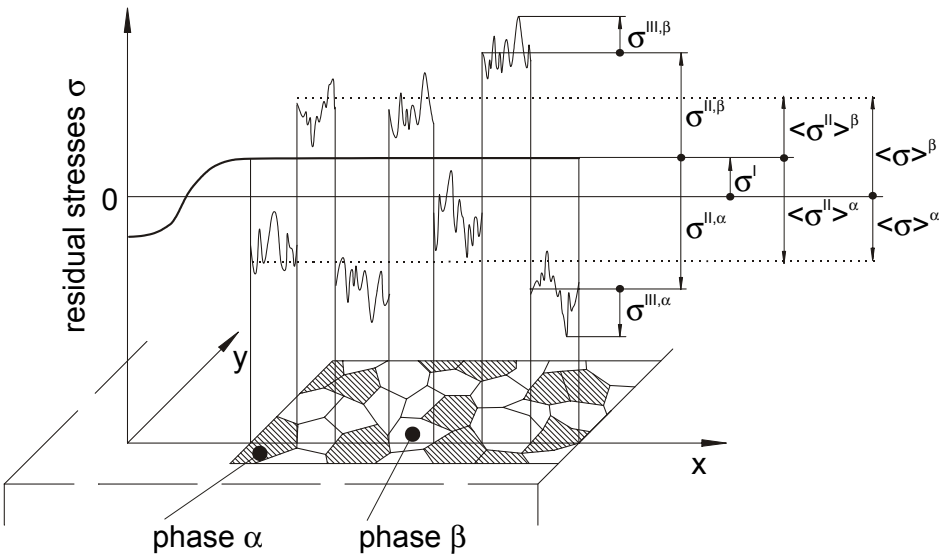

Figure 2.2: Overview of the different kinds of residual stresses. Refer to text for explanations.

Further developments

In order to accommodate this concept of classification with the experimental data and its evaluation, more precise formulations are necessary. A further subdivision of the σ^{II}, based on their origin, is useful.

Elastic interaction stresses

Elastic interaction stresses will be called the σ^{II} which are caused by differences in elastic moduli between crystallites, groups of crystallites or phases. Due to their connection to the elastic moduli they are dependent on the load stress σ^{L} as well as the macrostress σ^{I}. By definition they become zero when $\sigma^{L}+\sigma^{I} = 0$ [Ack 1996]. Since the response of grains to the stresses is dependent on their individual orientation, the elastic interaction stresses have to be defined in terms of the grain orientation g [Ack 1996].

$$\left\langle \sigma^{II,e} \right\rangle_g^{\alpha} = \frac{\int_{\Omega} \sigma^{II,e,\alpha}(g)\ f^{\alpha}(g)\ dg}{\int_{\Omega} f^{\alpha}(g)\ dg} \qquad (2.20)$$

Equation 2.20 describes the elastic interaction stresses, $\sigma^{II,e,\alpha}$ (e standing for elastic), in terms of the orientation, g, of the considered crystallites, and their orientation

distribution $f^{\alpha}(g)$, given by the orientation distribution function (ODF) [Bun 1997]. α denotes the phase for the case of a multiphase material and Ω signifies the volume of a grain, a crystallite group or a phase. It has to be noted that the $\sigma^{II,e,\alpha}$ of one crystallite group does not need to equilibrate over the whole sample, but the equilibrium has to be satisfied for the whole sample or a specified cross section when integrating over all grain orientations and phases, weighted by their respective volume fraction, given by the ODF and the composition of the material.

Plastic interaction stresses

Plastic interaction stresses will be defined as σ^{II} that have their origin in the orientation and phase dependent response to plastic deformation [Ack 1996]. They do not depend on the σ^{L} or σ^{I}. Therefore, they are, as opposed to the $\sigma^{II,e}$, also present when $\sigma^{L}+\sigma^{I} = 0$. Parameters of plastic deformation such as yield locus, elastic modulus, and work hardening are orientation dependent. This kind of stress can also have its origin, for example, in differences of the thermal expansion coefficient. Due to the fact that the latter phenomenon plays a minor role in the later discussed experiments, these stresses will be only indicated by the superscript p for plastic: $\sigma^{II,p}$.

Similar to the $\sigma^{II,e}$, the $\sigma^{II,p}$ are defined in terms of the orientation g and the ODF:

$$\left\langle \sigma^{II,p} \right\rangle_{g}^{\alpha} = \frac{\int_{\Omega} \sigma^{II,p,\alpha}(g)\ f^{\alpha}(g)\ dg}{\int_{\Omega} f^{\alpha}(g)\ dg} \qquad (2.21)$$

Acker [Ack 1996] calls them also grain microstresses while Behnken [Beh 1991] denotes the $\sigma^{II,p}$ with σ_0, since they are still present when no macro or load stresses are present. Holden *et al.* and Pang *et al.* [Hol 1997, Pan 1998a] use the term intergranular stresses.

Calculation of residual stresses

In x-ray experiments, generally, the average strain in a group of crystallites fulfilling the diffraction condition is measured. All the diffracting crystals have the normal of their diffraction planes parallel to the measurement direction given by the angles φ and ψ (see figure 2.3). The rotation around the measurement direction, λ, is free. The orientation, g, of a specific grain in the sample system is defined by the three angles φ, ψ, λ and by the hkl. The strain is determined from the shift of the reflection position relative to the reflection position of the unstrained lattice:

$$\varepsilon^{S}_{\varphi,\psi,hkl} = \frac{d_{\varphi,\psi,hkl} - d_{0,hkl}}{d_{0,hkl}} \qquad (2.22)$$

$\varepsilon^{S}_{\varphi,\psi,hkl}$ denotes the strain measured in the sample system, S, on the lattice plane, hkl, in the direction given by the angles φ and ψ (see figure 2.3). This direction corresponds to the L_{33} direction in the laboratory system, L. The transformation matrices of the tensors from one coordinate system to the other are given in [Bra 1983].

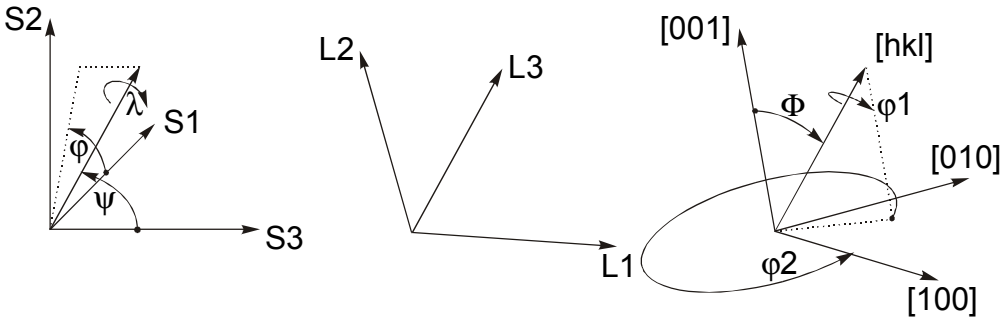

Figure 2.3: Definition of sample, laboratory, and crystal coordinate systems and the respective angles.

The aim of the calculations is the separation and estimation of the (residual) stresses σ^{L}, σ^{I}, $\sigma^{II,e}$, and $\sigma^{II,p}$ which altogether cause the strain ε, measured by means of x-rays. The peakshift observed is mainly induced by the load stress σ^{L} and the RS^{I} and RS^{II}. The RS^{III} are the main contributor to peak broadening, and therefore, will not be considered in the following. Information on the RS^{III} can be gained from different kinds of peak shape analyzing methods [see e.g. Del 1982].

The measured average strain of a given group of crystallites is caused by different kinds of stresses, as shown in equation 2.23 [similar to Beh 1991], and the observed strain is, therefore, a superposition of the response to the different stresses (equation 2.24). In other words, the approach presented here assumes the stresses due to plastic and elastic interaction are additive. Note that the term "crystallite group" refers to crystallites of almost the same orientation while, here, the expression "group of crystallites" means the crystallites whose rotation around the scattering vector is free.

$$\left\langle \varepsilon(g) \right\rangle^{\lambda} = s(g) \left\langle \sigma^{II,p} \right\rangle^{\lambda} + A(g) \left\langle \overline{\sigma} \right\rangle^{\lambda} \tag{2.23}$$

$$\left\langle \varepsilon(g) \right\rangle^{\lambda} = \left\langle \varepsilon^{p}(g) \right\rangle^{\lambda} + \left\langle \varepsilon^{e}(g) \right\rangle^{\lambda} \tag{2.24}$$

The first part of equation 2.23 covers the strains caused by plastic interaction while the second part treats the elastic response to the stresses given by [Beh 1991]

$$\overline{\sigma} = \sigma^{L} + \sigma^{I} + \left\langle \sigma^{II,e} \right\rangle^{\lambda} \tag{2.25}$$

In equation 2.23, $s(g)$ is the fourth rank tensor of the single crystal compliances. The tensor $A(g)$ describes the linear dependence of the crystallites on the average stress given in equation 2.25, their relation to the ODF, and the coupling between individual grains or grain and matrix.

For the coupling between crystallites and matrix, various models exist. The Voigt model [Voi 1928] assumes constant strain in all crystallites, the Reuss model [Reu 1929] assumes constant stress and the Eshelby / Kröner model [Esh 1957, Krö 1958] treats the crystallites as spheres embedded in a matrix which represents the average material properties, and so yields in an intermediate solution between the Voigt and Reuss model

When the Reuss model is used the strain due to elastic response can be written as

$$\varepsilon_{33}^{L,e}(g) = \left\langle r_{33ij}^{R,L,hkl}(g) \right\rangle^{\lambda} \overline{\sigma}_{ij}^{L} \quad \text{with} \quad \varepsilon_{33}^{L,e}(g) = \left\langle \varepsilon_{\varphi,\psi}^{S,e} \right\rangle^{\lambda} \tag{2.26}$$

with R indicating the Reuss model and L the laboratory system. The orientation dependent fourth rank tensors of the compliances r are given by [Hou 1993, Nye 1985]:

$$\left\langle r_{33ij}^{R,L,hkl} \right\rangle^{\lambda} = \frac{\int_0^{2\pi} s_{33ij}^{L}(\lambda)\ f[g(\lambda)]\ d\lambda}{\int_0^{2\pi} f[g(\lambda)]\ d\lambda} = \frac{\int_0^{2\pi} a_{3k} a_{3l} a_{im} a_{jn} s_{klmn}^{C}\ f[g(\lambda)]\ d\lambda}{\int_0^{2\pi} f[g(\lambda)]\ d\lambda} \qquad (2.27)$$

The a_{ij} are the direction cosines of the measurement direction in the laboratory system L with respect to the crystal system C (see figure 2.3). The integration path is determined by the angles φ, ψ, λ and the hkl.

The strain due to plastic interaction is given by [Ack 1996]:

$$\left\langle \varepsilon^{L,p} \right\rangle^{\lambda} = \frac{\int_0^{2\pi} \varepsilon^{L,p}[g(\lambda)]\ f[g(\lambda)]\ d\lambda}{\int_0^{2\pi} f[g(\lambda)]\ d\lambda} \qquad (2.28)$$

Combining equation 2.26 into equation 2.24 gives

$$\left\langle \varepsilon_{\varphi,\psi} \right\rangle^{\lambda} = \left\langle \varepsilon_{\varphi,\psi}^{p} \right\rangle^{\lambda} + \left\langle r_{33ij}^{R,L,hkl} \right\rangle^{\lambda}\ \overline{\sigma}_{ij}^{L} \qquad (2.29)$$

When a sufficient number of independent $\langle\varepsilon_{\varphi,\psi}\rangle^{\lambda}$ measurements is available, together with the ODF, a system of linear equations can be constructed which can be solved by least square fitting, where the σ_{ij} are the unknowns. In case of large $\sigma^{II,p}$, which can occur after large plastic deformations and strong texture, the fit of the linear Reuss model, weighted by the ODF, will not yield a satisfying solution. An estimation of the plastic part in the strain response is now possible from the deviation of the measured data from the fit:

$$\left\langle \varepsilon_{\varphi,\psi}^{p} \right\rangle^{\lambda} = \left\langle \varepsilon_{\varphi,\psi} \right\rangle^{\lambda} - \left\langle \varepsilon_{\varphi,\psi,\mathrm{fit}}^{e} \right\rangle^{\lambda} \qquad (2.30)$$

With

$$\left\langle \sigma^{II,p} \right\rangle^{\lambda} = \left\langle c(g)\ \varepsilon^{p}(g) \right\rangle^{\lambda} = \frac{\int_0^{2\pi} c_{33ij}[g(\lambda)]\ \varepsilon_{ij}^{p}[g(\lambda)]\ f[g(\lambda)]\ d\lambda}{\int_0^{2\pi} f[g(\lambda)]\ d\lambda} \qquad (2.31)$$

the magnitude of the plastic interaction stresses within a crystallite group can be estimated. It requires one of the various plasticity models such as the Taylor (homogeneous strain) [Tay 1938], the Sachs (homogeneous stress) [Sac 1928] or self consistent models (SC, intermediary solutions between Sachs and Taylor) [*cf.* for example Leb 1993].

From the least squares fit of the ODF weighted Reuss model the $\overline{\sigma}$ (see equation 2.29) can be estimated. As seen from equation 2.25 $\overline{\sigma}$ is a superposition of different stresses.

In the case of an applied load, the load stress σ^L can be calculated when the external applied load is measured separately. For example, in the case of large plastic torsional deformation, the shear stress τ can be estimated from the applied measured torque M_t using equation 2.32 [Can 1982]. Here, the assumption is made that the shear stress can be considered as constant over the sample cross section when the flow stress is reached at all points of the sample cross section. Slightly more accurate torque / shear stress conversions can be found in [Can 1982], but the calculations become more complex and require more than one measurement.

$$M_t = \tau \cdot 2\pi \int_{R1}^{R2} r^2 dr \qquad (2.32)$$

M_t: Torque; τ: Shear stress; r: Radius; $R1$: Inner radius (i.e. 0 for solid sample); $R2$: Outer radius

The macrostress, σ^I, can be estimated from the approximate macrostrain, ε_m, which is defined as the average of all strain distributions measured on different hkl, weighted by their respective multiplicity J (equation 2.33). Obviously this approach necessitates measurements on as many independent hkl as possible. Averages based on four different hkl or more start to give reasonable results [Ari 2000a].

$$\varepsilon_m = \frac{\sum \varepsilon_{pm}^{hkl} \cdot J^{hkl}}{\sum J^{hkl}} \qquad (2.33)$$

The ε_{pm}^{hkl} are defined as the pseudo macro strains, determined from the distortion of, at least, two complete diffraction rings of the same hkl by a least square fit of equation 2.34 [He 1998].

$$f_{11}\varepsilon_{11} + f_{12}\varepsilon_{12} + f_{22}\varepsilon_{22} + f_{13}\varepsilon_{13} + f_{23}\varepsilon_{23} + f_{33}\varepsilon_{33} = -\Delta\theta / \tan\theta \qquad (2.34)$$

ε_{ij} are the components of the strain tensor, f_{ij} are scattering vector and sample orientation dependent factors and θ is the Bragg angle of the observed hkl. The deviations of the measured hkl specific strains from the approximate macrostrain (see eq. 2.33) in the correspondent direction will be called crystallite microstrains. The deviations between the pseudo macrostrain (see eq. 2.34) and the approximate macrostrain will be called intergranular strains. σ_{ij}^{I} can be calculated from equation 2.35 [e.g. Noy 1987], using the average Young's modulus E and the Poisson ratio ν for the material.

$$\sigma_{ij}^{I} = \frac{E}{1+\nu}\ \varepsilon_{ij} + \frac{\nu\, E}{(1+\nu)(1-2\nu)}\delta_{ij}\ \varepsilon_{kk} \qquad (2.35)$$

δ_{ij} represents the Kronecker delta.

2.5 Review of experimental observations

2.5.1 Deformation microstructure in Al alloys

With respect to the deformation microstructure, Al-3wt.%Mg can be placed between two extremes, with pure Al on one side and AlMg alloys, containing more than 4.5wt.%Mg, on the other side [Hug 1993, Dul 1996]. In the following the terms defined by [Bay 1992] are employed to describe the different dislocation arrangements.

In pure Al only small dislocation mobility constraints exist, therefore a three dimensional mobility is possible, which enables the formation of low energy cell structures [Mug 1983]. These structures are described as cell blocks (CBs), subdivided into ordinary cells, almost devoid of dislocations. The CBs are separated from each other by dense dislocation walls (DDWs) and / or first generation microbands (MB1) [Hug 1993].

Due to the large atomic mismatch of about 12% between Al and Mg, solute - dislocation interactions are enhanced with increasing content of Mg. If the content is larger than 4.5 wt.%Mg, the material does not form cells [Dul 1996] and the

microstructure is characterized by Taylor lattices (TL), surrounded by domain boundaries (DBs) and microbands (MBs) [Bay 1992].

[Bay 1992] reports, that for pure Ni (which, in a similar manner to Al, has a high stacking fault energy) deformed at room temperature by rolling and torsion, the respective microstructures, due to the two deformation modes, are indistinguishable.

Investigations of the microstructure of high purity Al-3wt.%Mg alloy single crystals, rolled at room temperature, to a maximum of $\varphi = 1.2$, have been published by [Nak 1987]. At a strain of $\varphi = 0.22$, fine equiaxed cells with relatively diffuse boundaries are observed. MB clusters, parallel to the slip planes, formed at about $\varphi = 0.5$. Strong contrast differences suggested the presence of large misorientations between the MBs. At strains of $\varphi = 0.6$ to 1.2, well defined 10μm thick shear bands appeared in 100μm spacings and had crystallographic orientations. The space between such shear bands showed a microstructure consisting of MBs or elongated cells, nearly parallel to slip planes.

To the author's knowledge, there are presently no observations published on the microstructure of Al-3wt.%Mg, torsionally deformed at room temperature.

2.5.2 Uniaxial deformation, intergranular strains

Results on measurements of intergranular strains in single phase material with hcp structure are reported by [Pan 1997, Pan 1999, and Pyz 2000], and on single phase material with bcc structure, publications by [All 1989, Hau 1990, Cha 1995, Pan 1998b, and Ari 2000b] are available.

The experimental and simulation results on uniaxially deformed fcc materials will be summarized here since the observations presented in this work relate to fcc material. An overview of the residual intergranular strains observed for specific materials, textures, and plastic strains ε^{pl} is given in table 2.1. The observations by Holden *et al.* [Hol 1997],Daymond *et al.* [Day 2000], Pang *et al.* [Pan 1998a], and Clausen *et al.* [Cla 1998] show, consistently, that the 200 lattice direction, which is also the most compliant, shows the strongest intergranular strains. The 111 direction, as the stiffest crystal lattice direction, belongs to the group of planes that are affected more weakly by intergranular strains. In the case of Holden's observations on a Ni base alloy, they are even lower than the strains observed for the 311 reflection. The measurements by Daymond *et al.*, Pang *et al.*, and Clausen *et al.* reveal, in general, load strain

curves close to linearity and very low intergranular strains for the 311 direction. Though the higher multiplicity of the 311 direction might be an explanation, Clausen *et al.* conclude that a high multiplicity is no guarantee for weak intergranular strains, as can be seen from their results on the 331 and 531 plane. It is clear from all the results that the amount of plastic strain, the material, and the initial texture play a major role in the development of intergranular strains. All authors present simulations of their observations, based either on a Taylor-Bishop-Hill-type model [Hol 1997], the EPSC code by Lebensohn / Tomé [e.g. Leb 1993] [Pan 1998a, Day 2000] or Hutchinsons SC model [Hut 1970] [Cla 1998]. They all show good qualitative and quantitative agreement with the experimental data. Daymond *et al.* conclude from their simulations with the EPSC model that the largest effect on the lattice plane load response is not caused by the deformation texture but is due to residual strains and pre-straining induced hardening. A common point of all the measurements is the limitation of observation directions parallel and perpendicular to the previous load direction. Simulations for intermediate directions were published by Tomé *et al.* [Tom 1997].

Aris [Ari 2000a] presents a systematic investigation of the influence of texture, material, deformation, and deformation mode on the intergranular strains in the principal and intermediate directions. Part of this work was based on experimental results that will be discussed in chapter 5.

2.5.3 Torsional deformation

Due to its geometrical and mechanical stability, torsional deformation allows, as compared to other deformation modes, such as tension, much higher levels of plastic strain [Mont 1984, Bacz 1996]. Hot torsion tests provide, for example, information on the forgeability of the material [e.g. Gila 1994]. Tests at ambient temperature permit the investigation of the work hardening relationship at large strains [e.g. Fie 1957, Can 1982]. Torsion flow curves show generally lower flow stresses than comparable tension flow curves. Shrivastava *et al.* [Shr 1982] explain this phenomenon by differences in the work hardening behaviour due to differences in the movement of dislocation and the resulting deformation microstructure.

A distinction has to be made between the various torsion tests:

- samples: tubular or solid
- sample ends: fixed or free (i.e. permitting elongation)
- deformation direction: single or reverse
- temperature: ambient or elevated

Here only tests in single direction at ambient temperature will be considered. Results on hot and / or reversed torsion were published by, for example [Kas 1989, Hugh 1952, Wit 1980, 1982a, 1982b, Ron 1967].

The torsional deformation of tubular samples can be considered as pure shear, i.e. a biaxial stress state, when the shear stress gradient over the wall thickness can be considered to be small. The biaxial stress state has a compressive and a tensile component at ±45° to the torsion axis. The shear stress can be calculated from the applied torque using equation 2.36 [e.g. Dub 1990]. Both components have the same absolute value as the shear stress. The stress state in a solid cylindrical torsion sample can be considered as approximately biaxial too, as long as the deformation is elastic. The radial dependence of the shear stress is then given by equation 2.36, setting $R_1 = 0$.

$$\tau(r) = \frac{2 \cdot M_t \cdot r}{\pi \cdot (R_2^4 - R_1^4)} \qquad (2.36)$$

τ: Shear stress; M_t: Torque, r: Radial position;

R_1: Inner radius; R_2: Outer Radius

The axial effect and torsion texture

A well known peculiarity of torsional deformation is the development of axial forces when the ends are kept fixed, or an elongation of the sample, when a deformation with free ends is carried out. This phenomenon was observed at small strains [e.g. Poy 1912, Lal 1974] as well as large strains [e.g. Swi 1947, Hugh 1952, Por 1970, Ros 1968]. The cases reported for small strains involve certain aspects of non-linear or anisotropic elastic behaviour and will not be further discussed since all sample deformations presented here belong to the large strain range. The case of large torsional strains was first studied by Swift [Swi 1947], hence, being also known as "Swift Effect". The main observations at large strains can be summarized as follows [Mon 1984]:

- Single phase materials exhibit a general but not unique trend towards lengthening at room temperature and a trend towards shortening during hot deformation. Al is an exception. It does not lengthen or shorten at elevated temperatures.
- The initial state of the sample plays an important role for the sign of the length change when the strain is small. However, when large strains are applied, the beforehand mentioned behaviour is recovered.

Swift tried to explain the observed length change by the work hardening, elongation, and rotation (i.e. a change of texture) of certain grains. The first systematic examinations on the link between length change and texture were made by Rose *et al.* [Ros 1968]. Further experiments were carried out by [e.g. Mon 1984, Tót 1992, Bacz 1996]. These works were accompanied by theoretical approaches of [Gil 1975, Hou 1976, Can 1984, Mon 1985, Jon 1993, Nin 1994]. The conclusions on single direction torsion of fcc metals and in particular Al can be summarized as follows:

Solid Al samples deformed with fixed ends at room temperature show a strong maximum of the axial compressive force (i.e. elongation) at a deformation of $\gamma \approx 0.9$. The compressive axial force then decreases and starts to increase again at $\gamma \approx 2.9$. A set of ideal crystal orientations, given in table 2.2 and represented in figure 2.4, develops in fcc metals due to torsion [Mon 1985, Jon 1993]. [Back 1950] concluded from his experimental polefigures that the texture has the axial and tangential directions as symmetry axes. However, [Hou 1976] showed later that the polefigures of torsion textures must have a dyadic symmetry when the radial direction is perpendicular to the projection plane of the polefigure. The ideal orientations can be

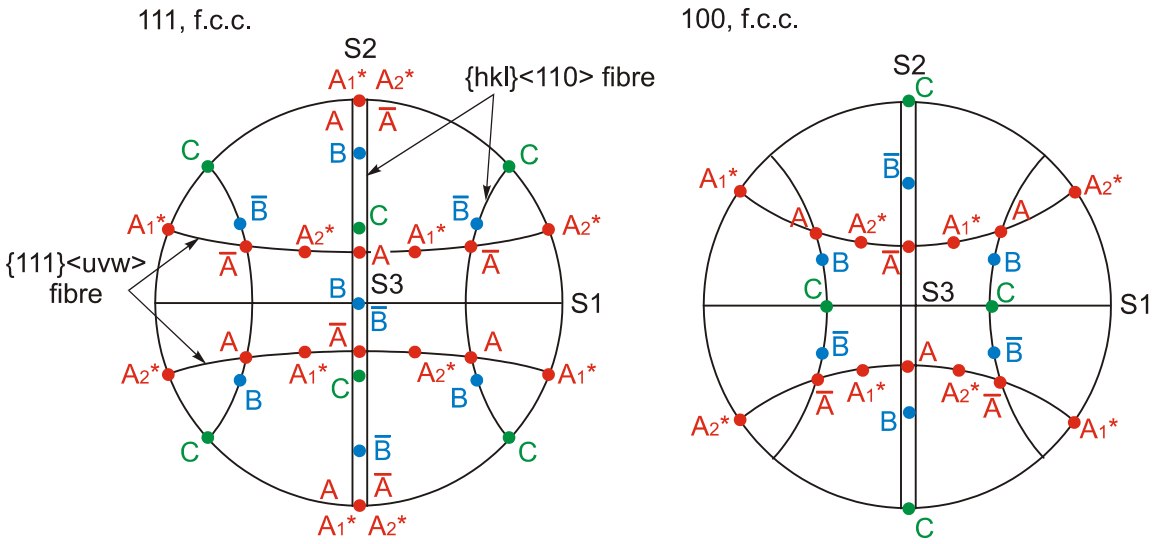

Figure 2.4: 111 and 100 polefigure representation of the ideal orientations in fixed end torsion of f.c.c materials. S1, S2, and S3 are the sample axes [adapted from Jon 1993 and Mon 1985]

subdivided in "self-symmetric" orientations (C), and "twin-symmetric" orientations (A / $\overline{A}$, B / $\overline{B}$, A_1^* / A_2^*). At small strains, at room temperature, the A component appears first. Prior to fracture, the C component is the principal one. The polefigures of samples in which a length change was observed, show a slight rotation around the symmetry axis. This rotation is opposite to the sense of shear at low strains and in the same sense at large strains [Mon 1984, Tót 1992]. Montheillet *et al.* [Mont 1985] conclude from theoretical considerations for the {hkl}<110> orientations that the axial stresses / elongation are zero when the texture shows no rotation. The B / $\overline{B}$ orientation does not lead to axial stresses / elongation, whatever its rotation is. The A / $\overline{A}$ and C components produce only small axial stresses whose sign and magnitude depend on the rotation. Only A_1^* / A_2^* cause large axial stresses, independent on the texture rotation.

All these observation relate to texture measurements made at the sample surface. The measurements of developing axial forces are an integration over the cross section. No observations are reported on the behaviour of the bulk.

Table 2.2: Notation and Miller indices used for the different ideal orientations [Mon 1985]

label	crystal orientation {hkl} <uvw>‡
A	$\{1\bar{1}1\}\langle 110\rangle$
$\overline{A}$	$\{\bar{1}1\bar{1}\}\langle\bar{1}\bar{1}0\rangle$
A_1*	$\{\bar{1}\bar{1}1\}\langle 112\rangle$
A_2*	$\{11\bar{1}\}\langle 112\rangle$
B	$\{1\bar{1}2\}\langle 110\rangle$
$\overline{B}$	$\{\bar{1}1\bar{2}\}\langle\bar{1}\bar{1}0\rangle$
C	{100} <110>
{111} fibre	{111} <uvw>
<110> fibre	{hkl} <110>

‡{hkl} is the shear plane normal (i.e. in direction of Z / S2) and <uvw> is the shear direction (i.e. in direction of Θ / S1

2.5.3.1 Investigation of residual stresses

Measurements of the residual strains after plastic torsional deformation are reported by Bollenrath *et al.* [Bol 1967] and Allen *et al.* [All 1985]. Bollenrath *et al.* investigated different steels with the bcc structure while Allen *et al.* used a tubular mild steel (bcc) sample. The former concluded from their measurements at the surface and lower layers, made accessible by etching, that no axial and tangential / hoop residual stresses have developed due to the deformation. The signs of the stresses observed at ±45° to the torsion axis are opposed to those of the previous applied load.

The results of Allen *et al.* from their bulk measurements (only the 211 reflection investigated by neutron diffraction) are themselves rather contradictory though they draw the conclusion, as opposed to Bollenrath *et al.*, that the sign of the residual stress components have the same sign as the respective load stress components.

Bollenrath *et al.* determined, from their measurements, the XEC of the materials. The values are systematically 15 to 20% lower compared to the XEC determined from tensile tests. However, [Pöh 1990] points out that the properties of the material at the

sample surface may be altered by oxidation and microcracks which occur well before failure. The influence of the texture is also likely to have an impact on these observations when considering how the elastic constants are linked to the measured strain and the calculated stress (see chapter 2.4.2).

No experimental observations have been reported on the radial dependence of the strain tensor within torsion samples, mainly because of the lack of appropriate experimental techniques permitting the spatial resolution of the deformation gradient within the sample.

Table 2.1: Overview of residual intergranular strains in fcc materials observed after plastic tensile loading

material	ε^{pl} [10^{-2}]	initial texture	∥ to prev. load	⊥ to prev. load	residual strains [10^{-4}] (uncertainty ≈ ±1x10^{-4}) 111	200	220	311	331	531	ref.
monel-400	~8.5	weak	RD		0	+7	-3	+0.5	-	-	[Hol
(Ni base		rolling		ND	0	+1	-1	+0.5	-	-	1997]
alloy)				TD	+1	+3	-1	+1	-	-	
nitronic 40	9.5	random	X		-1.5	+5.5	-3.5	+0.5	-4	-	[Day
(austenitic				X	-1.5	+2	-2	-0.5	-1.5	-	2000]
steel)	4.5	rolling	RD		-3.5	+14	-1	+0.5	-3.5	-	
				ND	+3	+9	-3.5	-0.5	-1.5	-	
	1.5	rolling	TD		-3.5	+0.5	-1	+4	-2	-	
				ND	-3.5	-4	0	-3	-1.5	-	
Al7050	1.5	weak	RD		-8	+11	-8	+5	-	-	[Pan
(Al alloy)		rolling		ND	2	-3	-3	-5	-	-	1998a]
				TD	-9	+6	-2	3	-	-	
			ND		-2	-7	-4	-4	-	-	
				RD	-5	11	-2	4	-	-	
				TD	-6	11	2	0	-	-	
Al	5	random	X		+2	-1	1	-0.5	-0.5	0	[Cla
				X	-1.5	+2.5	-0.5	0	-0.5	0	1998]
Cu	5	random	X		0	+3	-1.5	0	-1.5	-1.5	
				X	-1	+2.5	-1	0	0	0	
austenitic	5	random	X		0	+7	-3	0	-3	-3	
steel				X	-1	+5	-1.5	0	-0.5	-0.5	

3 MOTIVATION AND AIM

The availability of experimental data on texture and strain from samples made of the same material and deformed plastically in different deformation modes and dimensionalities is not very large. Amongst other reasons, this is due to the lack of appropriate experimental techniques providing high spatial resolution when the analysis of inhomgeneous deformations is intended. Until now only data integrating over the whole sample cross section or mainly relating to the sample surface was published, especially for the torsion of solid samples. It is well known that measurements on the sample surface do not reflect the plastic behaviour of the bulk. An important aspect in the deformation of metals, in terms of microstructure, texture, and strain state, is their deformation history. Therefore, it is necessary to perform non-destructive investigations of the bulk at different stages of deformation or even in-situ. This means that these investigations cannot be done using laboratory x-ray diffraction techniques.

From these facts three objectives for the present work are emerging:

The need of experimental data for the optimization of existing or the development of new plasticity models gives raise to the first objective which is to undertake systematic investigations on samples made of the same material and deformed uni-, bi-, and triaxially (i.e. increasing complexity of the deformation). The uniaxially (tension, compression) and biaxially (tubular torsion sample) deformed samples can be examined with existing techniques implying high energy synchrotron radiation. However, this is not the case for the solid samples, deformed triaxially in torsion, since they exhibit a steep deformation gradient in the bulk.

The second aim arises from the requirement of a non-destructive strain and texture scanning technique of bulk materials with high spatial resolution, combined with a fast data acquisition in order to allow dynamic in-situ observations. This technique should then be applied to the case of the plastic deformation of solid torsion samples. The technique should take advantage of the micro-focussed monochromatic high energy x-ray beam available on the beamline at the ESRF where this work was done. The high photon-flux and the high energy x-rays available there are essential for non-destructive in-situ investigations of the bulk.

The third goal is closely linked to the second one. Except for basic image processing software and a program for the ODF calculation, essentially no data analysis software is available for the new technique. This entails the necessity of developing almost the complete analysis software.

4 EXPERIMENTS

4.1 Samples

4.1.1 Materials

The samples investigated were made of two different Al alloys: AlMg3 and AlSi25Cu4Mg1. These materials have a fcc crystal structure (space groups: Al: Fm3m, Si: F43m).

AlMg3 (material number 3.3535.10) is a non-age hardenable, commercial purity, Al alloy, containing 3wt.% Mg in solid solution. It is one of the most widely used Al alloys in fields such as construction engineering or packaging. The samples were machined from hot extruded rods. The average grain size prior to deformation, determined by optical microscopy, was 60μm (see chapter 5.1).

AlSi25Cu4Mg1 is a PM-alloy that consists of approximately 25 wt.% coarse Si hard particles embedded in a soft Al alloy matrix. The Al matrix contains 4wt.% Cu and 1wt.% Mg in solid solution. The average grain size of the Al matrix is 5μm and the size of the Si particles ranges from 5 to 15μm, as determined by optical microscopy (see chapter 5.1). The material is used in car manufacturing since it combines high wear resistance with a good strength to weight ratio. AlSi25Cu4Mg1 is produced by thermal spraying and subsequent hot extrusion, [Mül 1999, Pyz 2000b]. The material was provided by Peak Werkstoff GmbH (Velbert / Neviges, Germany).

In all cases the longitudinal sample axis was parallel to the extrusion direction of the raw material.

Table 4.1 gives an overview of the material characteristics.

Table 4.1: Overview of the sample material characteristics [Dub 1990, Pea 1994]

material	R_m [MPa]	$R_{p0.2}$ [MPa]	A_5 [%]
AlMg3	190	80	20
AlSi25Cu4Mg1	230	135	2.9

4.1.2 Geometry

Figures 4.1 to 4.4 show the geometries of the tensile, compression, and the tubular torsion as well as the solid torsion samples.

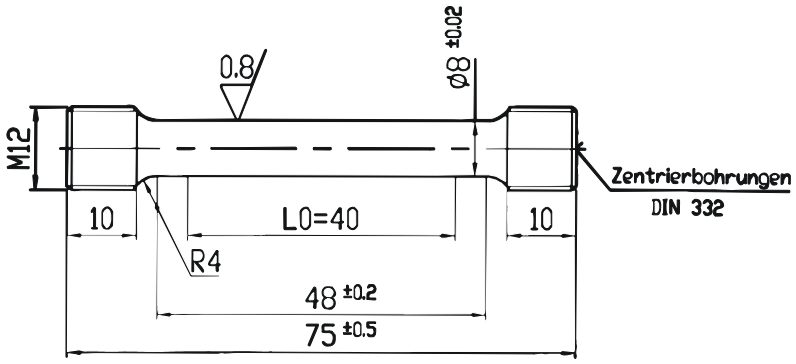

Figure 4.1: Geometry of tensile sample according to DIN 50125 B 8x40 [DIN 1991]

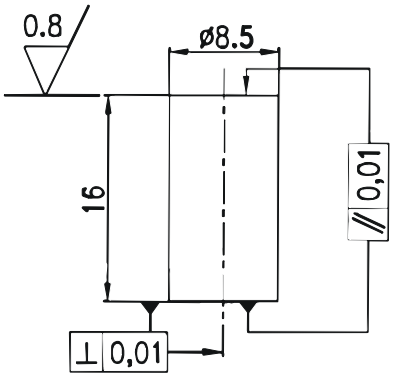

Figure 4.2: Geometry of compression sample similar to DIN 50106 [DIN 1978]

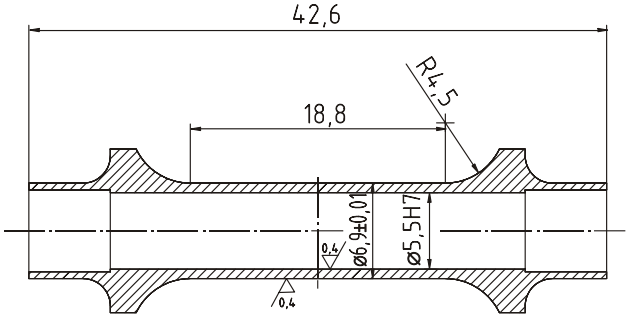

Figure 4.3: Geometry of tubular torsion sample

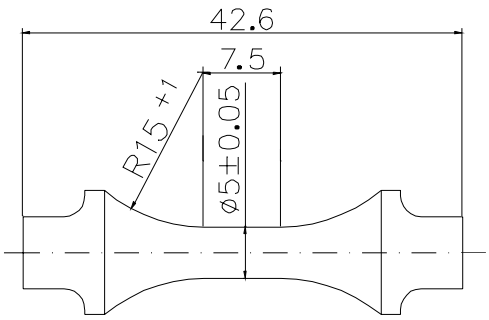

Figure 4.4: Geometry of solid torsion sample according to DIN ISO 1352 [DIN 1977]

4.1.3 Heat treatment

All the torsion samples were heat treated prior to deformation in order to reduce internal stresses due to manufacturing.

For the samples made from AlMg3 it was necessary to stay below the recrystallisation temperature to avoid grain growth. The heat treatment, therefore, consisted of heating to 220°C with a heating rate of 10°C / min, holding the temperature at 220°C for 2h and cooling down by leaving the samples inside the switched-off furnace.

The microstructure of the samples made of the AlSi alloy is very stable with respect to elevated temperatures [Weg 2001]. Therefore, the heat treatment of these samples was performed by heating to 400°C with a heating rate of 20°C / min, holding the temperature at 400°C for 2:45h and cooling down by leaving the samples inside the switched off furnace.

4.1.4 Deformation devices

The tensile and compression samples were deformed at the Bundesanstalt für Materialforschung (BAM), Berlin, Germany, on a 300kN Instron stress rig.

The torsion samples were deformed using a device developed at the HMI by the author in the framework of his diploma thesis [Mart 1998]. The small dimensions of the device permit an easy implementation into experimental setups, thus enabling in-situ investigations of the sample deformation. The device is designed for free end

torsional deformation, i.e. the samples can contract or elongate during the deformation. The deformation is controlled via the twist angle and a strain gauge permits the constant readout of the applied torque. The maximum twist speed with the actual motor configuration was 0.41° / s.

4.1.5 Deformation

All samples were deformed at room temperature.

The tensile and compressive deformations were performed ex-situ in strain control, with a strain rate of $d\varepsilon / dt = 1.25x10^{-4}s^{-1}$ (see chapter 2.2.3 for definitions of deformation). Four samples were deformed in tension and compression respectively. For the tensile deformation, one sample was deformed until failure. The deformation of the remaining samples was then adapted to equally fill the range between zero and maximum deformation. In case of the compression, the maximum deformation was determined as being when the sample began to bulge.

All torsional deformations were carried out in single direction. The tubular torsion samples were deformed ex-situ, in strain control, with a strain rate of $d\gamma / dt = 1.36x10^{-3}s^{-1}$, which corresponds to the maximum possible rate provided by the deformation device. To improve the geometric and mechanical stability of the deformation, an insert made of PTFE was inserted in the tubular samples.

The solid torsion samples were deformed (in-situ) in strain control. The strain rate for these samples ranged from $d\gamma / dt = 1.5x10^{-3}s^{-1}$ to the maximum possible rate $2.38x10^{-3}s^{-1}$(Note, when comparing the maximum strain rates of the solid and the tubular samples that these also depend on the sample dimensions). In most cases the deformation took place at the highest rate since it is known [Mon 1984] that residual stresses due to deformation increase with increasing strain rate. The deformation procedure for most solid torsion samples was as follows: After a first deformation the sample was unloaded and the strain state was investigated non-destructively. Then the sample was further deformed, unloaded and investigated and so on. In some cases the strain state was investigated under load. The sample on which dynamic in-situ investigations were carried out, was deformed continuously at the lowest strain rate.

Table 4.2 gives an overview of the sample deformations. Due to the geometric and mechanical stability [Mon 1984], the achievable deformations are the highest for the solid torsion samples.

Table 4.2: Overview of the deformation parameters of the presented samples

sample #	sample type	material	γ	φ	$d\gamma/dt$ [s^{-1}]	$d\varphi/dt$ [s^{-1}]
ZA4	tension	AlMg3	-	0.24	-	4.99×10^{-3}
DA5	compression	AlMg3	-	0.455	-	4.99×10^{-3}
TA31	tubular torsion	AlMg3	0.15	0.083	1.36×10^{-3}	7.85×10^{-4}
TA29	tubular torsion	AlMg3	0.30	0.159	1.36×10^{-3}	7.85×10^{-4}
TA30	tubular torsion	AlMg3	0.40	0.208	1.36×10^{-3}	7.85×10^{-4}
TA26	tubular torsion	AlSi25Cu4Mg1	0.15	0.083	1.36×10^{-3}	7.85×10^{-4}
TA8	solid torsion	AlMg3	1.50	0.624	2.38×10^{-3}	1.37×10^{-3}
TA8	solid torsion	AlMg3	2.50	0.893	2.38×10^{-3}	1.37×10^{-3}
TA8	solid torsion	AlMg3	3.50	1.105	2.38×10^{-3}	1.37×10^{-3}
TA6	solid torsion	AlMg3	0...2.20	0...0.82	2.38×10^{-3}	1.37×10^{-3}
TA11	solid torsion	AlSi25Cu4Mg1	0.15	0.083	1.5×10^{-3}	8.66×10^{-4}
TA11	solid torsion	AlSi25Cu4Mg1	0.30	0.159	1.5×10^{-3}	8.66×10^{-4}

4.1.6 Preparation of optical microscopy and TEM specimens

The optical microscopy specimens were obtained from the solid torsion samples by cutting them perpendicularly to their longitudinal axis. They were ground on SiC paper up to grade 1200 and then polished with a diamond and oxide suspension of 1μm grains. Afterwards the specimens were etched for 50s in 1mol % NaOH solution at 50°C to make the Al grain boundaries visible [Pet 1994].

The TEM specimens were prepared from a deformed solid AlMg3 torsion sample. The white circles, in figure 4.5, indicate the positions in the sample from where the foils have been taken. The sample coordinate system (see also chapter 4.2.2.2) is given by S1, S2, and S3. S1 is the shear or tangential direction, S2 indicates the shear plane normal or the axial direction of the torsion sample, and S3 represents the radial direction of the torsion sample or the normal direction of the foils. These directions were marked on the foils in order to allow later the identification of the shear direction on the TEM micrographs. The white double arrow shows the orientation of the previously applied torque, i.e. the shear was negative with respect to the sample system. After mechanical thinning to about 100μm, foils of 3mm

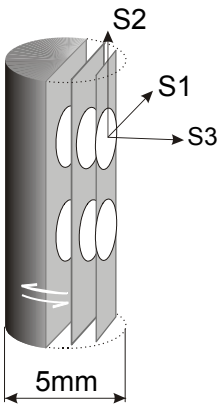

Figure 4.5: Deformed cylindrical section of solid torsion sample and sample coordinate system. The white circles show the positions from where foils were taken. The white double arrow indicates the direction of the previously applied torque.

diameter were punched. These were then electrochemically thinned in a 10 vol.% perchloric acid / ethanol solution with a tension of 20V and a current of 60mA, at a temperature of about -7°C .

Since the deformation depends linearly on the radial position within the torsion sample, the TEM specimens, taken from different radial positions, have undergone different deformations. Table 4.3 gives an overview of the radial positions and the corresponding deformations.

Table 4.3: Previous radial position of TEM specimens in torsion sample and corresponding deformation

specimen #	3A / B	2A / B	1A / B
radial pos. in mm	~0.3	~1	~2
deformation γ	0.18	0.6	1.2
von Mises strain ε_{vM}	0.1	0.35	0.7
natural strain φ	0.1	0.3	0.53

4.2 Methods

4.2.1 Experimental setups

4.2.1.1 Energy dispersive setup

The experiment involving the energy dispersive strain scanning technique [Rei 1999] was carried out on the beamline ID15A, at the ESRF [ID15A], in transmission geometry. The experimental setup is shown schematically in figure 4.6. A white synchrotron x-ray beam was used, confined by slits to a size of 0.1x0.1mm^2.

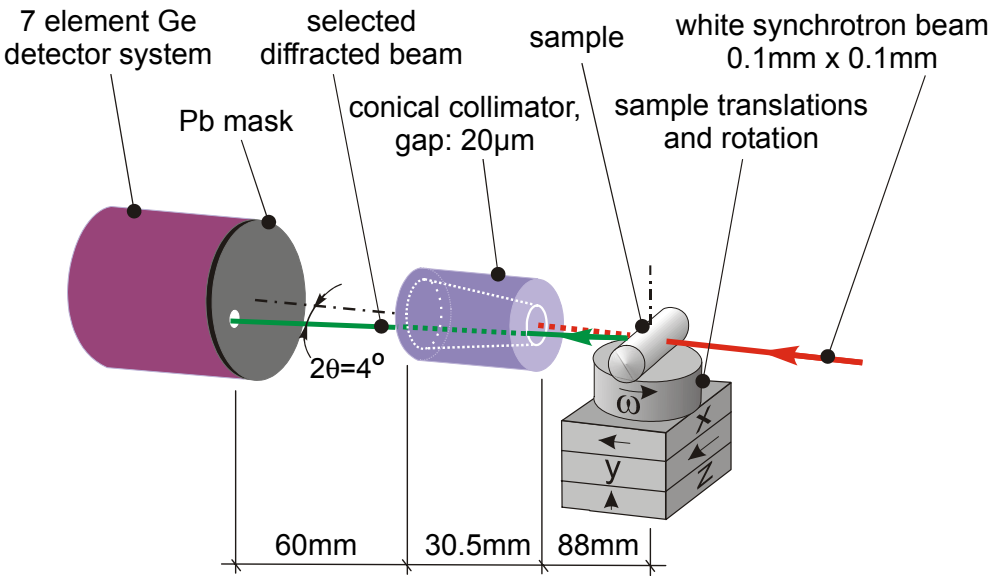

Figure 4.6: Experimental setup for energy dispersive technique

A conical collimator was placed 88mm behind the sample to define the gauge volume. The collimator had a nominal gap and a length of 20µm and 30.5mm, respectively. It allows selection of diffracted beams emanating from the gauge volume at an angle of $2\theta = 4°$. These dimensions result in a gauge volume size of about $0.1 \times 0.1 \times 2.5 mm^3$ (h x v x l). 60mm behind the conical collimator a thirteen element Ge detector system [Neu 1993] was placed. Since only one detector channel was required, a Pb mask with an entrance hole for the selected channel was placed in front of the detector. The size of the hole was 8mm, therefore selecting an azimuthal section of the diffraction cone of about 35°. The sample was mounted on an xyz translation stage for the alignment and on a rotation table in order to move the sample to different ψ-angles in the diffraction plane.
Table 4.4 gives an overview of relevant experimental parameters.

4.2.1.2 Angle dispersive setups

Using a standard laboratory x-ray source

On selected samples, strain measurements were performed in reflection geometry on torsion sample surfaces at the HMI, on a standard diffractometer in ψ-configuration [e.g. Hau 1997]. CoKα radiation ($\lambda = 1.78892$Å) was used, confined by a 1mm collimator. A point detector, in combination with an analyzer crystal, was used to

scan the diffraction peaks. The counting time per detector position was 10s on average, depending on the investigated reflection.

Table 4.4: Overview of parameters for the major experiments. The exposure time relates to each gauge volume position and can vary, depending on the measured reflection. All experiments listed were performed in transmission geometry. The ring current and filling mode relate to the synchrotron storage ring. (Refer to text for further explanations)

beamline at the ESRF	ID15A	BM16	ID11	ID11
technique	energy dispersive	angle dispersive	angle dispersive	angle disp. + conical slit cell
ring current [mA]	200	80	200	200
ring filling mode	2 / 3	16 bunch	2 / 3	2 / 3
beam energy [keV]	white	30	80	55
wavelength λ [Å]	white	0.40576	0.1549	0.2254
average gauge vol. size [μm], (h x v x l)	100x100x2500	1000x300x wall thickness 700	10x8x450	8x5x500
oscillation range [mm]	0	10	5	5
azimuthal acceptance / binning [º]	35	3	5	5
exposure time [s]	60	300 - 540	5	10 [1] *
detector type	point	point	area (4x4cm^2)	area (35x35cm^2) [area (18x18cm^2)]*
detector resolution	400eV	0.3mrad	150μm	310μm

*values in square brackets relate to the dynamic in-situ measurements

Using low energy synchrotron radiation

These experiments were performed on the beamline BM16 at the ESRF [BM16]. The two circle diffractometer on this beamline was designed for high resolution powder diffraction experiments but it could be easily modified for strain measurements on the tubular torsion samples. Due to the total thickness of the sample walls of 1.4mm, the x-ray beam with an energy of 30keV still provided sufficient penetration depth and photon flux for measurements in transmission geometry. Figure 4.7 shows a sketch of the experimental setup. The parallel beam was confined by slits to a size of 1x0.3mm^2 (h x v). A vertical slit was placed behind the sample in order to select only

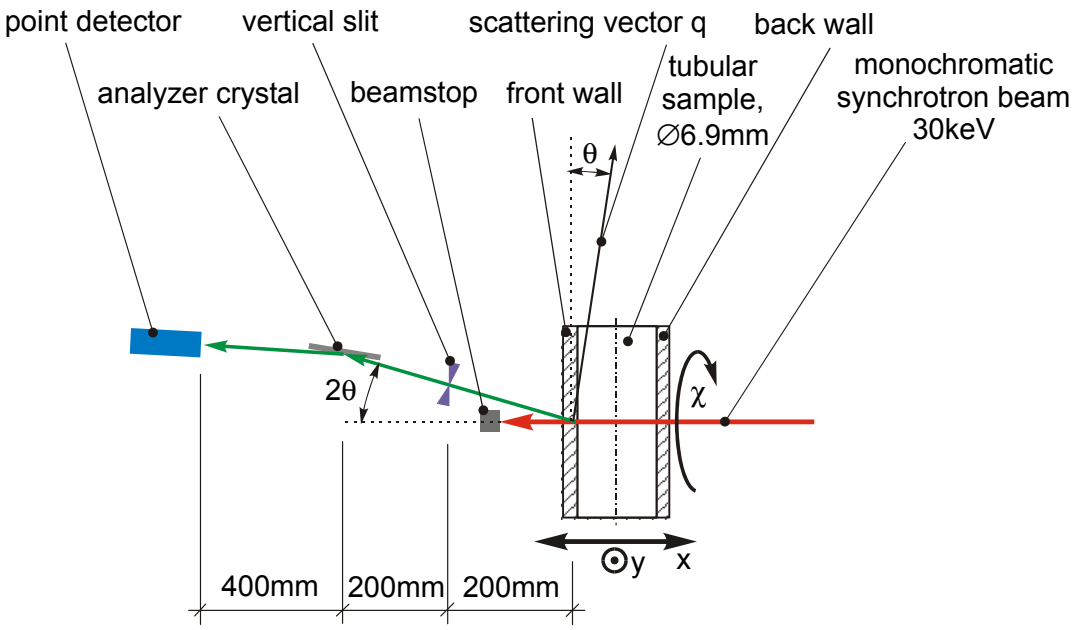

Figure 4.7: Experimental setup for angle dispersive technique, using analyzer crystal and point detector

the signal coming from the tube wall positioned in the center of the diffractometer. A point detector in combination with an analyzer crystal was used to scan the diffraction peaks in the vertical scattering plane. A sample rotation around the incoming beam permitted measurements at different sample orientation angles χ.

Using high energy synchrotron radiation

These experiments were performed on the diffractometer in the 2nd hutch of the beamline ID11 at the ESRF [ID11]. This instrument is dedicated to three dimensional x-ray diffraction (3DXRD) [Lie 2000a]. The high energy x-ray beam was focussed in two dimensions to below $10x10\mu m^2$ (see table 4.4), using a bent Laue crystal [Schul 1998] and an elliptical multilayer mirror [Lie 2001]. The gauge volume was defined by employing the crossed beam technique [cf. e.g. Lie 2000b]. The longitudinal resolution, i.e. the third dimension of the gauge volume, depends on the height and width of the focussed incoming beam, the scattering angle of the investigated diffracted beam, and the gap of the triangulation slit behind the sample. Based on this principle, two different setups for high resolution strain scanning on torsion samples were used, involving two different slit and detector systems.

Single triangulation slit

In the experimental setup, shown in figure 4.8, the scattering plane was horizontal and a 20μm wide horizontal slit was placed 100mm behind the sample which results in an average longitudinal resolution of 350μm. The distance of 100mm was required due to space constraints with the sample placed in the torsion device (not shown in figure).

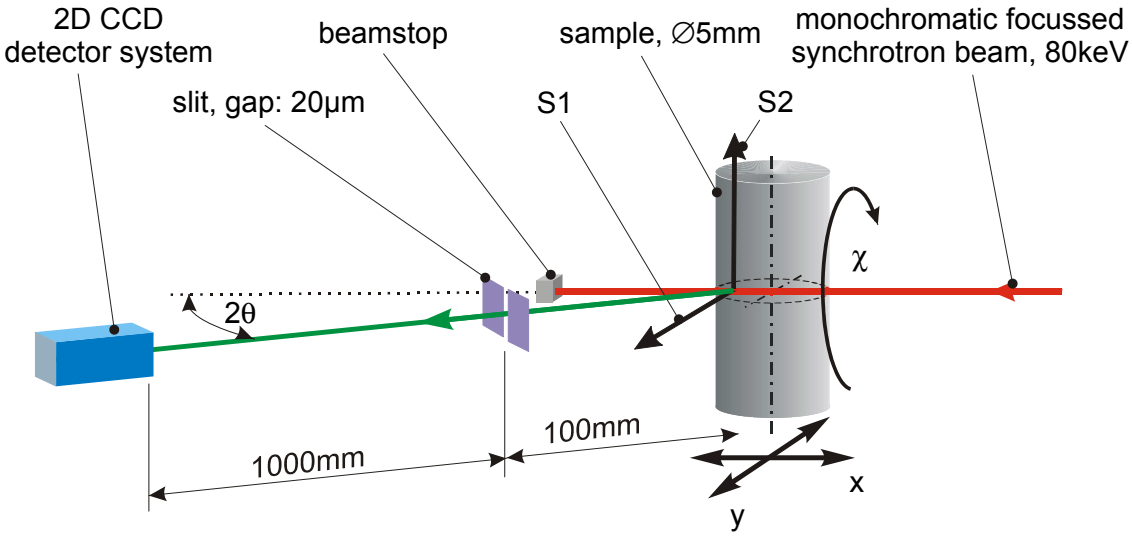

Figure 4.8: Experimental setup for angle dispersive technique, using a triangulation slit and 2D detector

The average azimuthal section of a Debye-Scherrer ring selected by the slit was about 7°. It depends on the scattering angle of the investigated reflection, the sample-to-slit distance, and the height of the triangulation slit. The x-rays emanating from the selected gauge volume were recorded on a two dimensional detector, which was situated 1100mm behind the sample. Sample translation stages enabled the measurements at different gauge volume positions within the sample. In order to detect additionally different sections of the Debye Scherrer cone the sample could be rotated around the incoming monochromatic beam.

Conical slit system

The experimental setup involving the 2nd generation conical slit system [*cf.* Nie 2000 for 1st generation] and a large area detector is represented in figure 4.9. The slit system, consisting of six 25μm wide conical apertures, was positioned 100mm behind the sample which corresponds to the common focal distance of the cones (in other words the selected diffraction cones have a common geometrical apex).

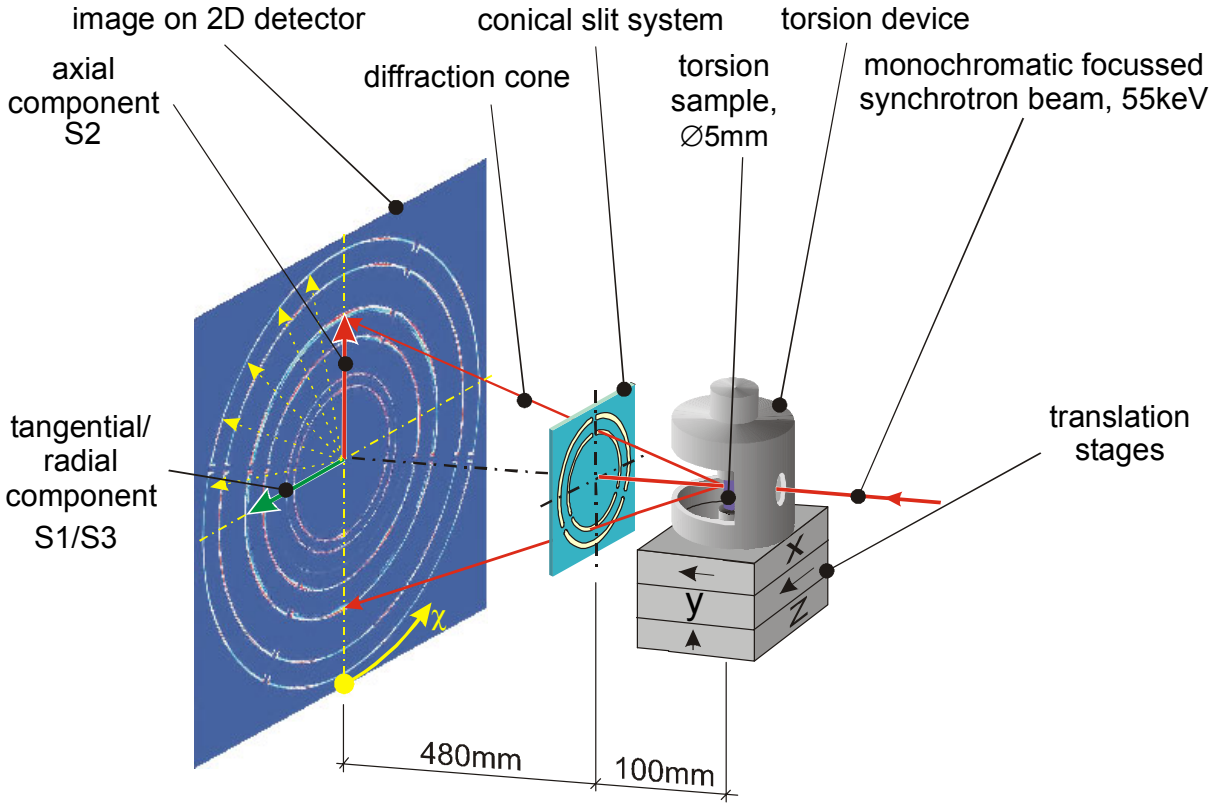

Figure 4.9: Experimental setup for angle dispersive technique, using conical slit system and 2D detector

The six complete Debye-Scherrer rings emanating from the same local gauge volume were detected simultaneously on a two dimensional detector placed 480mm behind the slit system. The conical slit system was designed for the investigation of cubic structures. In the case of fcc materials at once the 111, 200, 220, 222, 331, and 422 reflections can be monitored. The longitudinal resolution is the highest for the 422 reflection with 260μm. Accordingly, the 111 reflection has, with 750μm, the lowest resolution. Table 4.5 gives an overview of the experimentally determined longitudinal gauge lengths (see also chapter 4.2.5.3). For the dynamic in-situ experiments (i.e. continuous sample deformation), a CCD detector with fast read-out

time but smaller x-ray sensitive area was used. The detector slit distance was, in that case, 390mm and the reflections 111, 200, and 220 were monitored.

Table 4.5: Overview of the reflections selected by the 2nd generation conical slit system and the correspondent measured longitudinal gauge lengths

hkl	111	200	220	222	331	422
gauge length [μm]	750	640	500	420	370	320

4.2.2 Experimental procedures

4.2.2.1 Strain mapping

Figure 4.10 shows the scheme of the gauge volume positions for the mapping within the solid torsion samples. Since a single image contains only information about a biaxial strain state, the rings recorded at the positions shown by black dots in figure 4.10a, contain only information on the strain components in the tangential (S1) and axial (S2) direction and their radial dependence. Measurements at the positions shown in figure 4.10b are required to obtain additional information on the radial component (S3).

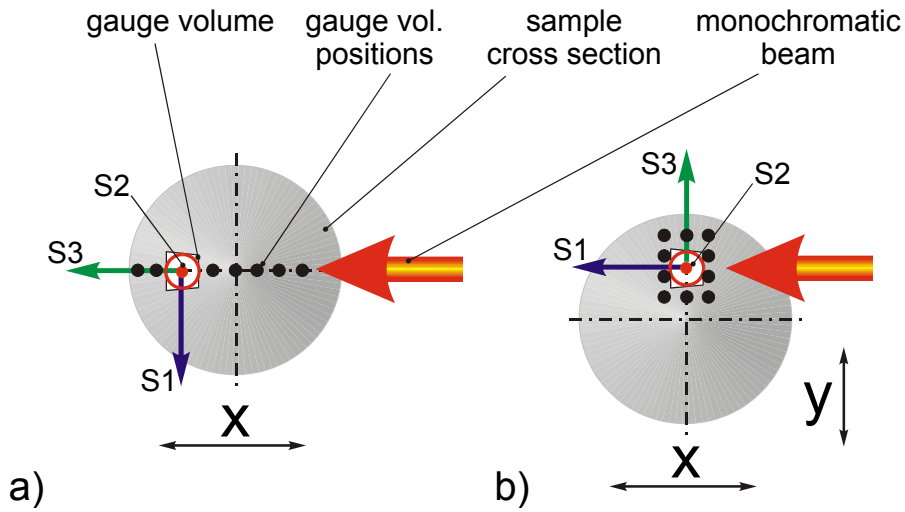

Figure 4.10: Scheme of the gauge volume positions, symbolized by black dots, within the solid torsion samples and the orientations of the sample coordinate system S with respect to the gauge volume positions.

Furthermore, the reconstruction technique to be applied to the data (see chapter 4.2.3) requires for each y position a series of images taken at different x positions. A complete data set to characterise the radial dependent strain state within the solid torsion samples required a set of 71 positions with a step size of 200μm in x and of 400μm in y direction. Therefore, for each radial position at least five images were available.

4.2.2.2 Coordinate systems

Sample coordinate system

Since all the samples investigated were cylindric and because the deformation had in all cases a rotational symmetry relative to the cylinder axis, the same right hand sample coordinate system is used. The axis parallel to the cylinder axis is denoted by S2, the radial direction is indicated by the S3 axis, and the S1 axis points in tangential or hoop direction (see figures 4.5 and 4.10). The respective rotations are shown in figure 2.3. An exception exists for the ψ angle in the ε *vs.* $\sin^2\psi$ plots: In order to facilitate the comparison to classical ε *vs.* $\sin^2\psi$ plots the origin of this angle was changed according to the direction of interest in such a way, that the position $\sin^2\psi = 1$ always points in the direction of the strain component of interest.

Laboratory coordinate system

The right hand laboratory system is always defined so that the x axis coincides with the incoming beam and points in direction of the photon velocity vector. The z axis points in the vertical direction and consequently the y axis is the horizontal. The right hand rotations around x, y, and z axis are called χ, φ, and ω, respectively. For completeness, it should be mentioned that for convenience, during the data anaylsis, the sense of the χ angle was changed when a large area detector was used.

Crystal coordinate system

The crystal coordinate system is shown in figures 2.1 and 2.3. The Bunge convention for the Euler angles is used.

4.2.2.3 Stress-free lattice parameter, d_0

A complete stress tensor or a hydrostatic stress can only be calculated when the stress-free lattice parameter is known with an accuracy of better than roughly $1x10^{-5}$ [see Hau 1991 for an exhaustive discussion of this aspect]. In stress measurements on surfaces this is not necessary when the hypothesis can be made that the surface normal stresses are zero within the penetration depth of the x-rays [Ack 1996].

In the present measurements made in the bulk of the sample, the hypothesis $\sigma_{33} = 0$ does not hold in cases where the macrostress is assumed to be not equal zero.

When the assumption is made that the hydrostatic stress is zero, the d_0 can be estimated via the random walk procedure when a large number of reflections and sample positions was measured. This is, for example, the case for the energy dispersive measurements.

Another possibilty is to try to measure the actual d_0 of the material investigated. This was done on an undeformed annealed AlMg3 alloy tubular torsion sample, on the beamline BM16, at the ESRF. The absolute wavelength was calibrated beforehand with a NIST Si powder. The error on the d_0 value was about $\pm 5x10^{-5}$.

4.2.3 Data evaluation

4.2.3.1 Energy dispersive measurements

For each sample postion one energy spectrum was recorded. Peak overlap was not problematic in the present case because a single phase material of high crystal symmetry was investigated. The increasing FWHM of the peakprofiles, which increases with decreasing 2Θ value and increasing energy, is counterbalanced by the peak separation, which increases with decreasing Bragg angle [Pyz 2000a]. The peak positions were determined by a least square fitting of gaussian peak profiles and a background correction. The d values were calculated according to equation 2.3. The crystallite microstrains were calculated based on equation 2.22, using the d_0 value determined by the random walk procedure. These values were then used in the form of ε *vs.* $\sin^2\psi$ plots [Mac 1961] for comparison to simulation results.

4.2.3.2 Angle dispersive measurements

Surface strain measurements

The lattice strains measured at different ψ positions were evaluated according to the $\sin^2 \psi$ method [Mac 1961]. The XEC required for the calculation of the stresses were calculated according to the Kröner model [Krö 1958] using the single crystal elastic constants of Al [Lan 1]. These evaluations were performed using a software package developed by Genzel [Gen 1999]. It takes into account the various aspects of statistical and systematic errors, inherent to the method [Hau 1997].

Bulk strain and texture measurements with large area detector

The data recorded at the radial positions schematically shown in figure 4.10 were available as 2-dimensional images. Each image contained six complete Debye-Scherrer rings. After background subtraction and determination of the beam center, i.e. the common center of all the rings, the images were transformed to polar coordinates using the software Fit2D [Ham 1996] (see figure 4.11), hereby slicing the circles into 1000 sections.

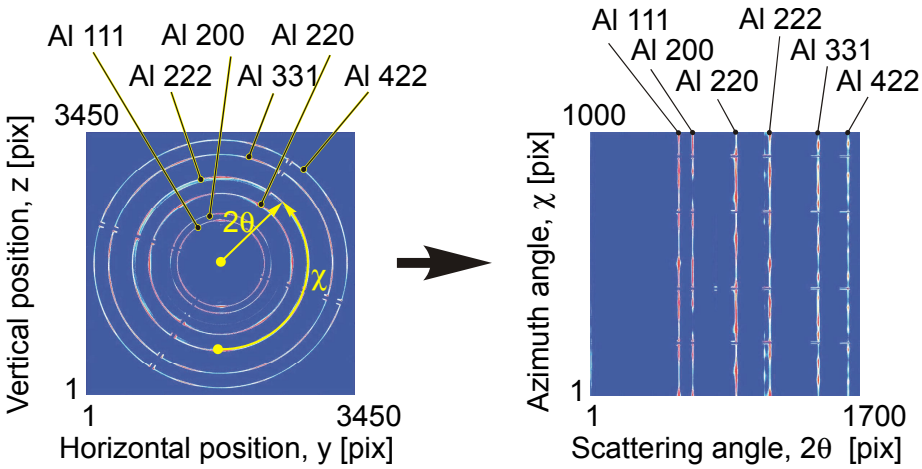

Figure 4.11: Transformation of data recorded with large area detector

This strategy, proposed by Wanner *et al.* [Wan 2000], allows the analysis of diffraction rings which have no smooth azimuthal intensity distribution. Before the least square fitting of a linear background and Pseudo Voigt profiles to the peak pattern of single pixel rows, a reconstruction procedure had to be applied to the data [Lie 2000c]. This reconstruction allows for the coupling of the local strain and the

local position of the gauge volume within the sample. Afterwards the results of the fit were rebinned to azimuthal sections of 5°.

Applying the appropriate coordinate transformations and absorption corrections to the integrated intensities, obtained from the least square fitting, the data was then used to calculate the radially dependent ODF, based on the BEARTEX software [Wen 1998].

The complete radially dependent pseudo macrostrain tensor (see ch. 2.4.2) was calculated for each measured reflection from the distortion of the diffraction rings. This requires the knowledge of the unstrained lattice parameter d_0, and the correction of the data for systematic distortions, caused by, for example, the detector system itself and the geometry of the experimental setup. The distortions were corrected by calculating the strains relatively to the supposedly strain free diffraction rings of an Al powder reference. The strain tensor components were then determined by fitting the parameters of the general equation 2.34 [He 1998] to the corrected peak positions (see figure 4.12). The fitting routine is based on a singular value decomposition algorithm [Pre 1992].

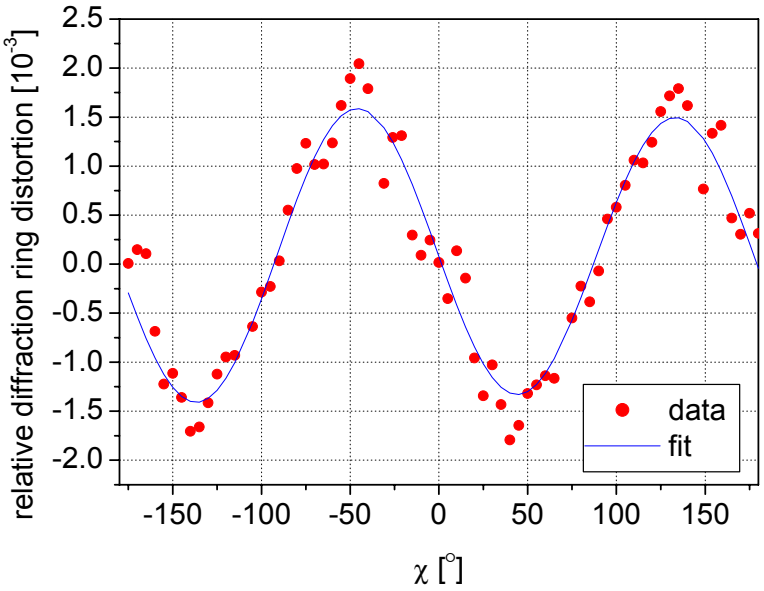

Figure 4.12: Example for a fit of equation 2.34 to the experimental data. Note: only a part of the data set required for this fit is shown.

Based on the pseudo macrostrain tensors, the individual peak positions, and the radially dependent ODFs, the residual stresses were then calculated according to the equations given in chapter 2.

Bulk strain measurements with small area detector

2-dimensional data was collected with the small area detector, each image representing an azimuthal section of the diffraction ring (see table 4.4) for a given reflection and sample position. After background subtraction, averaging over the azimuthal section, and reconstruction of the data [Lie 2000c], a Pseudo-Voigt profile was fitted to the peak by the least squares method. The pseudo macrostrain tensors were then calculated using the same algorithm as in the case of the data evaluation for large area detectors. But, in the present case, the strain free lattice parameter was determined by the random walk method, assuming the hydrostatic stresses to be zero.

The number of data points were not sufficient to calculate the radially dependent ODF. Therefore, the calculations of the stresses were made, assuming quasi-isotropy.

Bulk strain measurements with point detector

The spectra collected in the experiments on the beamline BM16 were in form of the measured intensity as a function of the absolute angular position of the point detector. The individual diffraction peak positions for each sample orientation were determined by least square fitting of a Pseudo Voigt profile. These experiments permitted also the determination of the strain free lattice parameter d_0, determined on undeformed tubular torsion samples. The strain was calculated according to equations 2.2 and 2.22. These values were then represented in form of ε *vs.* $\sin^2\psi$ plots [Mac 1961] for comparison to simulation results.

Data reconstruction technique

The aim of the strain measurements is the determination of the difference between the peak position of a diffracted beam, emanating from a local volume within a sample, and the peak position from an ideally unstrained reference sample. In figure 4.13, this reference beam position is represented by the solid line at an angle of $2\Theta_0$ to the incoming beam. The origin of this line coincides here with the origin of the laboratory coordinate system x_0 and the point where it impinges on the area detector, placed at the z axis, is the detector reference point z_0. The beam passes the slit that defines the local gauge volume within the strained sample.

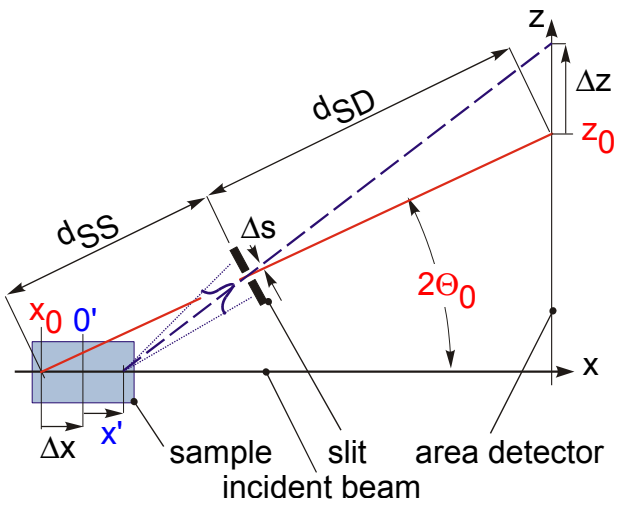

Figure 4.13: Ray diagram and coordinate system describing the relations between sample position, gauge volume position and beam positions on the area detector placed perpendicular to the x axis at the position of the z axis (see chapter 4.2.3.2 for further explanations).

The slit opening is Δs. The respective distances between sample, slit, and detector are called d_{SS} and d_{SD}. The strained sample is positioned with its center $0'$ at the position Δx. Due to the finite width of the reflection, only part of the rays emanating at the position x' are recorded on the detector at the distance Δz, relative to the reference position z_0. It is clear that beams impinging on the detector can have their origin at different positions x'. Therefore, it is not possible to obtain the peak position for a specific x' from a single recorded intensity distribution. A series of images has to be taken in a sufficient step width and range along x in order to assure that the signal originating in x' can be completely detected, though split up on several images. The diffraction peaks for each position x' can now be reconstructed using equation 4.1 [Lie 2000c]. The equation permits the calculation of the source point x' of each beam detected at a position Δz on the detector.

$$x' = b \cdot \Delta z \left[1 + \frac{\Delta z}{d_{SD} \cdot \sin(2\theta_0)} \right]^{-1} - \Delta x \quad \text{with} \quad b = \frac{d_{SS}}{d_{SD} \cdot \tan(2\theta_0)} \tag{4.1}$$

4.2.4 Experimental errors

4.2.4.1 Statistical errors

The statistical errors depend on the method applied to determine the diffraction peak positions and on the properties of the measured spectra such as counting statistics, signal to background ratio, FWHM of the measured peaks, overlapping of peaks, and the number of data points per peak [Bev 1992].

The peak overlap and peak FWHM can present a problem in the evaluation of the energy spectra recorded in energy dispersive measurements [Pyz 2000a]. In the data evaluation the resulting confidence intervals were calculated from the errors in the determination of the peak position.

In the experiments using the angle dispersive technique, the errors in the peak position on average ranged from 0.6 to $5x10^{-5}$ (average error: $2x10^{-5}$). They were neglected in the estimation of the resulting errors for the experiments on the beamline ID11, since their average was about one order of magnitude smaller than the systematic errors.

4.2.4.2 Systematic / instrumental errors

The main drawback and limitation of the energy dispersive technique is given by the energy resolution of about 200eV of the available detectors. The dependence of the gauge volume irradiation on the energy, due to absorption effects, can present a problem in some particular cases: Shifts of reflection positions of higher order might not correlate with the reflections of lower order when the specimen is made of a high Z material and when a significant macrostrain gradient is present. But this error is not of importance here due to the fact that Al is a low Z material and that no macrostress gradients were assumed to be present within the investigated samples.

The instrumental errors in the experiments on the beamline BM16 were negligible since alignment errors are compensated for by the use of a parallel x-ray beam. The errors introduced due to the fact that the scattering vector was inclined by the Bragg angle with respect to the sample rotation axis (see figure 4.7) were estimated to be in average $4x10^{-5}$ (see chapter 4.2.5.1). For the assessment of the strains measured it has also to be taken into account that the measurements represent an integration over the wall thickness of the tubular torsion samples. The difference in deformation between the outer side and the inner side of the tube wall was calculated to be 20%, representing a compromise between mechanical and geometrical stability of the sample during deformation and a not too steep deformation gradient across the wall thickness. The uncertainty for the measured d_0 value of $5x10^{-5}$ was judged to be negligible in these evaluations since no complete strain tensor was derived.

The principal instrumental error sources in the experiments on the beamline ID11, using an angle dispersive technique with a triangulation slit / conical slit system, were

the slit system itself and detector system. A more thorough discussion will be made in chapter 4.2.5.3.

4.2.5 Verification of techniques

4.2.5.1 General verifications

In all the measurements made with synchrotron radiation the samples were always aligned such that their longitudinal axis was perpendicular to the incoming beam. That implies that the scattering vector q (i.e. the bisector of incoming and reflected beam) deviated for each measured reflection by the Bragg angle from the intended measuring direction. Due to the use of high energy x-rays, the maximum Bragg angle was about 10° (Al 222 at $\lambda = 0.40576$Å). The assumption that this deviation is negligible for the measurements of crystallite microstrains was verified by comparisons of measurements on the Al 111 and Al 222 reflection, shown in figure 4.14. The average deviation between the two profiles is 5×10^{-5}. However, it has to be noted that the algorithms for the calculation of the strain tensors based on equation 2.34 and the ODF calculations accounted for the different q vector orientations.

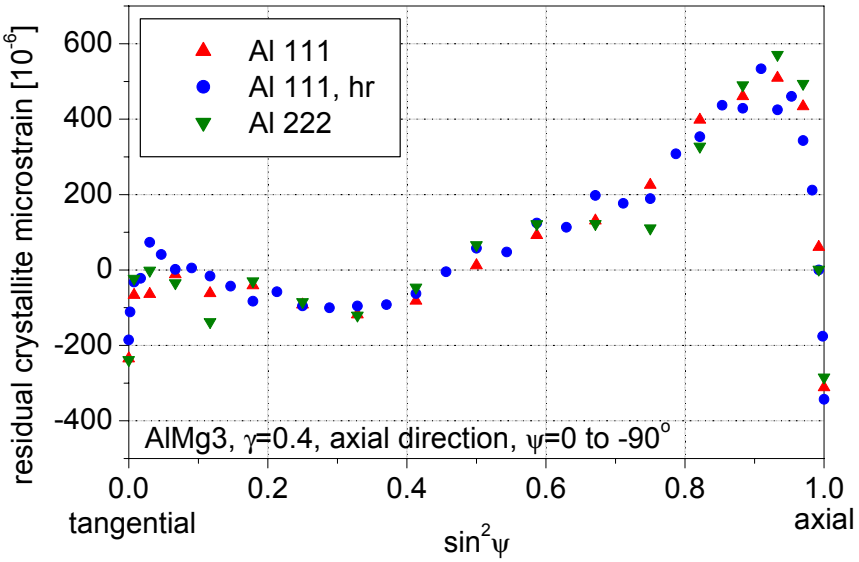

Figure 4.14: Plot of the crystallite microstrains *vs.* $\sin^2\psi$ for the axial direction of a tubular AlMg3 alloy torsion sample, plastically deformed to $\gamma = 0.4$, measured on the Al 111 and Al 222 reflections with a step size in ψ of 5° and 2.5° (marked hr for "high resolution").

Furthermore, a measurement of the Al 111 reflection was performed with a step size in ψ of 5° and 2.5° in order to check if an azimuthal angular resolution of 5° is sufficient without losing major features in the profiles. The curves in figure 4.14 show that the larger step size is sufficient.

4.2.5.2 Coarse grain effects

One of the general problems when performing strain or texture measurements with x-rays using a gauge volume much smaller than 0.1mm^3, is the average grain size of the material investigated. Conclusions on the macroscopic level can be false due to the fact that too few grains have contributed to the measured interference line. Estimations of the influence of the grain size and the gauge volume have been proposed by Lienert *et al.* and by Pyzalla [Lie 2000b and Pyz 2000a]. To diminish the influence of the coarse grain effects, the sample can be oscillated, either in rotation or in translation but it has to be noted that a combination of several oscillations requires an increased speed for each additional movement in order to irradiate the resulting gauge volume homogeneously. More than one oscillation direction becomes impractical when detector exposure times are of the order of a few seconds. Furthermore the oscillation range should not significantly deteriorate the spatial resolution. In the experiments discussed here, tests have shown that the linear oscillation in the ranges given in table 4.4 was by far the most effective compared to angular oscillation. For the torsion samples an angular oscillation would have been limited to a range of ±5° due to the deformation device and the requirement not to degrade significantly the spatial resolution.

To assess how many grains within the irradiated effective volume are contributing to the signal detected at a specific position, first the number of illuminated grains has to be calculated. In fact, it should be considered how many grains are intersected by the effective gauge volume. In the experiments discussed here, the horizontal size of the beam is much smaller than the length of the illuminated effective volume and its height, given by the linear oscillation range. The division of the gauge volume by the average grain volume would give misleading results. This is easily understandable when considering a gauge volume of say 10x10x500μm^3 and a grain size of 60μm. The result would be that less than one grain contributes to the diffraction pattern. Instead, based on the intersections, the number of (partially) irradiated grains can be estimated according to:

$$N_g = ceil\left(\frac{l}{d_g}\right) \cdot ceil\left(\frac{v}{d_g}\right) \cdot ceil\left(\frac{h}{d_g}\right) \quad (4.1)$$

N_g: Number of (partially) illuminated grains

l: Gauge volume length

v: Effective vertical gauge volume size, e.g. the linear oscillation range

h: Effective horizontal gauge volume size

d_g: Grain size

The expression *ceil* means that the result of the division is rounded towards the greater integer, therefore it will be always at least 1.

In the next step it has to be estimated how many of these grains are actually diffracting, when considering only one reflection. This depends on the mosaic spread of the material, the multiplicity of the reflection of interest, and, if applied, the range of the angular oscillation. The fraction of diffracting grains can then be estimated based on equation 4.2 [Lie 2000b], assuming a uniform texture.

$$N_{dg} = N_g \cdot \frac{J\ (\Delta\omega_g + \Delta\omega_o)}{2} \quad (4.2)$$

N_{dg}: Number of diffracting grains, assuming uniform texture

N_g: Number of (partially) illuminated grains

J: Multiplicity of the reflection

$\Delta\omega_g$: Mosaic spread of the grains in radians

$\Delta\omega_o$: Angular oscillation range in radians

This number relates to the complete diffraction ring. Therefore in the last step it has to be estimated how many grains are contributing to the observed azimuthal section of the diffraction ring. This can be, for example, the section of the diffraction ring accepted by a point detector or in case of an area detector the azimuthal range over which the diffraction rings are averaged for the later evaluation.

$$N_{odg} = N_{dg} \cdot \frac{\chi_a}{2\pi} \quad (4.3)$$

N_{odg}: Number of observed diffracting grains

N_{dg}: Number of diffracting grains

χ_a: Azimuthal average range in radians

Values for the mosaic spread of Al grains of up to 0.12rad were reported by Poulsen *et al.* [Marg 2001, Pou 2001].

Based on a mosaic spread of 0.12rad, a grain size of 60μm, and the values given in table 4.4 the calculations yield an estimation that, for a total number of illuminated grains of N_g = 760, on average, N_{odg} = 10 grains contribute to each 5° section of an individual diffraction ring, in the case of the experiments on the beamline ID11. At first this might seem very few but it has to be considered that, in case of the evaluation of crystallite microstrains (see chapter 5.2.3.3), this number of contributing grains is doubled because the information of one azimuthal section can be averaged with the diametrically opposed one, which contains essentially the same information. An error estimation of 1.8×10^{-4} for the crystallite microstrains, based on the division of the average range for the microstrain divided by the square root of N_{dog} = 20, is in good agreement with the average microstrain differences of about 1.5×10^{-4} between the diametrically opposed ring sections. In the case of the determination of the pseudo macrostrain tensor (see chapter 5.2.3.3), the number of grains is even higher since at least five complete diffraction rings are evaluated per gauge volume position (see chapter 4.1.2.2).

The number of observed diffracting grains per reflection and sample position in the case of the energy dispersive measurements on the beamline ID15A, was about N_{odg} = 15. Due to the very large gauge volume, N_{odg} is estimated to be over 480 for the measurements on the tubular torsion samples on the beamline BM16.

4.2.5.3 Verification of the strain measurements with the conical slit cell

The following section will address the verification of the strain and texture measurements by means of the 2nd generation conical slit system and a large area detector. The section is subdivided into parts treating the constitutive elements of this technique which are: The achievable spatial resolution, the 2nd generation conical slit cell, and the large area x-ray detector. However, for detailed aspects of the beam focussing elements and the focal characteristics the author refers to the publications by Schulze *et al.* and Lienert *et al.* [Schul 1998, Lie 2001].

Spatial resolution and reconstruction technique

First feasibility experiments on the spatial resolution using the crossed beam technique, involving a triangulation slit and a point detector (see chapter 2), were made on a shot peened Al sample that had already been measured employing different techniques using neutrons and synchrotron x-rays [Web 1998]. The results of this verification experiment [Lie 2000a] proved that the crossed beam technique combined with the data reconstruction technique provides sufficient longitudinal spatial resolution, corresponding to theoretical calculations, to resolve the strain in the shot peened region. The combination of these techniques was then used to investigate the strain distribution in a plastically deformed solid AlMg3 alloy torsion sample. It was shown that the techniques could be used to resolve the steep strain gradient in the sample center, which is present at an angle of 45° to the torsion axis and to confirm the point symmetry of the strain profile (see figure 4.15) [Mart 1999]. The point symmetry is inherent to this component since the observation direction changes with respect to the sample coordinate system when crossing the sample center.

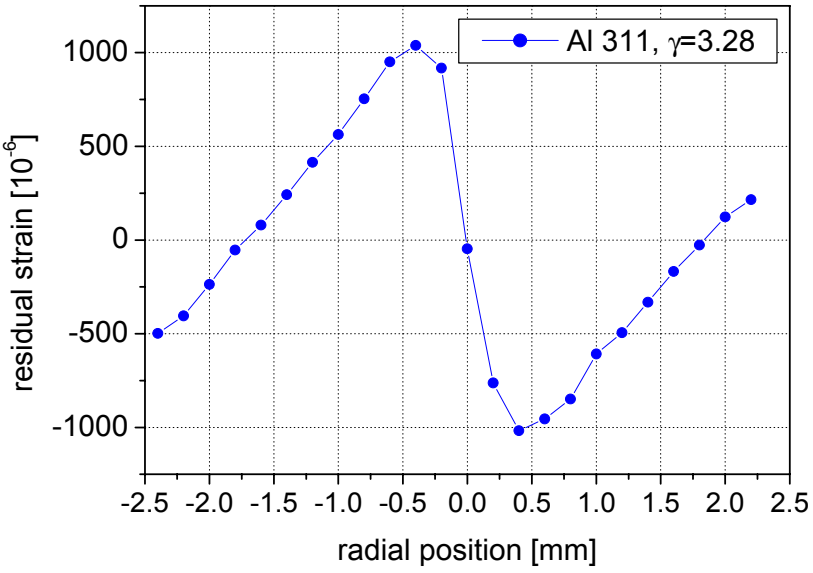

Figure 4.14: Strain profile within solid AlMg3 alloy torsion sample, plastically deformed to $\gamma = 3.28$, measured on the Al311 reflection, in the direction of the shear component, at 45° to the torsion axis.

Conical slit cell

Measurements of the slit gaps of the 2nd generation conical slit system by optical microscopy gave a result of 25μm. The slit system was mounted on a dedicated alignment stage. After prepositioning the alignment of the slit system was optimized by moving a 150μm thick Al powder sample along the incoming beam through the focus of the x-ray beam which has to coincide within a few μm with the focus of the conical slit cell. To obtain smooth powder rings the sample was spinning around the incoming beam. For each sample position an image of the diffraction pattern was recorded with a large area detector placed behind the slit system. From a first data set the optimum alignment of the slit could be calculated. After this optimization another series of images was recorded to assess the longitudinal gauge volume size defined by each cone and the deviations in longitudinal direction from the theoretical common apex of the cones. This deviation is a function of the concentricity of the apertures as well as the radius and cone variations. It was found that the standard deviation from the common apex was 12μm (i.e. about 2%), which was judged to be satisfying. This value was improved in later experiments where translation stages for the alignment of the slit system were used that had a step size of 1μm instead of 5μm. Table 4.5 gives an overview of the gauge volume lengths, experimentally determined from the FWHM of the intensity *vs.* powder sample position profiles. The longitudinal resolution should improve by a factor of two if the detector resolution can be enhanced by the same factor. Monte Carlo simulations [Lie 2000d] of the beam path and the conical slit system showed that the thickness of the slit of 2mm did not cause significant clipping of the beams selected by the slit system.

Large area detector

The large area detector used for the experiments presented in this work was a MAR 345 online image plate scanner with an active area of 3450x3450 pixels and a pixel size of 100μm. Strain measurements require usually the detection of radial variations of the diffraction ring diameter within an accuracy of $1x10^{-4}$ or better. As indicated beforehand, the longitudinal resolution of the gauge volume depends also on the spatial resolution of the detector system used. This spatial resolution is mainly given by the point spread function (PSF) [Neu 1993]. In the present case it was determined from the projection of a 100μm wide slit, placed directly on the detector. The radial resolution was found to be 310μm at a beam energy of 55keV. The critical

value above which the detector resolution deteriorates the spatial resolution, given by the slit system and the focus size, can be estimated with:

$$PSF = \Delta s \cdot \frac{d_{sd}}{d_{ss}} \qquad (4.4)$$

PSF: Point spread function of detector

Δs: Gap of triangulation slit

d_{sd}: Distance between detector and slit

d_{ss}: Distance between sample and slit

For the present setup this value was about 120μm. Thus, the resolution of the detector degraded the spatial resolution by a factor of about 2.5. Presently there are no affordable large area detectors available which have a better resolution.

The detector was tested by evaluating the images of the diffraction rings of the thin Al powder sample. Since the powder was spun during the detector exposure and assumed to be stress-free, the Debye-Scherrer rings should be perfect circles. The radial spatial distortions induced by the present detector system are insignificant since basically the diffracted beams pass no optical elements (e.g. lens systems) before impinging on the fluorescent layer of the image plate. The observable distortions of the patterns, which have an azimuthal period of 2π, are mainly due to the fact that the image plate normal is not parallel to the incoming beam. A transformation of the patterns to polar coordinates and applying a geometrical correction for this misalignment using the software Fit2D [Ham 1996] (see figure 4.11) results in an interference line pattern where the previous rings are straight within $\Delta\Theta / \Theta = 1\text{x}10^{-4}$. After the transformation, the radial variations are dominated by pixel to pixel oscillations. By an azimuthal averaging over 5°, these fluctuations reduce to about $2\text{x}10^{-5}$.

Distortion corrections

Combining all the optical elements and the area detector results in a systematic distortion of the diffraction rings in the range of $\pm 4\text{x}10^{-4}$. To correct these distortions, the diffraction data taken on strained samples has to be corrected with the distortion measured on diffraction rings of an unstrained powder sample. The powder sample does not necessarily need to be made of the same material as the strained sample as long as the lattice parameters of both materials are known to roughly within

$1x10^{-5}$. It is important that the diffraction peaks of interest are close to each other, within a few percent, since these distortions are assumed to have a smooth distribution over the entire detector area.

Determination of complete strain tensor

The validity of the results from the determination of the complete strain and stress tensors are based on the stress equilibrium conditions (see chapter 2) and on the uniqueness of the stress / strain relationship, which means that the same state of stress cannot lead to two different states of strain [Cra 1959]. In the case of the torsional deformation of solid cylindrical samples, this results in the condition that the tensor components $\varepsilon 13$ and $\varepsilon 23$ have to be zero, for the given sample coordinate system (see figure 4.10).

In the case of the stress within a torsion sample, where the stress state has a rotational, symmetry the equilibrium is assured per se for the radial, the tangential, and the off-diagonal components (see e.g. figure 4.14 for the $\varepsilon 12$ component) because their direction changes depending on the position in the sample with respect to a fixed point outside the sample coordinate system. Only the axial component points always in the same direction and is, as a consequence, not self-equilibrating. Therefore the validity of the data obtained can be checked by verifying that the equilibrium condition is fulfilled in direction of the axial stress component.

Because the Bragg angles are rather small, due to the short wavelength of the x-radiation, the uncertainty for the diagonal components of the strain tensor are almost identical to the uncertainty for the strain free lattice parameter d_0. This can be explained by the fact that any small change of the d_0 corresponds to a change of the apparent hydrostatic stress, which has only an impact on the diagonal tensor components. Therefore, the determination of the off diagonal tensor components is not sensitive to uncertainties in d_0. The uncertainties between the components within one group (i.e. diagonal or off diagonal) is estimated from the deviations of the data points to the fit of equation 2.34. The average error for the pseudo macrostrain tensor components is usually below $\pm 1x10^{-4}$. This value can be considered as an upper bound since the linear model represented by equation 2.34 can not actually fit correctly strain data showing strong non-linear crystallite microstrains (see chapter 2.4.2).

4.2.5.4 Verification of texture measurements

Since the calculation of the ODF was based on incomplete experimental polefigures, it was necessary to assess the sensitivity of the WIMV algorithm [Mat 1982], used for the calculation of the ODF, to perturbations in the form of missing data points.

In a first step, complete polefigures for the reflections, available with the conical slit cell setup, were recalculated from an ODF that represented a torsion texture. This set of polefigures will be called set1. Afterwards the ODF was calculated again from set1 in order to check the reproducibility. The resulting set of polefigures, calculated from a recalculated ODF, is called set2. The criteria for the assessment were the differences and the standard deviation between set1 and set2. The average deviations between set1 and set2 were 2%, for this reproducibility check, and therefore negligible. In the next step, the ODF was calculated using incomplete polefigures of set1 as input. The output was, again, an ODF from which a new set2 of polefigures was calculated for the comparison to set1.

The overall conclusion was that:

- The higher the index of the reflection, the lower the sensitivity of the recalculated polefigures to incomplete input polefigures.
- The less complete the input, the greater the differences between set1 and set2. The average difference was 10% in the case of an input polefigure with coverage of 26% (with the maximum of 14% for the 111 polefigure and the minumum of 6% for the 422 polefigure).
- The differences decrease to an average of about 6% when the input polefigures cover the regions that contain the typical features of the respective texture (with the maximum difference of 11% for the 111 polefigure and the minumum of 5% for the 422 polefigure).

The experimental polefigures, from the measurements presented here, had usually a 36% completeness, covering most of the typical torsion texture features. The recalculated polefigures are judged to be sufficient for a description of the texture development. However, conclusions based on small details in the polefigures have to be made very carefully and it has to be considered that individual points in the polefigures might have errors of up to 60%.

5 RESULTS AND DISCUSSION

5.1 Microstructural changes due to plastic deformation

5.1.1 AlMg3

5.1.1.1 Investigations by optical microscopy

The initial grain size of the sample material (i.e. before deformation) was determined on optical micrographs using the line cut method [Schu 1991]. The AlMg3 alloy had an average grain size of 60µm. Figure 5.1 shows the optical micrograph of the cross section of a solid torsion sample deformed at room temperature to γ = 2.88. The zone displayed has undergone a deformation of γ = 1.7 (Note: The deformation depends linearly on the radial position within the sample). For some grains a break up into smaller lamellar subgrains (about 10 to 15µm wide) is clearly observable.

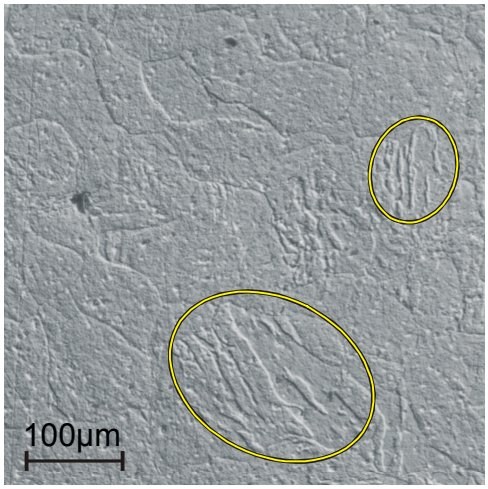

Figure 5.1: Optical micrograph of the cross section of the solid AlMg3 torsion sample. The displayed zone was deformed to about γ = 1.7 at room temperature. The circled areas show grains, broken up into subgrains. Etched for 50s in 1mol % NaOH solution at 50°C.

5.1.1.2 Investigations by TEM on AlMg3 alloy solid torsion samples

All these investigations were performed with a PHILIPS EM400 TEM working at an acceleration voltage of 100kV though the microscope can provide a maximum of 120kV.

Microstructure at low strains, $\varphi = 0.1$

The specimens taken from the radial position $r \approx 0.3$mm (see chapter 4.1), corresponding to a deformation $\varphi = 0.1$, showed three types of microstructures. The first one (see figure 5.2) can be described as a fairly uniform distribution of dislocation tangles. The zigzag shaped lines, marked LCD, might be attributed to Lomer-Cottrell dislocations [Ver 2001].

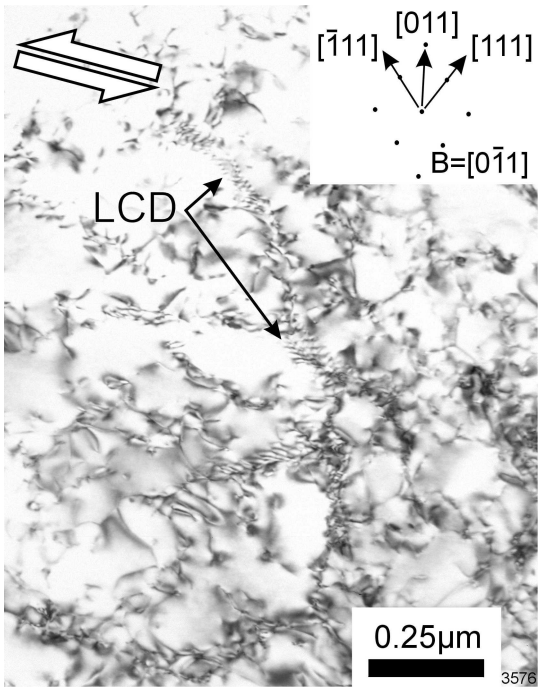

Figure 5.2: TEM micrograph of AlMg3 deformed in torsion to $\varphi = 0.1$, exhibiting a fairly uniform distribution of dislocation tangles. The zigzag shaped lines denoted with LCD might be attributed to Lomer-Cottrell dislocations. The double arrow indicates the shear direction.

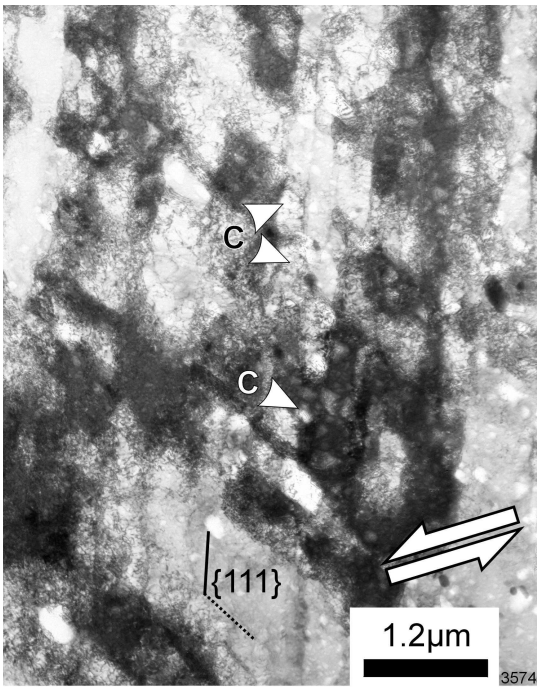

Figure 5.3: TEM micrograph of AlMg3 deformed in torsion to $\varphi = 0.1$ (different region than in figure 5.2), showing a diffuse chequerboard or cell block pattern. The double arrow indicates the shear direction. Solid line: trace of the {111} plane perpendicular to paper. Dotted line: trace of the {111} plane 50° to paper

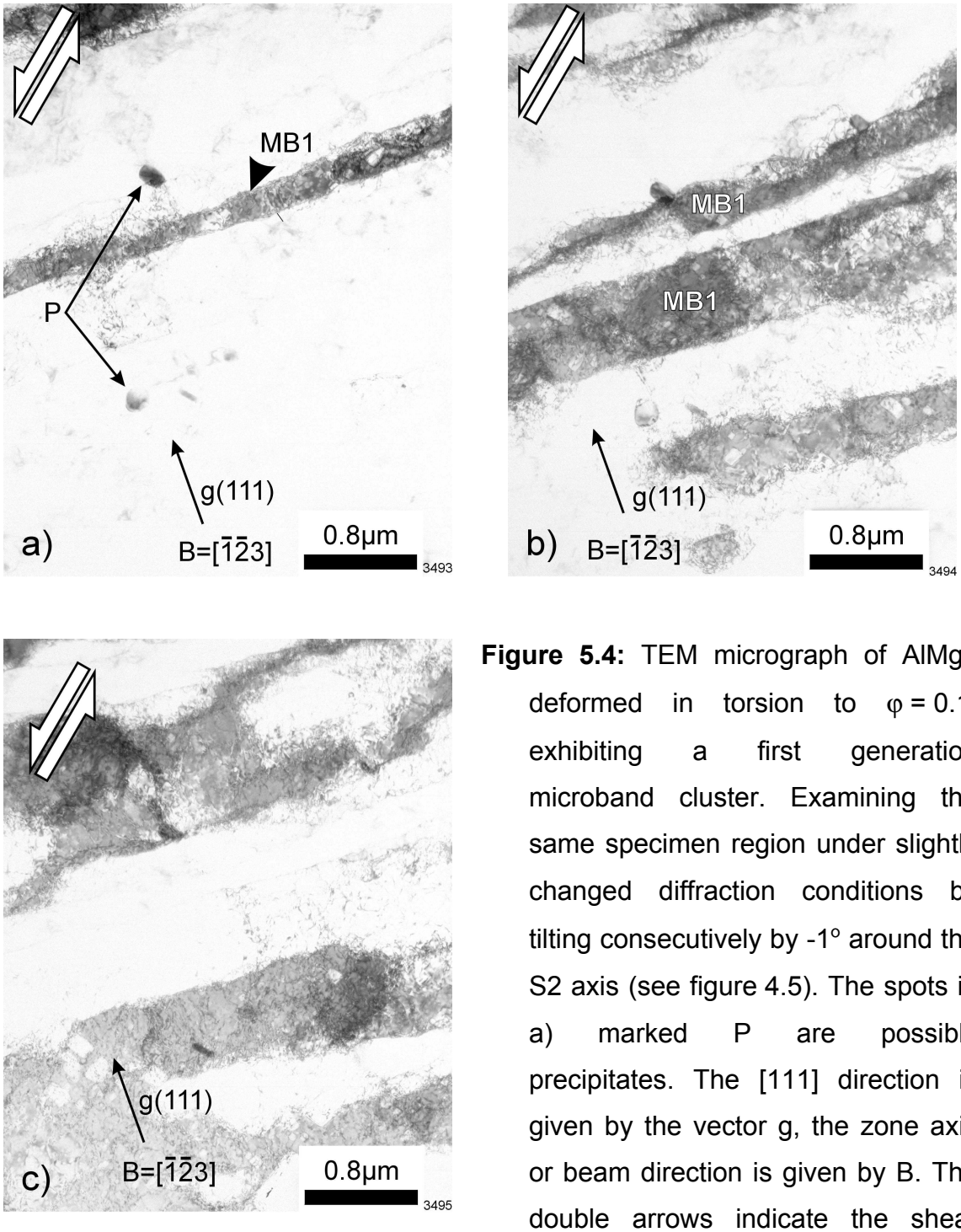

Figure 5.4: TEM micrograph of AlMg3 deformed in torsion to $\varphi = 0.1$, exhibiting a first generation microband cluster. Examining the same specimen region under slightly changed diffraction conditions by tilting consecutively by -1° around the S2 axis (see figure 4.5). The spots in a) marked P are possibly precipitates. The [111] direction is given by the vector g, the zone axis or beam direction is given by B. The double arrows indicate the shear direction. Square shaped features are artifacts due to the specimen preparation.

The second microstructure type is a diffuse "chequerboard" or cell block pattern. The diffuse aspect of the pattern is probably due to the low deformation and the presence of Mg. Long intersecting dark dislocation bands are observed parallel to the traces of {111} planes. They subdivide the region into cells with varying dislocation density. At this stage the structure looks similar to a Taylor lattice, but small cells, marked C, can be already seen. This interpretation is confirmed later by the observations on the specimen deformed to $\varphi = 0.3$.

A third microstructure type is shown in figures 5.4a to c. The TEM micrographs show a cluster of 0.2 to 0.6µm wide, first generation microbands (MB1) which are all aligned with a {111} plane. The micrographs show the same region under slightly changed diffraction conditions by tilting the specimen consecutively by -1° around the S2 axis (i.e. the shear plane normal, see figure 4.5). The complete vanishing of the MB1 after a small tilt suggests that its constitutive dislocations have similar Burgers vectors.

The spots, in figure 5.4a, marked P, could be Al_6Fe or (Al, Mg, Si) precipitates. Verdier [Ver 1998] reports for a Al-2.5wt.%Mg alloy, based on commercial purity Al (i.e. similar to the alloy used here), coarse Al_3Fe precipitates of 1µm diameter and fine precipitates of 0.15 to 0.3µm diameter of Al_6Fe and (Al, Mg, Si) precipitates. Verdier concludes from comparisons with a high purity Al-2.5wt.%Mg alloy that no differences in the dislocation arrangements are observable for strains of $\varphi \geq 0.4$. Thus the influence of the precipitates on the dislocation patterns is not very strong.

Microstructure at low strains, $\varphi = 0.3$

The specimens taken from the region deformed to about $\varphi = 0.3$ show basically the same features as the lower deformed material. However some patterns are more pronounced. This is especially the case for the cell block structure, also called "chequerboard" pattern [Dul 1996].

Figure 5.6 shows a detail of a cell block structure. A first generation microband (MB1), consisting of two layers of small pancake shaped cells (SPC) delineates a cell block (CB). Some of the cells within the cell blocks are almost completely cleared of dislocations. Dense dislocation walls, delimiting cells, are distinguishable. They partly start to evolve into MB1s.

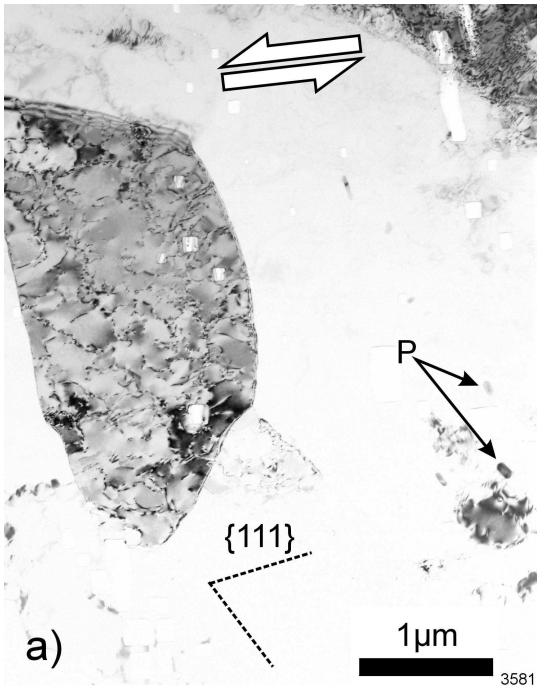

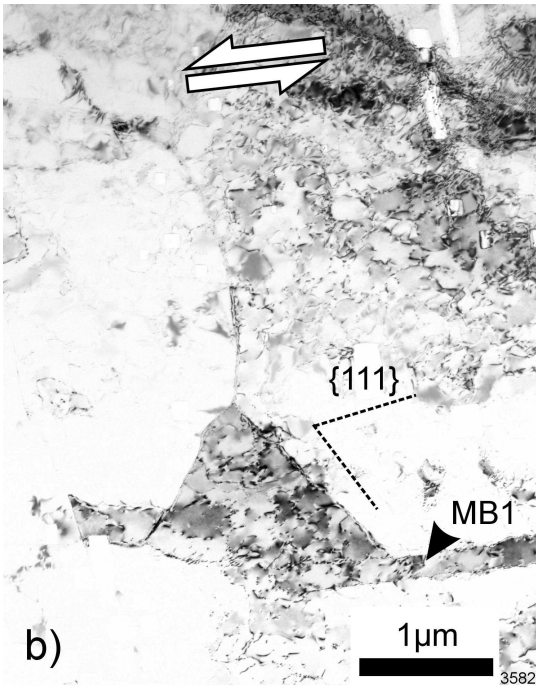

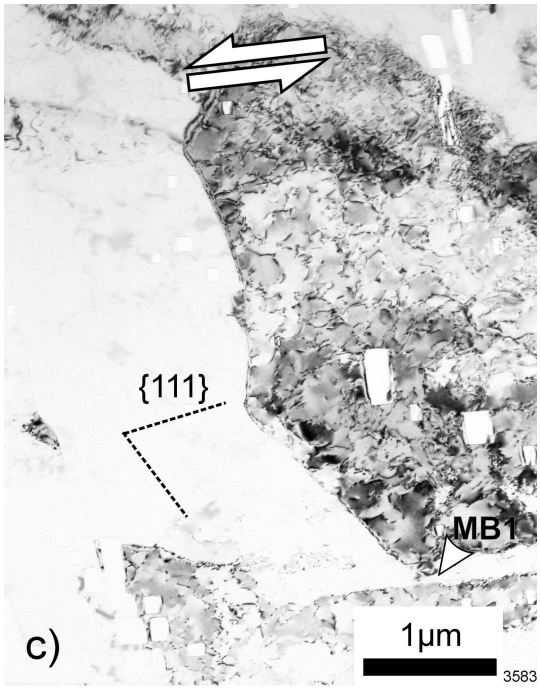

Figure 5.5: TEM micrograph of AlMg3 deformed in torsion to $\varphi = 0.3$, examining the same specimen region under slightly changed diffraction conditions by tilting consecutively by -1° around the S2 axis (see figure 4.5). The first generation microband appearing in b) and disappearing again in c) is marked MB1. The spots in a) marked P might be precipitates. The dashed lines mark the traces of {111} planes perpendicular to the paper, zone axis $B = [0\bar{1}1]$. The double arrows indicate the shear direction. Square shaped features are artifacts due to the specimen preparation.

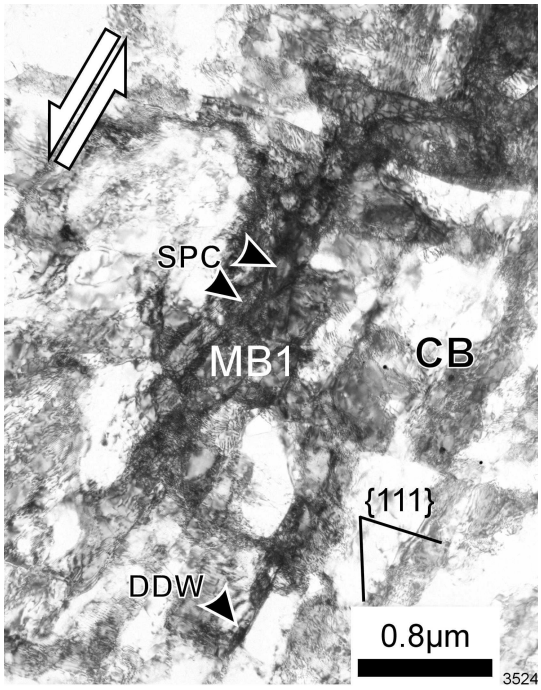

Figure 5.6: Deformation: $\varphi = 0.3$. Detail of further developed chequerboard [Dul 1996] or cell block structure showing dense dislocation walls (DDW) which separate cells in the cell block (CB). The first generation microband (MB1) consists of small pancake shaped cells (SPC). Solid lines are the traces of {111} planes perpendicular to the paper. The zone axis is [011]. The double arrow indicates the shear direction.

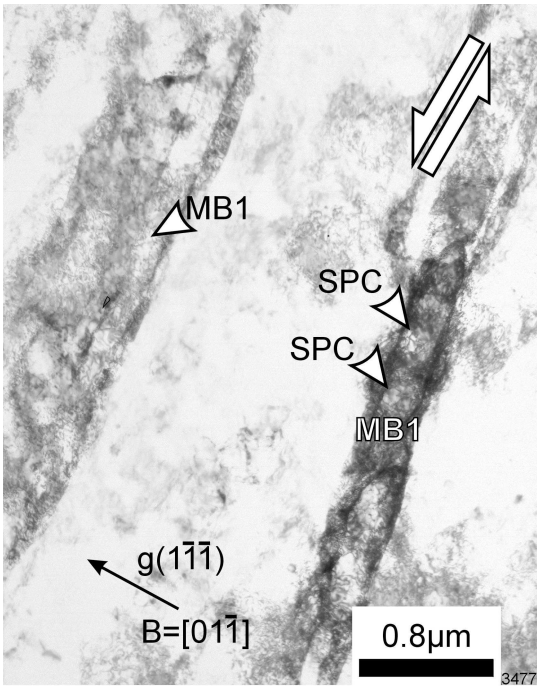

Figure 5.7: Deformation: $\varphi = 0.53$. First generation microbands (MB1) parallel to {111} plane and to shear direction, indicated by double arrow. Distinct small pancake shaped cells (SPC) are seen within one microband. g is the vector indicating the [$1\bar{1}\bar{1}$] direction. The zone axis or beam direction B is [$01\bar{1}$].

Figures 5.5a to c show three adjacent subgrains whilst varying the diffraction condition by tilting consecutively the specimen by -1° around S2 (see figure 4.5). Subgrains normally start to form at higher strains. The very fine subgrain boundaries (about 0.05µm) permit the conclusion that these clearly delineated subgrains are not due to the torsional deformation but originating from the heat treatment prior to deformation.

The vanishing and respective reappearing of the neighbouring subgrains after small tilts suggest that the misorientation between them are only small and that the uniform dislocation distributions within the subgrains have similar Burgers vectors. In figure 5.5b, a first generation microband MB1 appears parallel to the trace of a {111} plane and to the shear direction. It cuts through different subgrains. Moreover, a subgrain boundary parallel to the trace of a {111} plane is observable.

Microstructure at intermediate strain, $\varphi = 0.53$

At a deformation of $\varphi = 0.53$ only one type of microstructure was observed. As shown in figure 5.7, depending on the diffraction condition, very clear and long first generation microbands MB1 are visible, consisting of small pancake shaped cells SPC. Here the MB1s are parallel to {111} planes and to the shear direction.
Generally a depletion of the microstructure diversity is expected with increasing strain [Dul 1996] though it is astonishing to observe it at this relatively low strain. More samples would need to be investigated in order to see if this is due to a general trend or just because of an insufficient number of grains were studied with respect to statistical significance.

Summary of the TEM observations

In the specimens taken from low deformed regions (φ=0.1 and φ=0.3) three types of dislocation arrangements were observed. These were areas with almost uniformly distributed dislocations tangles, first generation microband clusters and "chequerboard" patterns. In the specimens taken from the intermediate deformed zone (φ=0.53) only one type of microstructure was observed, consisting of long MB1.
Shear bands, which normally evolve from first generation microbands via second generation microbands and which cut through several crystallites, were not observed. However, they are expected to appear at higher strains [Kor 1986].
The only close similarity to the microstructures observed by [Nak 1987] on cold rolled high purity AlMg3 single crystals are the clusters of first generation microbands. The main reason for this is certainly the fact that Nakayama investigated single crystals of high purity.
The observations reported here permit only limited general conclusions, mainly for two reasons: The initial grain size was too large and only six TEM specimens were

studied. Due to the initial grain size of 60µm, it is most likely that only a maximum of three or four grains was observable in one TEM specimen. Though [Dir 1995] observed in cold rolled Al+5at.%Mg, for different grain sizes, no qualitative differences in the microstructure, it is known that the microstructural development in a grain depends strongly on its initial orientation. Therefore, a larger number of specimens per deformation step or a smaller initial grain size is required for more generalized statements.

5.1.2 AlSi25Cu4Mg1

The average grain size of the Al matrix in the AlSi alloy, determined on optical micrographs using the line cut method [Schu 1991], was 5µm and the Si particle size ranged from 5 to 15µm (see. figure 5.8). Pyzalla *et al.* [Pyz 2000b] identified the intermetallic phases as Mg_2Si and Al_2Cu.

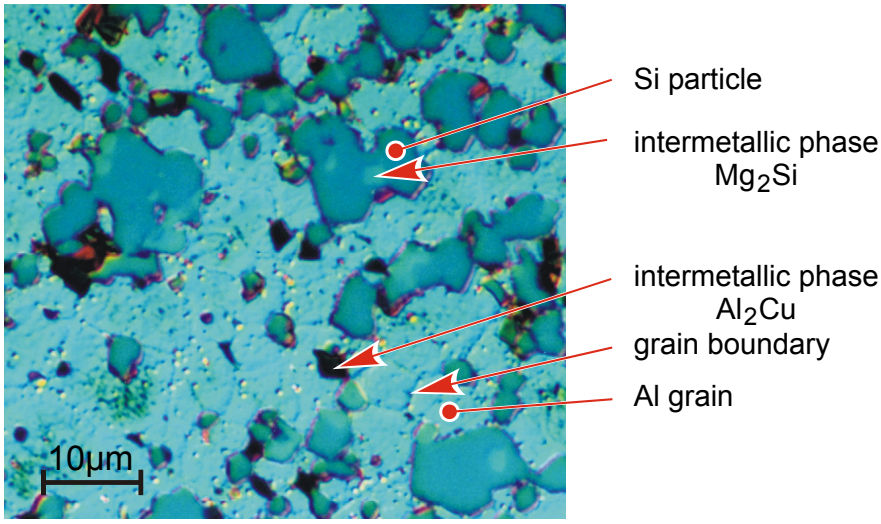

Figure 5.8: Optical DIC Micrograph of cross section of solid AlSi alloy torsion sample. The displayed zone is in the sample center and therefore almost undeformed. Etched for 50s in 1mol % NaOH solution at 50°C.

5.2 Analyses using synchrotron radiation and simulations

5.2.1 Uniaxial deformation

The experimental results of the measurements on compression and tensile samples made of the AlMg3 alloy were already published together with simulations of the crystallite microstrains by Aris [Ari 2000a]. Therefore, only a short section summarizing the most important aspects and figures will be dedicated to these experiments, which were carried out using the energy dispersive setup (see chapter 4.2.1.1). For the simulation a Taylor-Bishop-Hill-type model was used assuming isotropic linear hardening. The initial texture was represented by a set of 3821 individual grains.

5.2.1.1 Compression of AlMg3

The experimentally observed crystallite microstrains and intensities are presented together with the simulated ones in figures 5.9 to 5.12. The data is plotted in form of strain / intensity vs. $\sin^2\psi$. The letters L and T on the abscissæ indicate the load and the transverse direction respectively. The presented compression sample was deformed to $\varphi_v = 0.445$. This was the highest deformation possible before this sample type started bulging.

The simulations of the crystallite microstrains and the intensities for the 111 reflection are in good agreement with the experimental results (figure 5.9). The peak to valley value of 1200×10^{-6} in the microstrain profile is among the largest of the four reflections investigated, 111, 200, 220, and 311.

The largest crystallite microstrains are observed for the 200 reflection with a peak to valley value of 1500×10^{-6} (figure 5.10). Here, the simulations are in good agreement for the microstrain profile but less good for the observed intensity distribution.

The 220 reflection exhibits the weakest microstrains of the investigated reflections with a peak to valley value of about 600×10^{-6} (figure 5.11). The simulated intensities are in very good agreement with the experiment. The intensity profile is clearly indicating the 110 / 320 fibre texture, experimentally determined by Aris [Ari 2000a] in a separate experiment. At higher deformations a pure 110 fibre texture is expected [Was 1962, Dri 1978]. The modelled microstrains do not always follow the experimental observations.

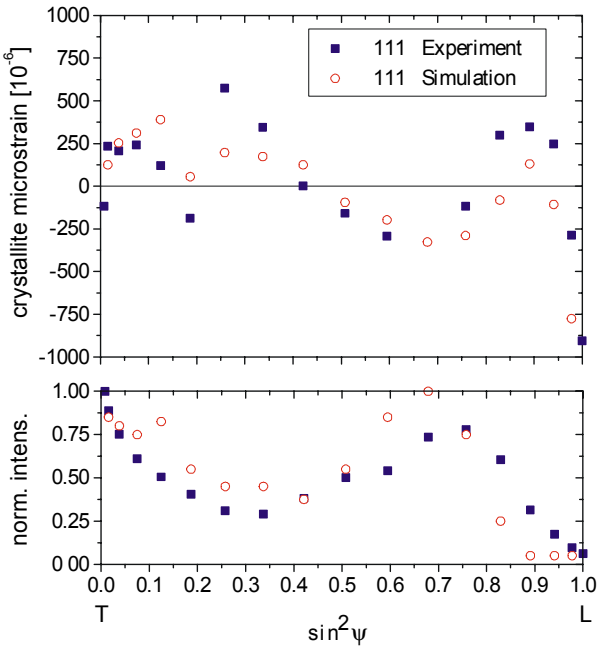

Figure 5.9: Crystallite microstrains and intensity distribution, AlMg3 compression sample, φ_v = 0.455, 111 reflection, T and L indicate transverse and load direction respectively, experimental uncertainty: ±150x10^{-6}

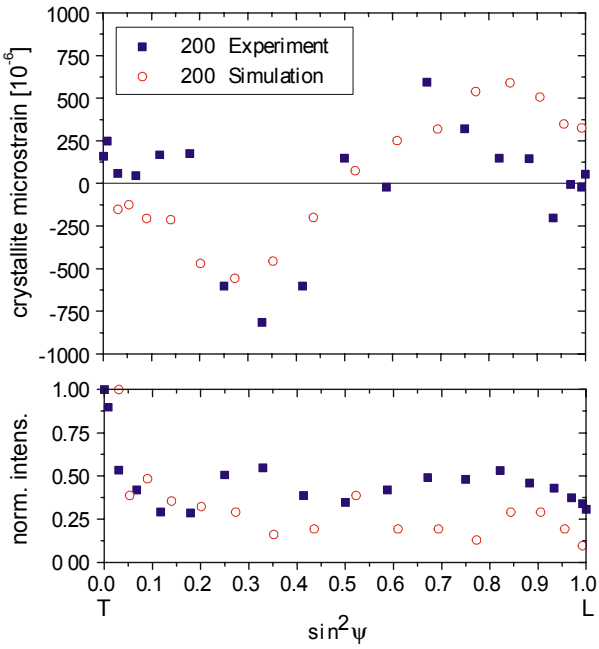

Figure 5.10: Crystallite microstrains and intensity distribution, AlMg3 compression sample, φ_v = 0.455, 200 reflection, T and L indicate transverse and load direction respectively, experimental uncertainty: ±150x10^{-6}

Figure 5.12 displays the results from the measurements on the 311 reflection. The intensity profile does not exhibit sharp peaks, which corresponds to the results of the texture measurements, showing that no strongly preferred orientations exist in the sample for this crystal direction. The simulation of the intensity, qualitatively, predicts well the experimental observations. Quantitatively, there are differences of more than 50%. The deviations of the simulated microstrains from the experimental ones are partially considerable but mostly they are within the experimental uncertainty of 150x10^{-6}. The magnitude of the peak to valley values of the crystallite microstrains is 1100x10^{-6}, similar to the observations for the 111 reflection.

Please refer to chapter 5.2.4 for a summary of the microstrains observed for the different deformation modes.

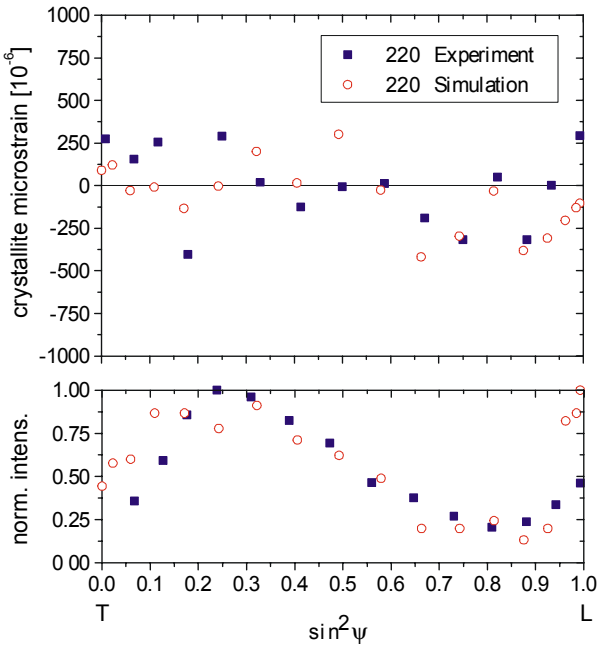

Figure 5.11: Crystallite microstrains and intensity distribution, AlMg3 compression sample, $\varphi_v = 0.455$, 220 reflection, T and L indicate transverse and load direction respectively, experimental uncertainty: ±150x10^{-6}

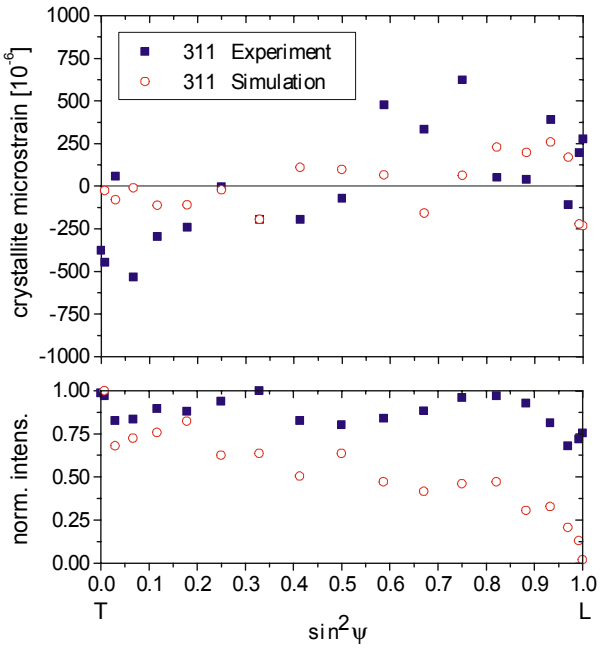

Figure 5.12: Crystallite microstrains and intensity distribution, AlMg3 compression sample, $\varphi_v = 0.455$, 311 reflection, T and L indicate transverse and load direction respectively, experimental uncertainty: ±150x10^{-6}

5.2.1.2 Tensile deformation of AlMg3

The results from the measurements on the tensile sample deformed to $\varphi_v = 0.24$, representing the highest achievable tensile deformation for these samples, are presented in figures 5.13 to 5.16 in the same form as the results for compression.

The simulations and experimental results for the 111 reflection (figure 5.13) are in good agreement and the differences are mostly within the experimental uncertainty. Contrary to the compression sample, the 111 reflection exhibits rather weak crystallite microstrains with a peak to valley value of 400x10^{-6}.

The 200 reflection exhibits, with a peak to valley value of 1000x10^{-6}, the largest crystallite microstrains (figure 5.14). The deviations between simulation and experiment are partially strong but the overall shape of the microstrain and intensity profiles is qualitatively close to the experimental ones.

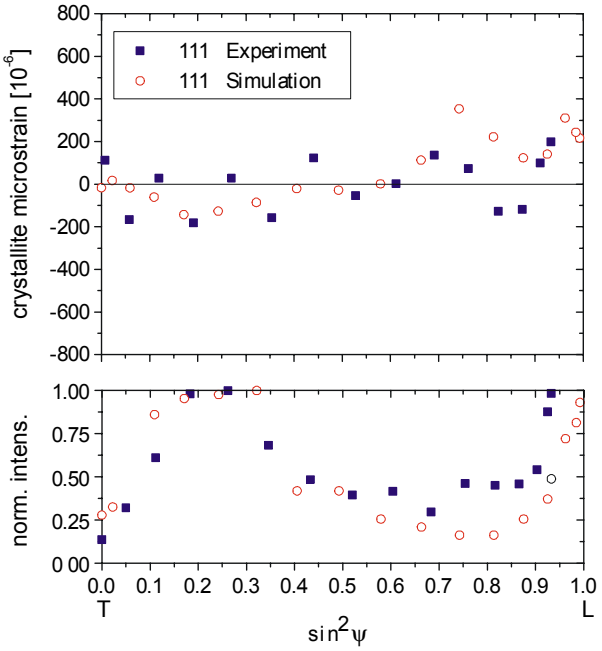

Figure 5.13: Crystallite microstrains and intensity distribution, AlMg3 sample, tensile deformation $\varphi_v = 0.24$, 111 reflection, T and L indicate transverse and load direction respectively, experimental uncertainty: $\pm 150 \times 10^{-6}$

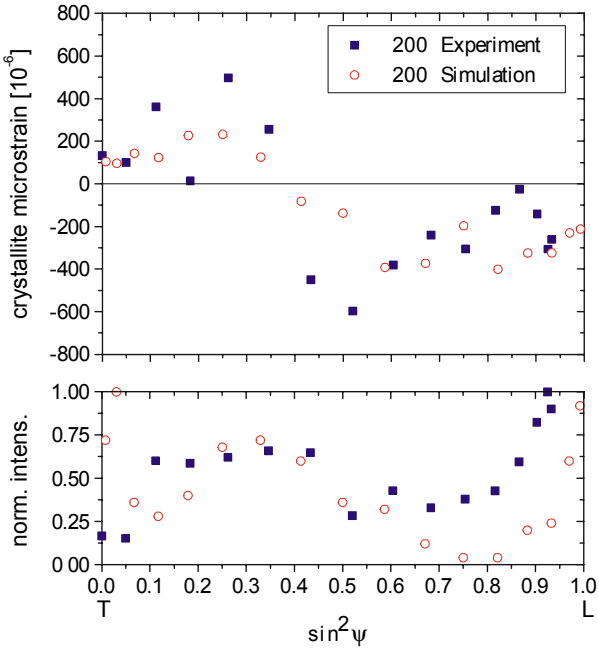

Figure 5.14: Crystallite microstrains and intensity distribution, AlMg3 sample, tensile deformation $\varphi_v = 0.24$, 200 reflection, T and L indicate transverse and load direction respectively, experimental uncertainty: $\pm 150 \times 10^{-6}$

The crystallite microstrains observed on the 220 reflection (figure 5.15) are among the lowest observed with a peak to valley value of 500×10^{-6}. The profile could be considered almost as linear within the experimental uncertainty of 150×10^{-6}.

The strength of the crystallite microstrains observed for the 311 reflection (figure 5.16) is about the same as for the 220 reflection. As opposed to the very good agreement between simulation and experiment for the 220 reflection, the simulations for the 311 reflection show large deviations from the experimental results in the intensity profiles. However, regarding the microstrain values, the simulated values agree well with the experimentally determined strain values.

Please refer to chapter 5.2.4 for a summary on the microstrains observed for the different deformation modes.

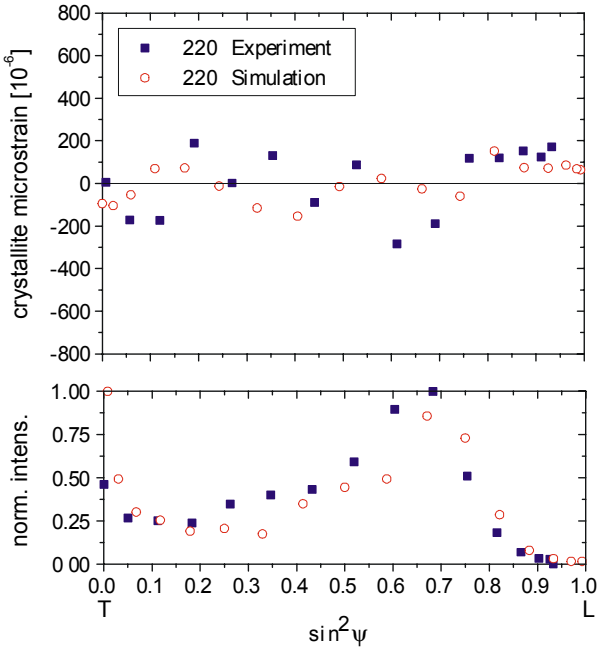

Figure 5.15: Crystallite microstrains and intensity distribution, AlMg3 sample, tensile deformation $\varphi_v = 0.24$, 220 reflection, T and L indicate transverse and load direction respectively, experimental uncertainty: $\pm 150 \times 10^{-6}$

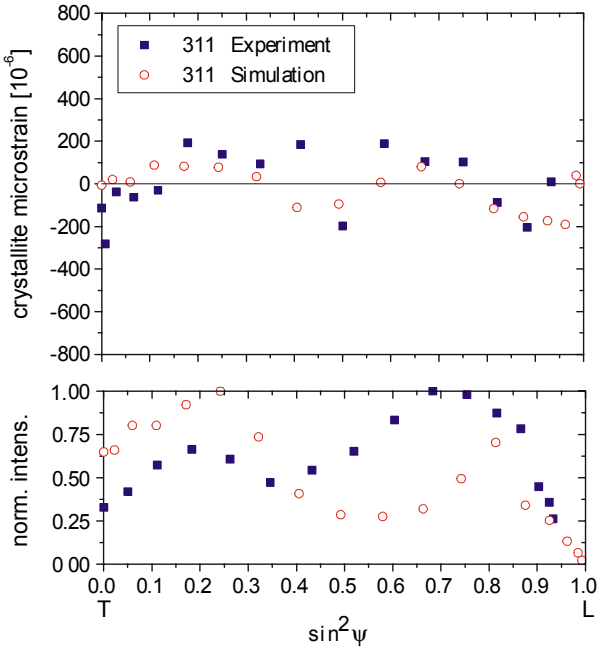

Figure 5.16: Crystallite microstrains and intensity distribution, AlMg3 sample, tensile deformation $\varphi_v = 0.24$, 311 reflection, T and L indicate transverse and load direction respectively, experimental uncertainty: $\pm 150 \times 10^{-6}$

5.2.2 Biaxial deformation

5.2.2.1 AlMg3

The results of the crystallite microstrain measurements on the tubular AlMg3 alloy torsion samples, using low energy synchrotron radiation (see chapter 4.2.1.2), are presented in the figures 5.17 to 5.20. The data is plotted for the axial sample direction (i.e. S2 in sample coordinate system) in form of ε vs. $\sin^2\psi$ and intensity vs. $\sin^2\psi$ graphs. The "ψ" in the plots must not be confused with the ψ as defined in the sample coordinate system (see chapter 4.2.2.2). The tangential and the axial reference direction are marked as T and A on the abscissæ respectively. Note that, due to to experimental constraints, the data for the deformation $\gamma = 0.15$ refers to the positive "ψ" branch while the higher deformations are related to the negative "ψ" branch. For each deformation step a different ex-situ deformed sample was

investigated, except the sample with the lowest deformation of $\gamma = 0.15$, which was measured before and after deformation. The other samples were deformed to $\gamma = 0.30$ and 0.40. Above that deformation, bulging occurred.

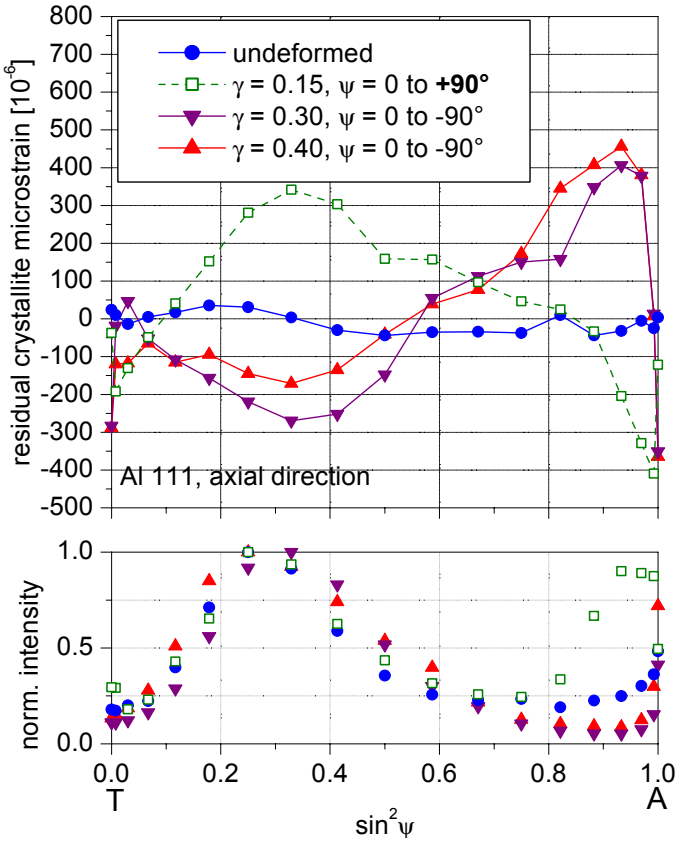

Figure 5.17: Crystallite microstrains measured on the Al 111 reflection in tubular AlMg3 torsion samples in different deformations. Note the different ψ range of 0° to +90° for the deformation $\gamma = 0.15$. Average error: $\pm 15 \times 10^{-6}$.

From the measurements on the undeformed sample it was concluded that the samples were basically stress-free prior to deformation. The complete data set from this sample was used to calculate the stress-free lattice parameter, which, for AlMg3, was found to be $d_0^{AlMg3} = 4.0607 \pm 5 \times 10^{-5}$ Å.

For all the investigated reflections, Al 111, 200, 220, and 311, it can be observed that the peak to valley value of the microstrain oscillations decrease slightly with increasing deformation ($\gamma = 0.30$ and 0.40). An overview of the maximum peak to valley values together with the hkl and its respective multiplicity, J, is given in table 5.1. It shows that there is a slight correlation between high multiplicity and low crystallite microstrains. But the crystal direction with the lowest multiplicity J = 8 does

not show the highest crystallite microstrains. The maximum, being 1100x10^{-6}, is observed on the Al 200 reflection (J = 12).

Table 5.1: Overview of the investigated reflections hkl, their respective multiplicity J and the maximum observed peak to valley values $\Delta\varepsilon$ for the residual crystallite microstrains

hkl	J	$\Delta\varepsilon$ [10^{-6}]
111	8	800
200	12	1100
220	12	1000
311	24	600

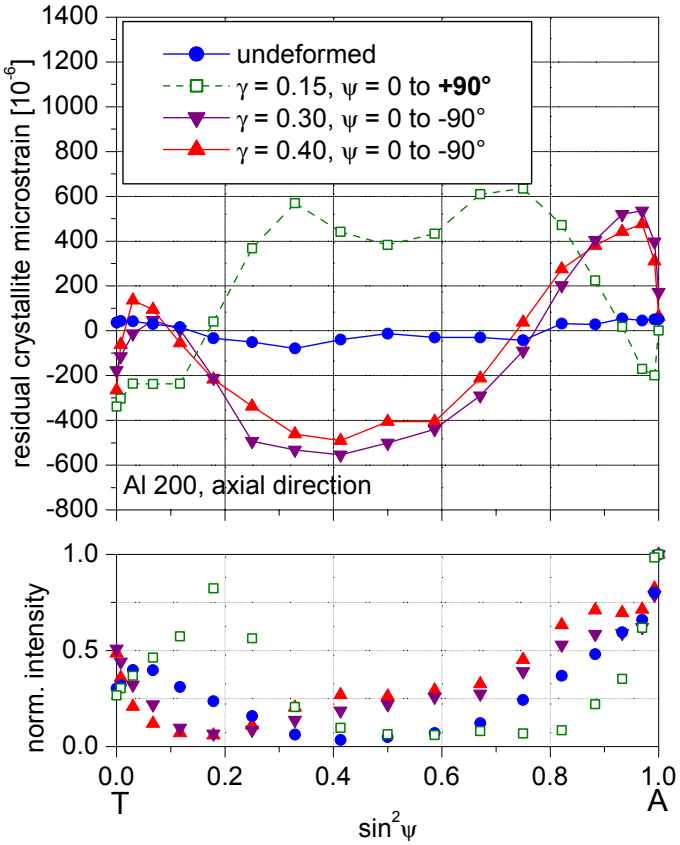

Figure 5.18: Crystallite microstrains measured on the Al 200 reflection in tubular AlMg3 torsion samples in different deformations. Note the different ψ range of 0° to +90° for the deformation γ = 0.15. Average error: ±20x10^{-6}.

Previous texture measurements on the rods the samples were made from, revealed a 111 / 100 fibre texture. With increasing deformation, the Al 200 and 220

(figures 5.17 and 5.18) exhibit the strongest intensity variations. The intensity profiles of the Al 311 reflection (see figure 5.20) show that the texture is not very pronounced for this crystallite direction.

The overall shape of all the microstrain profiles, for $\gamma = 0.30$ and 0.40, does not change strongly. The large differences in comparison to the curves for $\gamma = 0.15$ are of course firstly due to the different "ψ" ranges. Independently of the texture and apart of the different deformation, this leads to the so-called "ψ-splitting", manifesting itself in the opposed slopes of the curves. This occurs when a shear stress component is present. This is the case here since the principal axes of the residual stress state are oriented at 45° to the axial direction, which is the reference direction for the present plots.

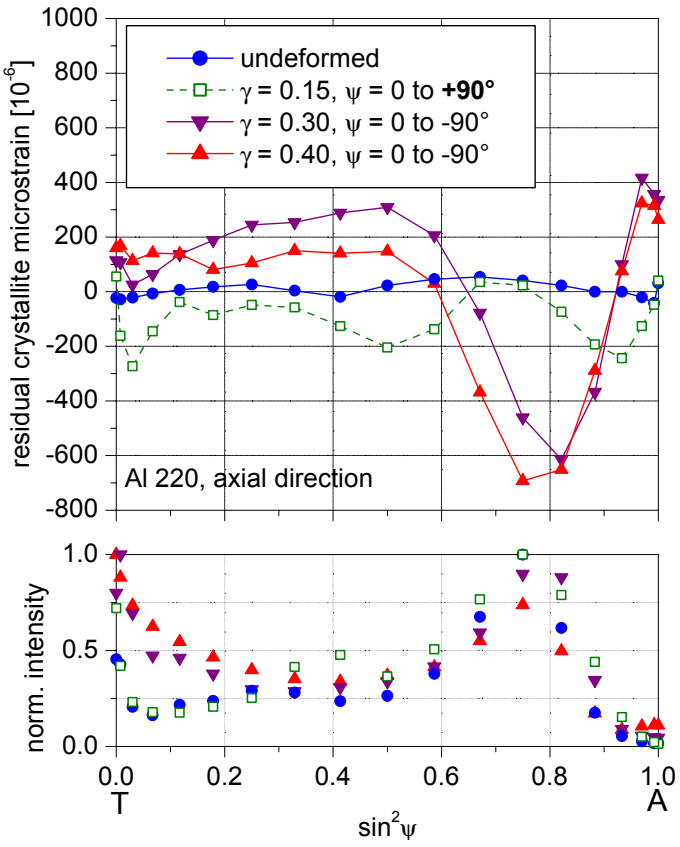

Figure 5.19: Crystallite microstrains measured on the Al 220 reflection in tubular AlMg3 torsion samples in different deformations. Note the different ψ range of 0° to +90° for the deformation $\gamma = 0.15$. Average error: $\pm 25 \times 10^{-6}$.

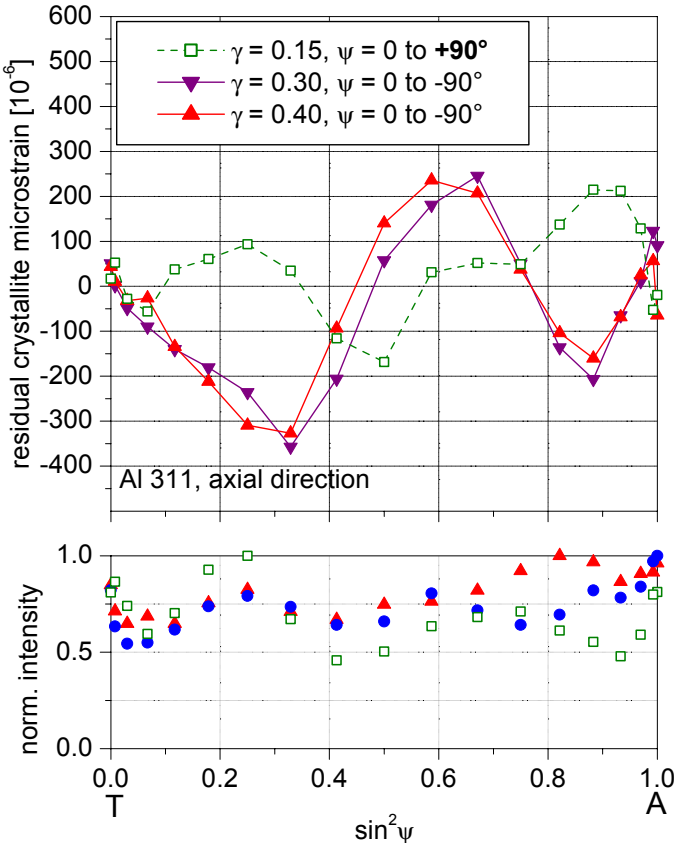

Figure 5.20: Crystallite microstrains measured on the Al 311 reflection in tubular AlMg3 torsion samples in different deformations. Note the different ψ range of 0° to +90° for the deformation γ = 0.15. Average error: ±20x10^{-6}.

Another reason for the differences is the dyadic symmetry of the expected torsion texture, which is clearly visible in the intensity profiles of the Al 200 reflection (figure 5.18): The intensity peak / minimum, situated at $\sin^2\psi \approx 0.5$, corresponds well with the texture measurements on solid torsion samples (see chapter 5.2.3.2, figure 5.33) and similar findings by Montheillet *et al.* [Mon 1984] and Canova *et al.* [Can 1984]. Another typical feature of pure torsion textures of Al can be seen in the Al 111 intensity profile for γ = 0.15 (see figure 5.17). The pole, situated before in axial direction for the undeformed sample, is slightly rotated by about 10° in the sense opposed to the shear, i.e. ccw. This intensity peak corresponds to ideal orientation A as shown in figure 2.4. Montheillet *et. al.* [Mon 1984] reported that this rotation did not exceed 10° in their experimental observations on the surface of solid samples in fixed end torsion.

Please refer to chapter 5.2.4 for a summary of the microstrains observed for the different deformation modes.

5.2.2.2 AlSi25Cu4Mg1

The investigated tubular torsion sample made of the AlSi25Cu4Mg1 alloy was ex-situ deformed to $\gamma = 0.15$. This deformation is close to the maximum achievable for this type of sample geometry. The hkl specific 2θ shifts, measured at different sample positions, permitted the determination of the residual shear stresses, assuming the absence of stresses in radial (S3) direction. This was done by a linear fit of equation 2.34 (see chapter 2.4.2), similar to the so-called $\sin^2\psi$ method and by using XECs according to the Kröner model. The results are listed in table 5.2.

Table 5.2: Residual stresses as obtained from a linear fit to the observed ring distortions and using XECs according to the Kröner model

hkl	residual stress [MPa]	error [MPa]
Al 111	-47	±4
Al 200	-52	±8
Al 220	-48	±5
Al 311	-41	±7
Si 111	68	±7
Si 311	62	±12

The residual shear stresses in the Al phase have the same sign as the previously applied deformation shear while the signs of the stresses in the Si phase are opposed to it. Taking into account the multiplicity, J, of the investigated reflections and the volume fractions of the two phases of 62.5vol.% Al and 37.5vol.% Si the macro residual shear stress calculated to be -5±8MPa and can be considered as approximately zero within the experimental uncertainty. Note that the macrostress does not necessarily need to be zero since only one wall of the tube was measured.
The deviations of the measured peak positions from the linear fit were all within the experimental uncertainty of about 50×10^{-6}. Therefore, it was concluded that no significant crystallite microstrains are present in this sample

5.2.3 Triaxial deformation

5.2.3.1 Macrostrain tensors and intergranular strains

AlMg3

The solid torsion sample made of AlMg3 was subsequently deformed to $\gamma = 1.5$, 2.5, and 3.5. The measurements were carried out after deformation, except after the highest deformation $\gamma = 3.5$, where the measurements were made under load, i.e. in-situ. The relaxation caused a decrease of the load torque of about 7% during these in-situ measurements, and was judged to be insignificant. For this experiment, the setup with the conical slit system was used (see chapter 4.2.1.2)

Macrostrain and macrostress tensors

Figure 5.21 shows the radially and deformation dependent macrostrain tensors as calculated from the hkl specific pseudo macrostrains (see equation 2.33). The corresponding macrostress tensors, calculated using XECs according to the Kröner model and assuming quasi-isotropy, are presented in figure 5.22. The assumption of quasi-isotropy is justified by the fact that Al can be considered as almost elastically isotropic with an anisotropy factor of z = 1.6. Due to a small sample misalignment, the plots show no data at the center position. Since the employed technique only allows bulk measurements, no data points in the surface region of the sample (i.e. r = 2.5mm) are available either.

Looking first at the macrostrain tensors for $\gamma = 1.5$ and 2.5 (i.e. the residual macrostrain), the following observations can be made: The $\varepsilon 12$ component (direction of the previously applied load) exhibits a maximum of -1400×10^{-6} close to the center, which has the same sign as the previously applied deformation load. Similar findings were already published by Martins *et al.* [Mart 1999, and 2000]. Ideally, the value of the strain is zero at the center since the torsion sample center undergoes theoretically no shear deformation, which is comparable to the neutral fibre in bending tests. The residual macro shear strain decreases linearly towards the surface and reaches slightly positive values. The $\varepsilon 12$ component is not significantly dependent on the degree of deformation (see the following chapter).

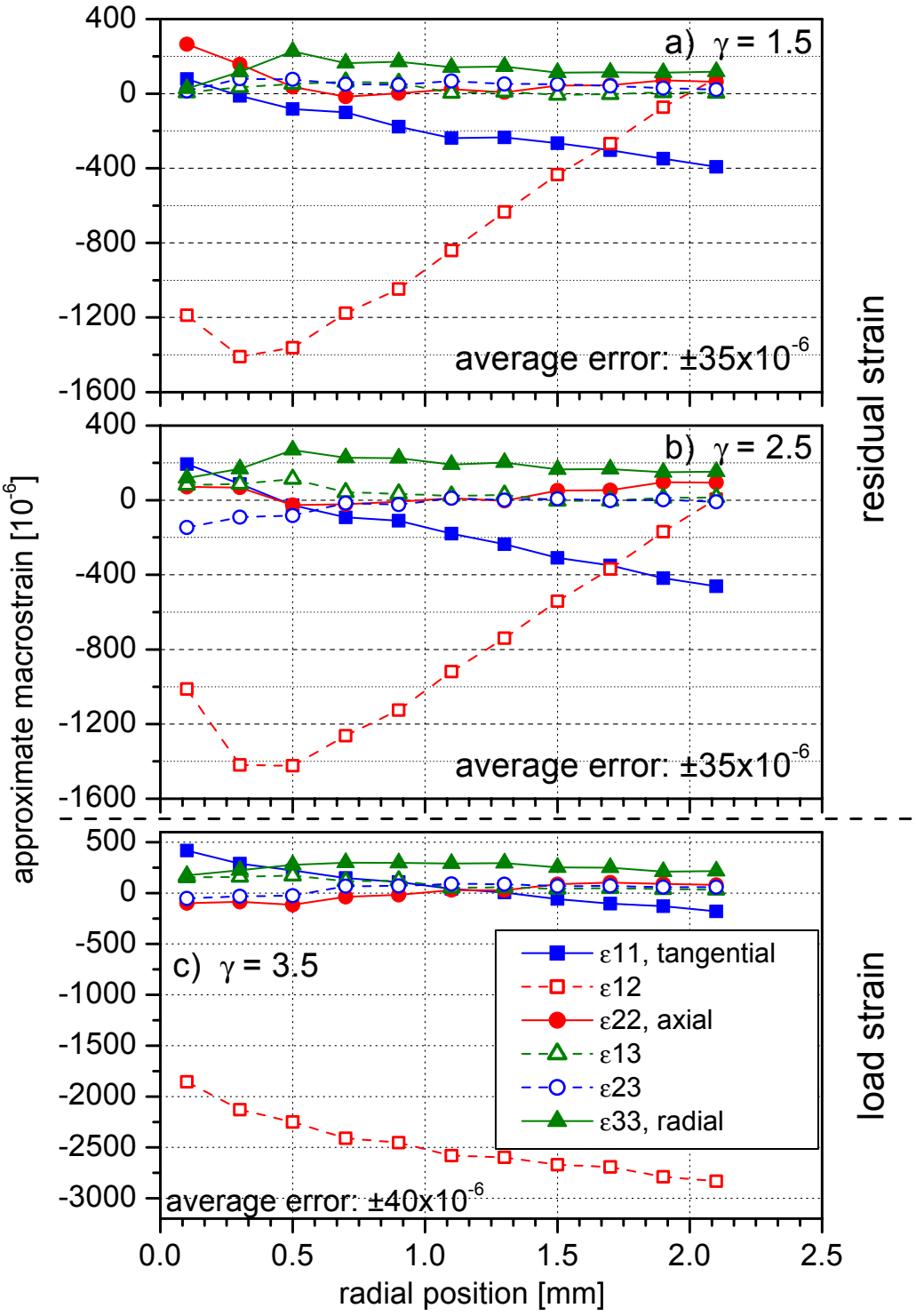

Figure 5.21: Radially dependent approximate macrostrain tensor within a solid AlMg3 torsion sample, subsequently deformed to a) $\gamma = 1.5$ (residual strain), b) $\gamma = 2.5$ (residual strain), and c) $\gamma = 3.5$ (load strain tensor).

The main changes due to the change of the deformation take place in the diagonal elements of the tensors.

At $\gamma = 1.5$, the almost linear decrease of the tangential component $\varepsilon 11$ has a gradient of about -250×10^{-6} / mm (decrease from 100×10^{-6} at r = 0.1mm to -400×10^{-6} at r = 2.1mm). At $\gamma = 2.5$, the gradient has increased by about 40% to -350×10^{-6} / mm (decrease from 200×10^{-6} at r = 0.1mm to -500×10^{-6} at r = 2.1mm).

The $\varepsilon 22$ (axial) tensor component exhibits, for $\gamma = 1.5$, a tensile strain of 250×10^{-6} at r = 0.1mm, decreases to around zero in the mid--radius range, and gains again slightly tensile values (70×10^{-6}) around r = 2mm. In principle, the overall profile is the same for $\gamma = 2.5$, but the tensile strain close to the center has decreased by 60% to about 100×10^{-6}, while it has increased to 100×10^{-6} at r = 2mm.

The $\varepsilon 33$ (radial) tensor component remains almost constant over the investigated cross section with a tensile strain of about 150×10^{-6} for $\gamma = 1.5$ and 200×10^{-6} for $\gamma = 2.5$. Close to the center it decreases close to zero ($\gamma = 1.5$) and 100×10^{-6} ($\gamma = 2.5$). Ideally, the $\varepsilon 11$ and $\varepsilon 22$ components are identical at r = 0mm.

In comparison to the deformation steps of $\gamma = 1.5$ and 2.5, the strain measurements at $\gamma = 3.5$ were carried out under the external deformation load, i.e. in-situ. The $\varepsilon 11$ component shows in these measurements a slightly smaller gradient of 300×10^{-6} / mm but a higher tensile strain close to the center (400×10^{-6}). The radial component, $\varepsilon 33$, exhibits values between 200 and 300×10^{-6}. While these two components do not change their overall shape, as compared to the lower deformations, this is not the case for $\varepsilon 12$ and $\varepsilon 22$.

The shear tensor component shows, as expected, an almost constant large compressive load strain (-2800×10^{-6}) with a decrease close to the center. Remembering that this component has the opposed sign when crossing the center (rotational symmetry of the coordinate system, causing a singularity for this component in the center), this observed decrease is mainly caused by the spatial resolution of the measurement technique (see chapter 4.2.3.2).

Contrary to the case for the lower deformations, the axial component $\varepsilon 22$ is now compressive (-100×10^{-6}) close to the center. Close to the surface the strain is slightly tensile (50×10^{-6}).

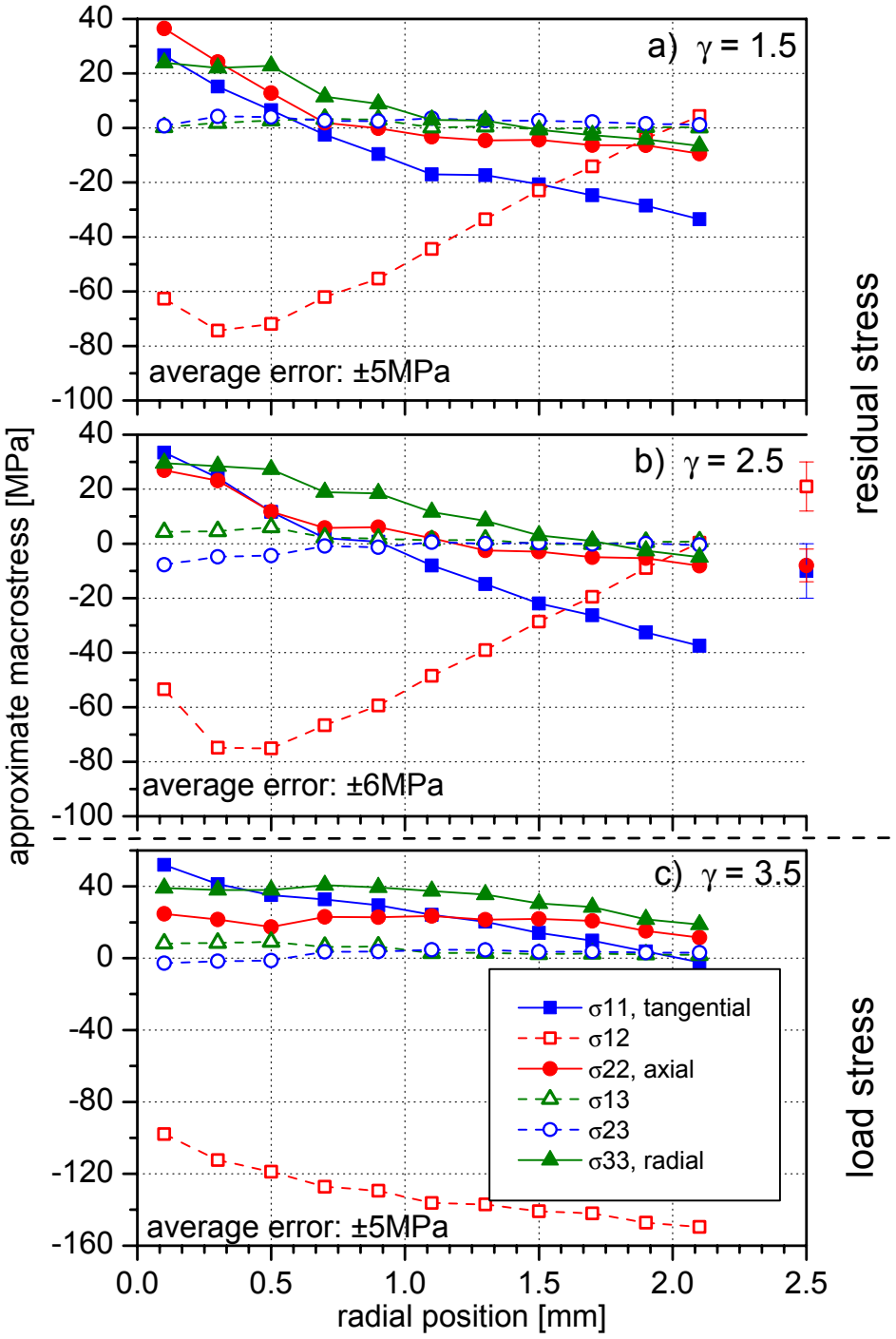

Figure 5.22: Radially dependent approximate macrostress tensor within a solid AlMg3 torsion sample, subsequently deformed to a) $\gamma = 1.5$ (residual stress), b) $\gamma = 2.5$ (residual stress), and c) $\gamma = 3.5$ (load stress tensor). The separate data points in b), at r = 2.5, are from d vs. $\sin^2\psi$ measurements at the sample surface of a similarly deformed sample in the respective directions using conventional x-rays.

Looking now at the calculated macrostress tensors (see figure 5.22), all the diagonal components of the macrostress tensor decrease from large tensile stresses, close to the center, to compressive (for γ = 1.5 and 2.5) or lower tensile stresses (for γ = 3.5). The σ12 shear component shows large compressive residual stresses close to the center and a trend towards tensile residual stresses at the close surface region. The load stress profile (γ = 3.5) decreases from a maximum of about -150MPa, close to the surface, to about –100MPa close to the center. This decrease can be explained in the same way as the respective macrostrain component above. The components σ13 and σ23 can be considered as equal zero within the experimental uncertainty. In fact, if these components were not zero they would violate the uniqueness of the stress / strain relationship (see chapter 4.2.5.3).

For the determination of the macrostrain and macrostress tensors the accuracies of the stress-free Al calibration powder used for the detector distortion correction and of the measured stress-free lattice parameter of AlMg3 (see chapter 5.2.2.1) proved to be not satisfying for the complete evaluation. The use of d_0^{Al} = 4.0496±5x10^{-5}Å and d_0^{AlMg3} = 4.0607±5x10^{-5}Å lead to the conclusion that an apparent "hydrostatic stress" of about -20MPa was present in the sample. This stress only affects the diagonal components of the deviatoric stress tensor and is most probably due to the uncertainty in the stress-free lattice parameters. The accurate determination of the hydrostatic part of the stress tensor requires a higher accuracy for the measurement of the stress-free lattice parameters [Hau 1997]. For the plots in the figures 5.21 and 5.22, therefore, the decision was taken to derive the deviatoric part of the stress / strain tensor from the equilibrium condition. Due to the rotational symmetry of the stress state only the σ22 (axial) component is not self-compensating (i.e. with respect to the laboratory system, all tensor components change sign, except the axial one, when crossing the sample center). For the calculation of the equilibrium forces, additional surface measurements on a similarly deformed sample using a laboratory x-ray source were taken into account. The data points are shown at r = 2.5 for γ = 2.5, in figure 5.22. The calculation of the axial forces lead to the above mentioned estimation of the apparent "hydrostatic" stress of –20MPa. The σ12 value (independent of hydrostatic part) from the surface is in very good agreement with the (expected) trend of the σ12 component of the synchrotron measurements. The "good" agreement between the trend of the σ22 value from the bulk measurements

and the $\sigma 22$ from the surface measurements is inherent to the above-discussed procedure (see chapter 5.2.3.5 for a closer discussion of the axial component). For the tangential component, $\sigma 11$, it can be concluded from the surface measurements that it should exhibit a steep gradient in the close surface region.

Assuming that the load shear stress is constant over the whole radial range and equals -150MPa (maximum value of $\sigma 12$ for $\gamma = 3.5$), the applied load torque can be calculated using equation 2.32. The calculated torque is 4.9Nm, about 17% lower than the torque measured independently with a strain gauge on the torsion device. A calculation with the equivalent von Mises stress, in order to take account of the triaxial stress state, yielded about the same result. In fact, similar observations on steel torsion samples were reported by Bollenrath *et al.* [Bol 1967] and Prümmer *et al.* [Prü 1966]. This indicates that XECs obtained from tensile experiments, or calculated with the according models, are not directly applicable for multiaxial deformations. Nevertheless, in the present case, this deviation plays a minor role since only stresses calculated for the same deformation mode are compared to each other. Another reason for these deviations, though maybe not the major one, might be the fact that XECs calculated from the single crystal elastic constants of pure Al were used. Dawson *et al.* [Daw 2001] concluded from a parametric study that the single crystal elastic constants of pure Al cannot be directly applied when calculations for Al alloys are made. However, a closer investigation of these two aspects is beyond the scope of this work.

Intergranular strains

The three tensor components that exhibit the largest intergranular strains are shown in figures 5.23 to 5.25. They display the radially and deformation dependent intergranular strains for the reflections Al 220, 222, 331, and 422 for the $\varepsilon 11$, $\varepsilon 12$, and $\varepsilon 22$ component. The respective macrostrain tensor component is plotted additionally as a reminder since the intergranular strains are defined as the hkl specific deviation from the respective macrostrain component (see chapter 2.3.2), i.e. the macrostrain components are identical to the corresponding ones in figure 5.21.

The $\varepsilon 11$ (tangential) component shows a clear separation for all three deformations (see figure 5.23): The 331 and 422 reflection exhibit slightly tensile or zero intergranular strains. The 220 and 222 show mainly compressive intergranular strains up to -200×10^{-6}. The intergranular strains observed for the 220 lattice plane are not

only the strongest but they also show large oscillations which extend into the tensile strain close to the sample center. The general trend of all tangential intergranular strain components is their decrease with increasing deformation.

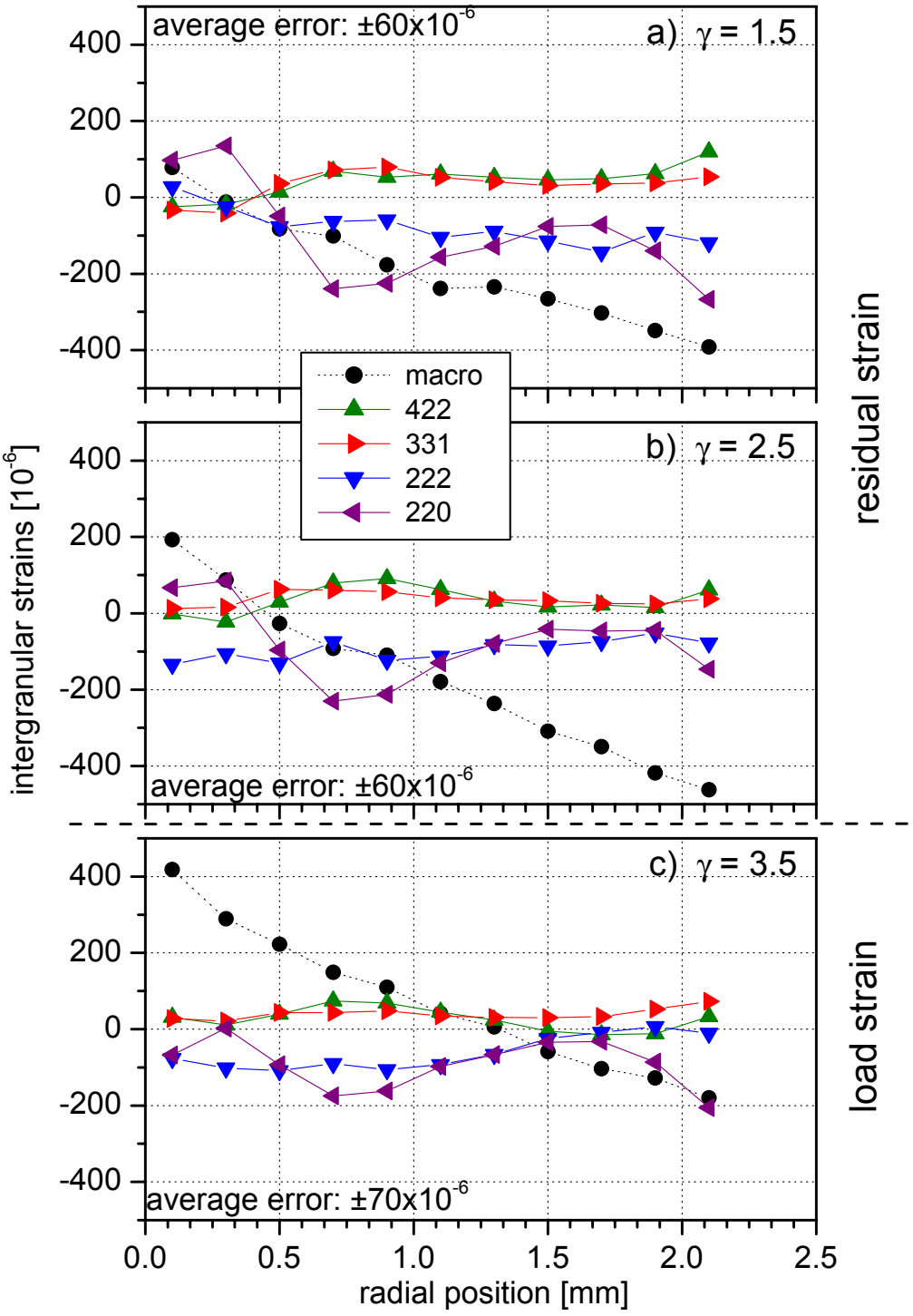

Figure 5.23: Radially dependent intergranular strains in the tangential direction within solid AlMg3 torsion sample, subsequently deformed to a) $\gamma = 1.5$ (residual strain), b) $\gamma = 2.5$ (residual strain), and c) $\gamma = 3.5$ (load strain).

For the $\varepsilon 12$ component (see figure 5.24) the intergranular strains observed on the 331 reflection are almost zero at all radii and deformations. This reflection well represents, therefore, the macrostrain. As already observed for the $\varepsilon 11$ component, the intergranular strains for the 422 reflection are, in general, tensile (up to 100×10^{-6}) or zero, with one exception close to the center for $\gamma = 2.5$, where the strains are compressive. The intergranular strains for the 220 and 222 reflections are mostly compressive, except in the center region, where for the 220 reflection large tensile strains (up to 200×10^{-6}) can be observed. Contrary to the 331 and 422 reflection, which exhibit only a weak dependence on the degree of deformation, the intergranular strains first increase with increasing strain (step from $\gamma = 1.5$ to 2.5). However, after the deformation to $\gamma = 3.5$ they have slightly decreased again, continuing the overall trend seen for the deformation $\gamma = 2.5$.

The strongest intergranular strains were observed for the $\varepsilon 22$ (axial) component (see figure 5.25). Here, the 220 reflection exhibits large tensile intergranular strains (up to 350×10^{-6} with a steep decrease to compressive values close to the center) while the 331 and 422 reflections only show strains close to zero or slightly compressive ones (-100×10^{-6}). The strains observed on the 222 reflection show a general trend to increase with increasing deformation. They develop from almost zero strain at all radii at $\gamma = 1.5$ to mostly tensile strains at $\gamma = 3.5$.

For all presented tensor components the 331 reflection is, in general, the least affected by intergranular strains and closely represents, therefore, the macrostrain state. The 220 reflection shows, typically, the largest intergranular strains and the strongest dependence on the degree of deformation. This is contrary to observations on a solid torsion sample made of AlSi25Cu4Mg1 (see following chapter) and to results reported by Pang *et al.* on Al7050 tensile samples [Pan 1998a]. Furthermore, the similarity between respective intergranular strain components of a specific hkl is remarkable.

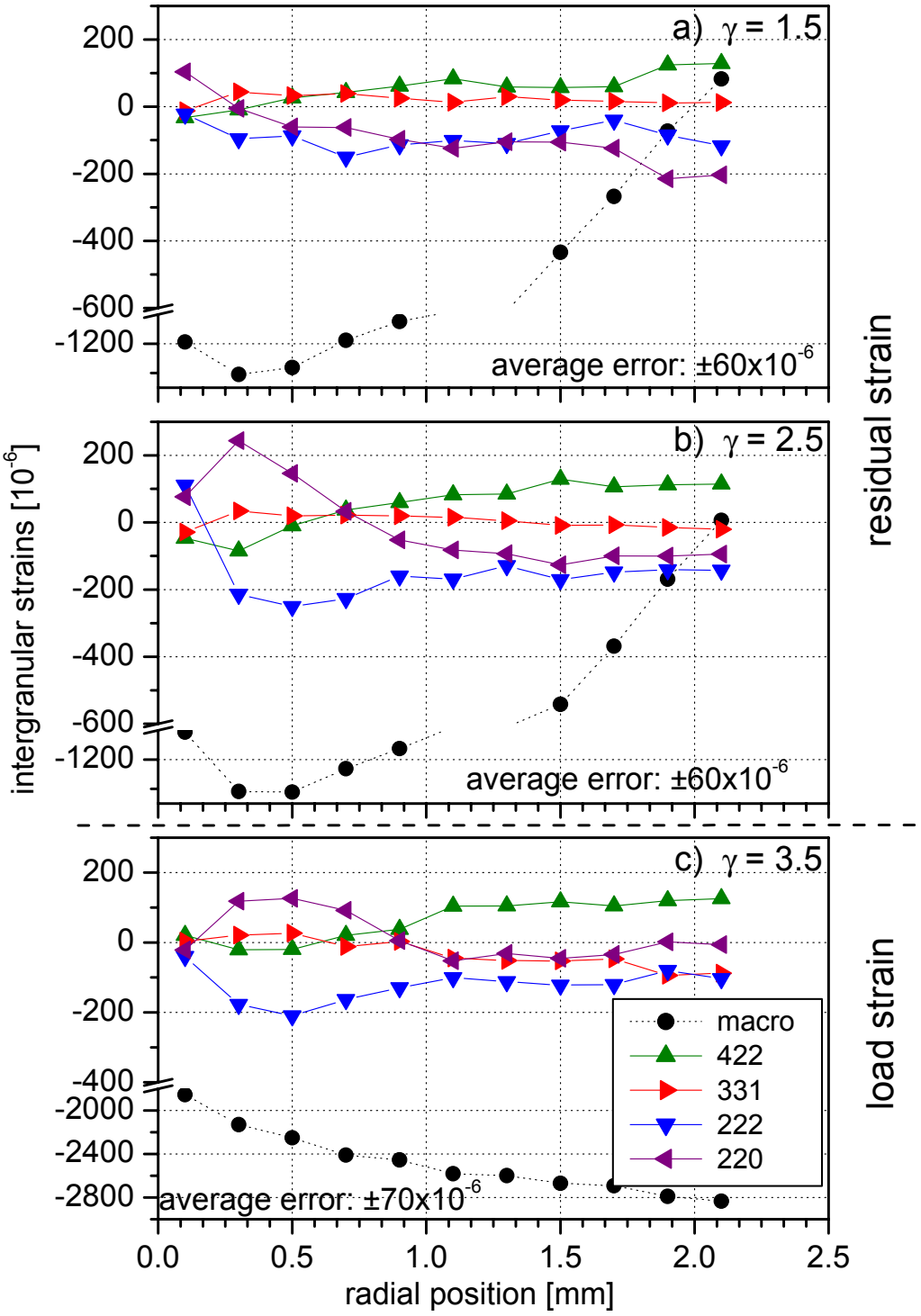

Figure 5.24: Radially dependent intergranular strains in the (previous) load shear direction within a solid AlMg3 torsion sample, subsequently deformed to a) $\gamma = 1.5$ (residual strain), b) $\gamma = 2.5$ (residual strain), and c) $\gamma = 3.5$ (load strain).

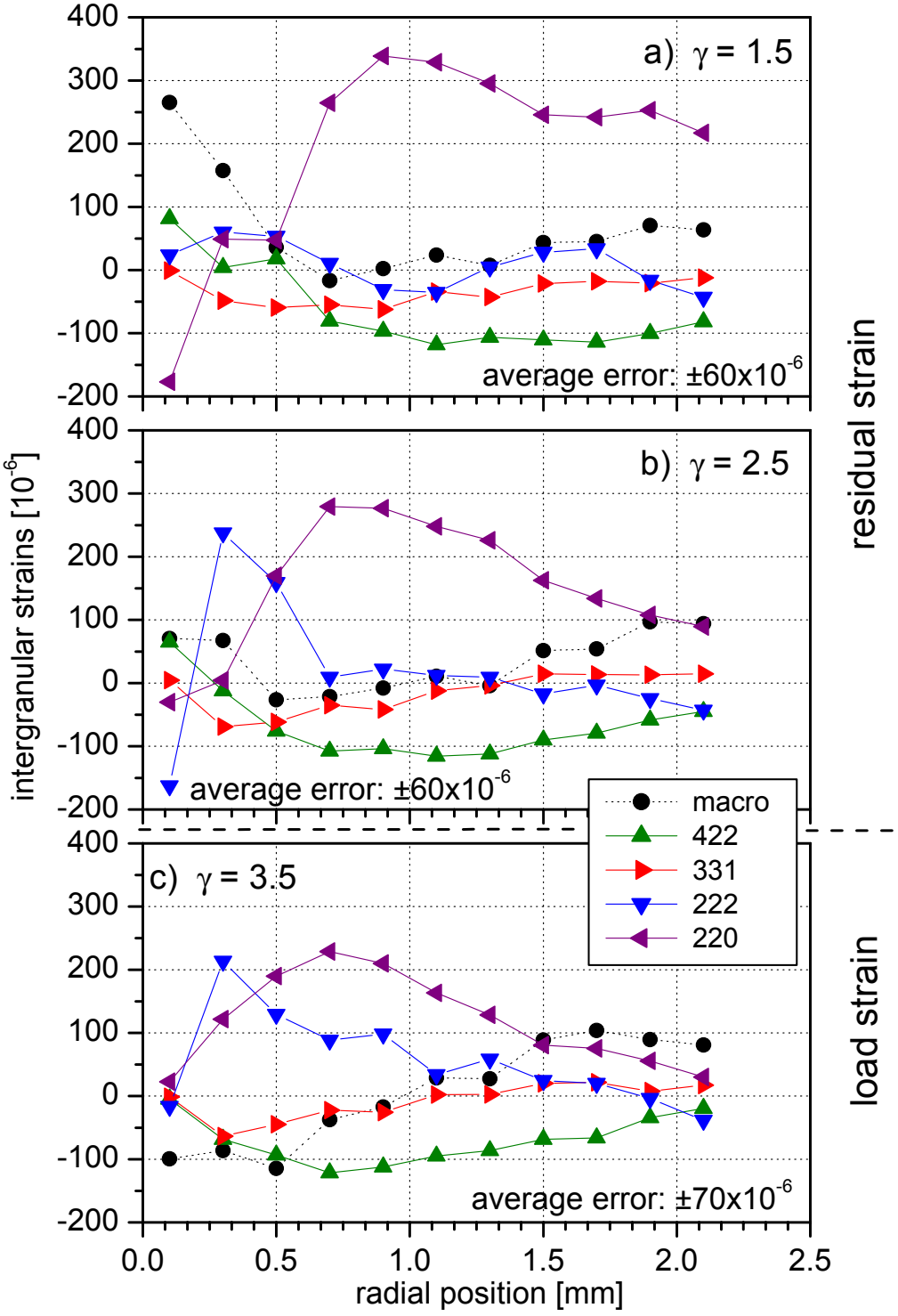

Figure 5.25: Radially dependent intergranular strains in the axial direction within a solid AlMg3 torsion sample, subsequently deformed to a) $\gamma = 1.5$ (residual strain), b) $\gamma = 2.5$ (residual strain), and c) $\gamma = 3.5$ (load strain).

AlSi25Cu4Mg1

Residual macrostrains

Figures 5.26 and 5.27 show the radial dependence of the residual macrostrain tensor components for the deformation $\gamma = 0.15$ and $\gamma = 0.30$ respectively. The macrostrain was estimated by averaging the respective components of all measured hkl and phases, weighted by their lattice plane multiplicity and their phase volume fraction in the sample (see equation 2.33).

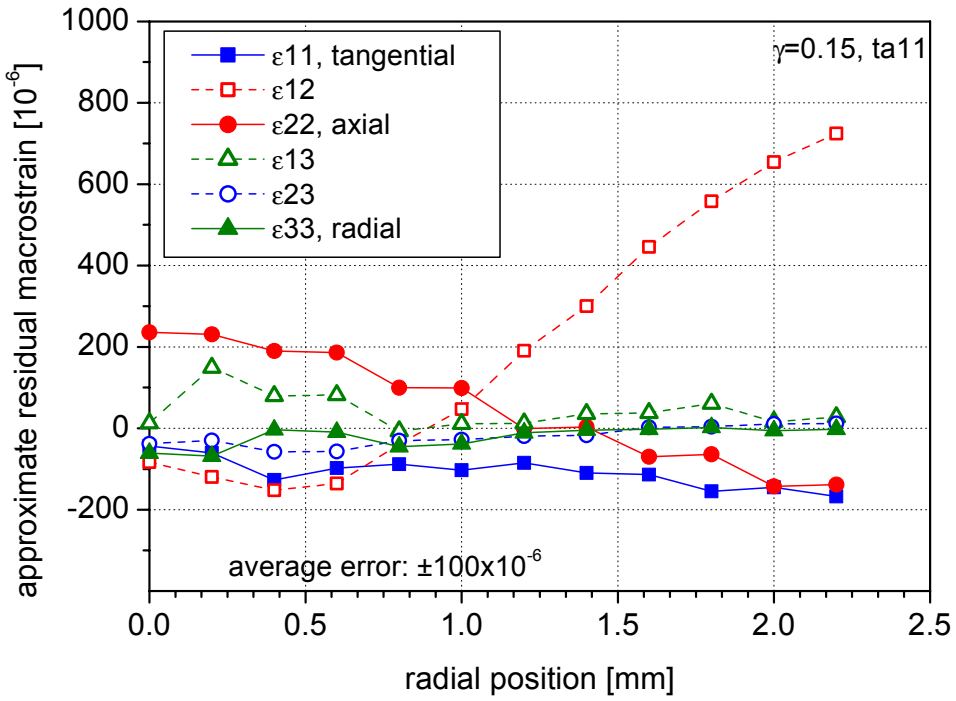

Figure 5.26: Radially dependent approximate residual macrostrain tensor within an AlSi25Cu4Mg1 torsion sample for a deformation of $\gamma = 0.15$. Average error: $\pm 1 \times 10^{-4}$

For both deformations the off diagonal εj3 components can be considered zero or close to zero within the experimental uncertainty. The tangential component (ε11) exhibits a small linear increase of compressive residual macrostrain towards the sample surface with a maximum of -180×10^{-6} for $\gamma = 0.15$ and -300×10^{-6} for $\gamma = 0.30$. The ε12 component, lying in direction of the previously applied load stress, changes in both figures from compressive strain close to the sample center to large tensile strain (750×10^{-6}) close to the surface, thus having the opposite sign of the previous load. The change of sign has been observed in other experiments on torsion samples

made of steel [Bol 1967]. Only the ε22 component (axial direction) is strongly affected by the higher deformation. The axial strain decreases almost linearly from tensile load at the center to compression close to the surface.

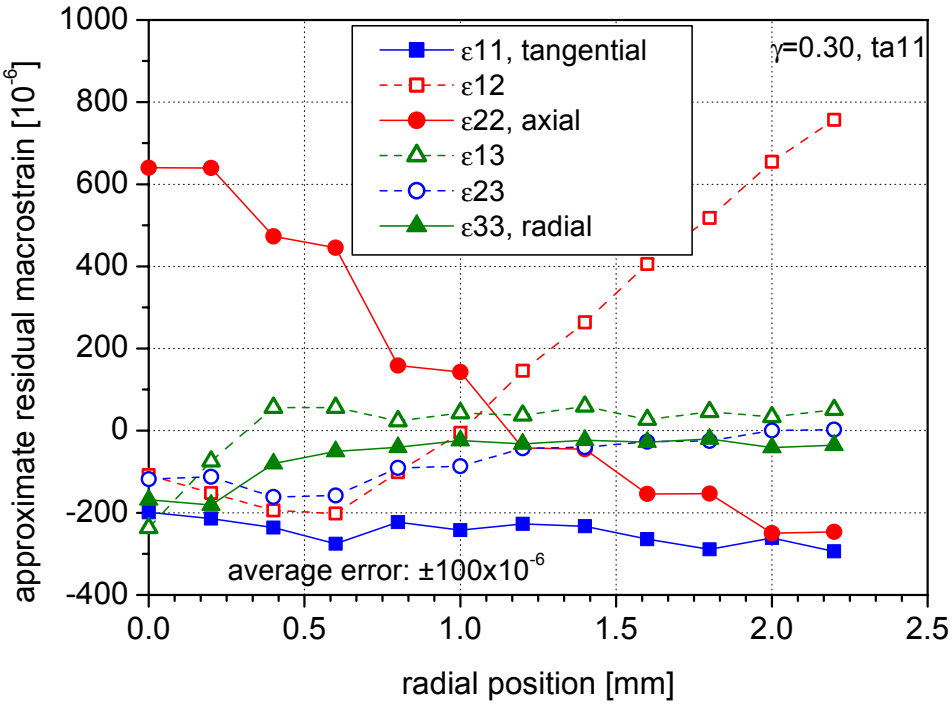

Figure 5.27: Radially dependent approximate residual macrostrain tensor within an AlSi25Cu4Mg1 torsion sample for a deformation of $\gamma = 0.30$. Average error: $\pm 1 \times 10^{-4}$

For $\gamma = 0.30$ the steepness of the slope is almost 2.5 times stronger than for $\gamma = 0.15$. The values for the strain at the center / close to the surface are 230×10^{-6} / -150×10^{-6} for $\gamma = 0.15$ and 630×10^{-6} / -230×10^{-6} for $\gamma = 0.30$. The increase of axial strain can be explained by the advanced evolution of a torsion texture (see chapter 5.2.3.5). The radial dependent residual macrostress tensor for $\gamma = 0.30$, presented in figure 5.28, has been calculated from the macrostrains using XECs according to the Kröner model, assuming quasi-isotropy. Additional measurements on the surface using a laboratory x-ray source are plotted at r = 2.5mm. In contrast to the procedure for the solid torsion sample made of AlMg3 the diagonal components were plotted without correction for the hydrostatic stress. Considering the axial stress component the equilibrium condition is obviously violated, but subtracting the supposedly hydrostatic stress of about –35MPa would yield a satisfying result. Moreover, as in the case for

AlMg3, the axial stress observed at the surface would coincide well with the trend given by the calculated bulk axial stress. Though the data points are critical close to the center, the strain / stress uniqueness condition for σ13 and σ23 can be considered fulfilled within the experimental uncertainty.

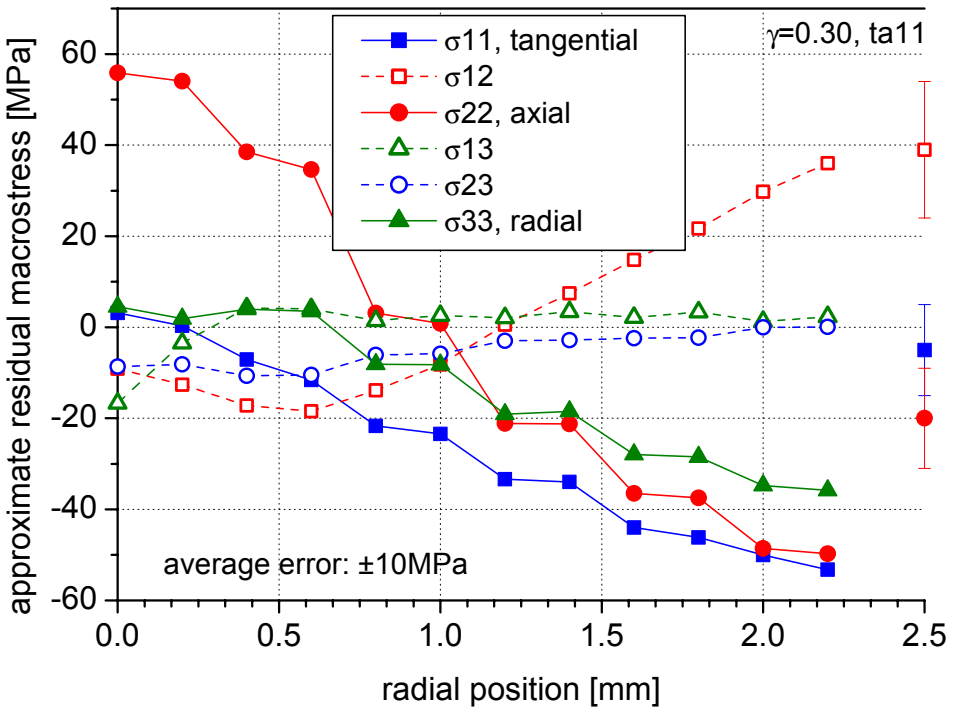

Figure 5.28: Radially dependent residual macrostress tensor within an AlSi25Cu4Mg1 torsion sample for a deformation of $\gamma = 0.30$; average error: ±10MPa. The separate data points at r = 2.5 are from d vs. $\sin^2\psi$ measurements at the sample surface in the respective directions using conventional x-rays.

Residual intergranular strains

The residual intergranular strains observed on the different hkl and phases (see chapter 2.4.2) are given in figures 5.29 to 5.31. The dotted lines represent the selected macrostrain components and the solid lines the intergranular strain component for the different phases / hkl. Only very low intergranular strains were observed for the εj3 components and, therefore, are not plotted. The profiles of the intergranular strain component ε11 for the two deformations are shown in figures 5.29a and b. The main changes take place in the Al 111, Al 200, and Si 311 orientations. For the Al 200 direction the tangential intergranular strain (ε11) decreases almost to zero at $\gamma = 0.30$ while for $\gamma = 0.15$ it was showing significant

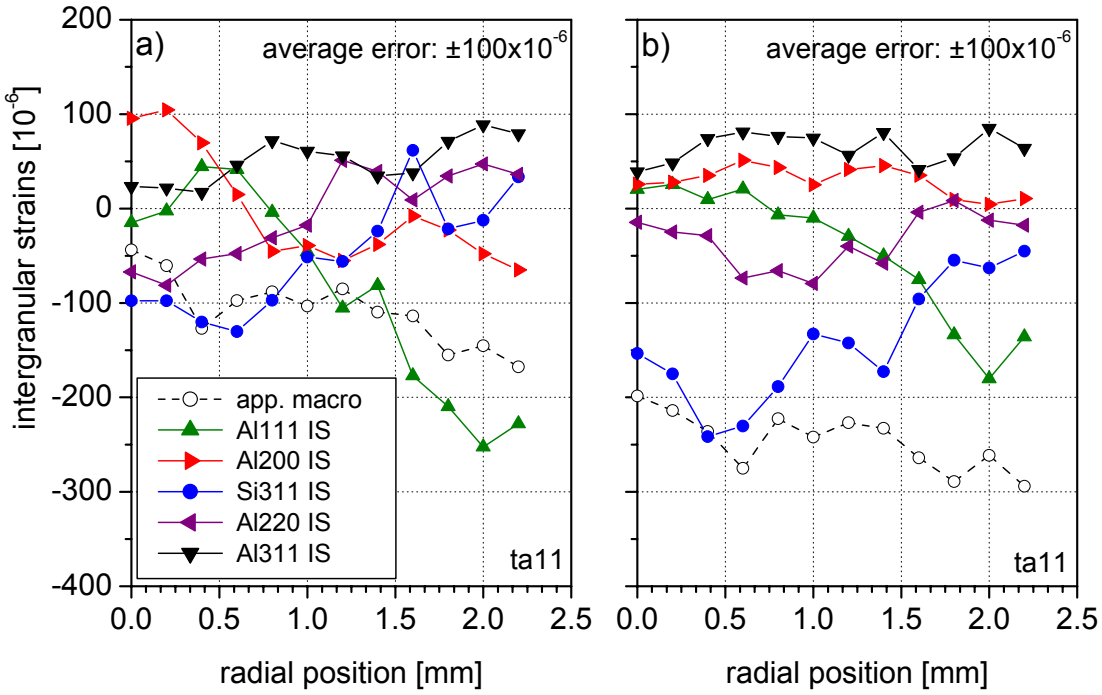

Figure 5.29: Radially dependent ε11 (tangential) component of the residual intergranular strain within an AlSi25Cu4Mg1 torsion sample for a deformation of $\gamma = 0.15$ (a) and $\gamma = 0.30$ (b), respectively; dotted line: respective component of the residual macrostrain tensor. Average error: $\pm 1 \times 10^{-4}$.

tensile strain at the center and compression close to the surface. The tangential intergranular strain for the Al 111 orientation shows the same tendency to decrease with higher deformation. In contrast to that, the ε11 component in Si 311 is compressive over the whole cross section for $\gamma = 0.3$ while it was only slightly compressive and tensile at $\gamma = 0.15$. From an incomplete data set for the Si 331 orientation, which is not presented here, it can be estimated that all the intergranular strains in Si 311 are similar to those in Si 331. For the tangential component, the general trend with higher deformation seems to be an increase of the compressive intergranular strain in the Si phase and a decrease of the intergranular strains in the Al phase. While the influence of the deformation on the tangential intergranular strain component (ε11) was already rather small, it is almost negligible for the ε12 component (i.e. in the direction of the previously applied deformation load), as already seen for the residual macrostrain. The figures 5.30a and b look almost identical, showing large compressive values for the Si 311 orientation close to the surface, which decay to -200×10^{-6} at the center. The strains in the Al phase are either

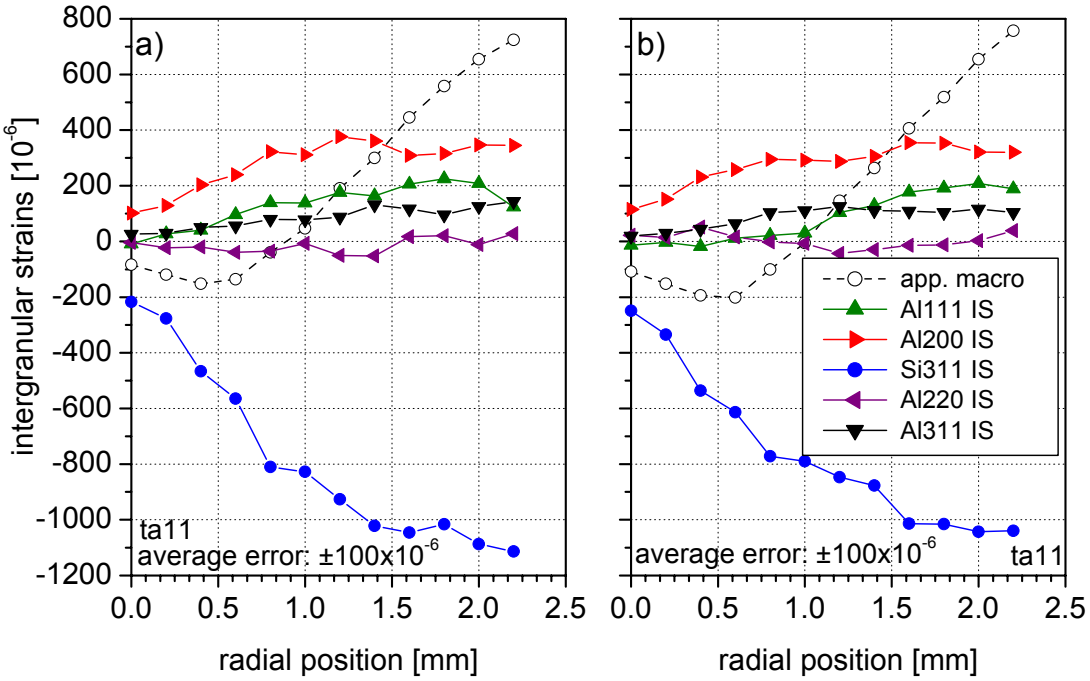

Figure 5.30: Radially dependent ε12 component (previous load shear direction) of the residual intergranular strain within solid AlSi25Cu4Mg1 torsion sample for a deformation of $\gamma = 0.15$ (a) and $\gamma = 0.30$ (b) respectively; dotted line: respective component of the residual macrostrain tensor. Average error: $\pm 1 \times 10^{-4}$.

very close to zero (Al 220) or slightly tensile (Al 200, max: 380×10^{-6}) with no strong dependence on the radial position. This means that the intergranular strain in the Si phase keeps the sign of the previously applied load strain while the intergranular strains in the Al phase tend to change sign.

For the axial component (ε22) the higher deformation seems to have a homogenizing effect (figures 5.31a, b). At $\gamma = 0.15$, there are still significant differences observable close to the center between the Al phase (tensile or almost zero for all hkl) and the Si 311, which is slightly compressive. At $\gamma = 0.30$, almost all the differences have vanished. The axial intergranular strains are almost zero over the whole cross section, which means that all hkl specific axial strains equal the axial macrostrain (dotted line).

Considering all intergranular strain components at the different deformations, the Al 220 direction seems to exhibit the lowest intergranular strains and therefore represents closely the macrostrain state. The same conclusion was drawn from the tensile experiments by Pang *et al.* [Pan 1998a] on Al7050 samples. The Si 311

lattices show the strongest residual intergranular strains of all the investigated reflections and tend in general to compressive intergranular strains. For the Al phase, the Al 200 is the most strongly affected by intergranular strains.

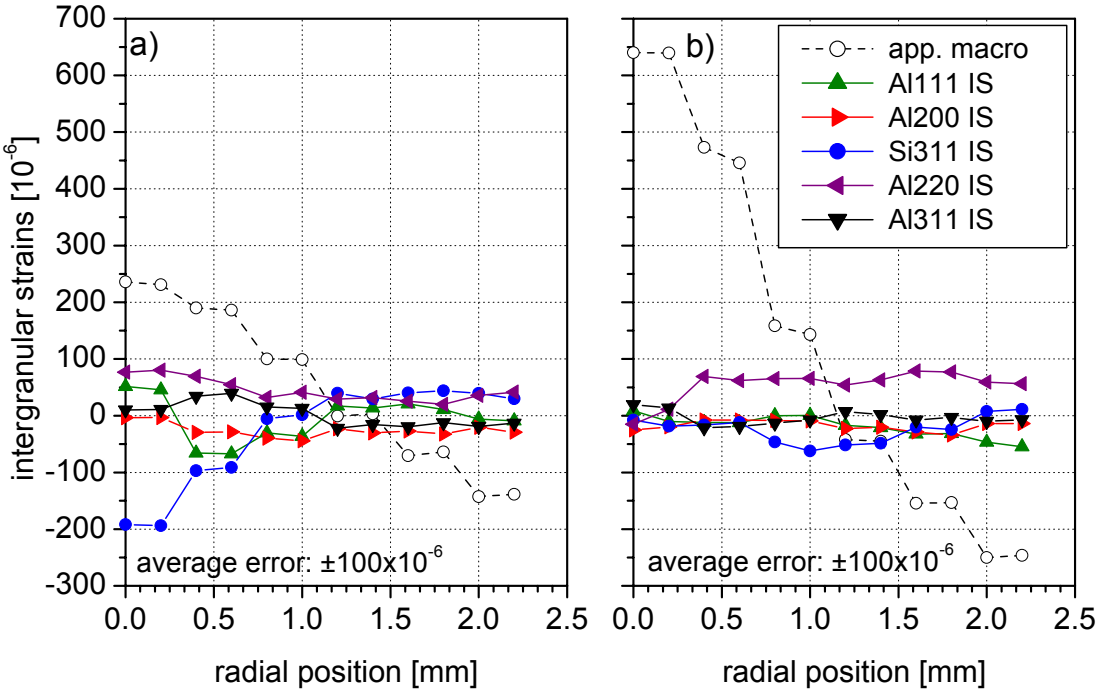

Figure 5.31: Radially dependent ε22 (axial) component of the residual intergranular strain within an AlSi25Cu4Mg1 torsion sample for a deformation of $\gamma = 0.15$ (a) and $\gamma = 0.30$ (b), respectively; dotted line: respective component of the residual macrostrain tensor. Average error: $\pm 1 \times 10^{-4}$.

Table 5.3 gives an overview of the significant residual intergranular stress components at two selected radial positions and for the two deformations. They were calculated using the same assumptions as for the residual macrostress tensor.

Table 5.3: Overview of values of selected intergranular stress components for different phases and hkl, sorted after the two deformations and for one selected radial position close to the sample center and another close to the sample surface, (average error: ±10MPa).

stress tensor component	hkl	radial position	r = 0.4mm	radial position	r = 2.2mm
		$\gamma = 0.15$	$\gamma = 0.30$	$\gamma = 0.15$	$\gamma = 0.30$
	macro	-5	-7	-29	-53
σ_{11} in MPa	Al 111	5	2	-22	-16
(tangential	Al 200	14	11	-4	5
direction)	Al 220	1	2	-1	-4
	Al 311	5	14	10	11
	Si 311	-42	-65	0	-18
	macro	-13	-17	33	36
σ_{12} in MPa	Al 111	8	6	12	15
(previous	Al 200	16	19	19	17
load shear	Al 220	5	10	6	6
direction)	Al 311	9	9	11	8
	Si 311	-66	-77	-84	-8
	macro	15	39	-27	-50
σ_{22} in MPa	Al 111	-4	-7	-10	-12
(axial	Al 200	5	-2	-2	3
direction)	Al 220	4	-1	-1	-2
	Al 311	2	0	5	6
	Si 311	-17	11	2	-8

5.2.3.2 Observed and simulated texture within AlMg3

For the determination of the local texture within the solid AlMg3 torsion sample, the same data set was used as for the determination of the macrostrain tensors (see chapter 5.2.3.1). The radially and deformation dependent ODFs were calculated from the incomplete experimental polefigures of the Al 220, 222, 331, and 422 reflections (see chapter 4.2.5.4). The 111 and 200 polefigures, represented in stereographic projection in figures 5.32 to 5.34, are recalculated from the ODFs. In order not to overcomplicate the diagrams, the polefigures are only shown for the selected radii r = 0.5, 1.3, and 2.1mm, though they were obtained for the same radial step width as the strain tensors in figure 5.21. The S3 (radial) direction is always pointing normal to the plane of the paper. The other sample directions, as well as the direction of the deformation shear, are shown only once in each of the three figures. At the bottom of the figures a schematic representation of the ideal orientations is plotted as a reminder (see also figure 2.4 and table 2.2).

Throughout the 111 polefigures, the strong 111 pole in S2 direction persists. It has its origin in the initial strong 111 / 100 fibre texture, visible in the 111 and 200 polefigures for the lowest deformed sample in figure 5.32 at r = 0.5mm. Note that the deformation in that part of the sample is about $\gamma = 0.30$ since it decreases linearly from the maximum at the sample surface to zero at the center. The higher 111 pole figure maximum at r = 1.3mm could either indicate the radial non-homogeneity of the initial fibre texture or it could be an artifact from the ODF calculation, due to the incomplete input polefigures. The development of the maxima in all the other polefigures is consistent with the expectation that the strength of the initial texture should decrease with increasing deformation. The 200 polefigures exhibit, similarly to the 111 polefigures, the influence of the initial 100 fibre texture. But, contrary to the 111 polefigures, the polefigure maximum decreases much faster (c.f. at r = 0.5, decreases from about 10 at $\gamma = 1.5$ to about 5 at $\gamma = 3.5$) with increasing γ and r and is situated, at higher deformations, at the 10 or 2 o'clock position. However, the initial 111 and 100 poles in axial direction should not disappear since they represent one of the ideal orientations (A and C respectively) of the torsion texture.

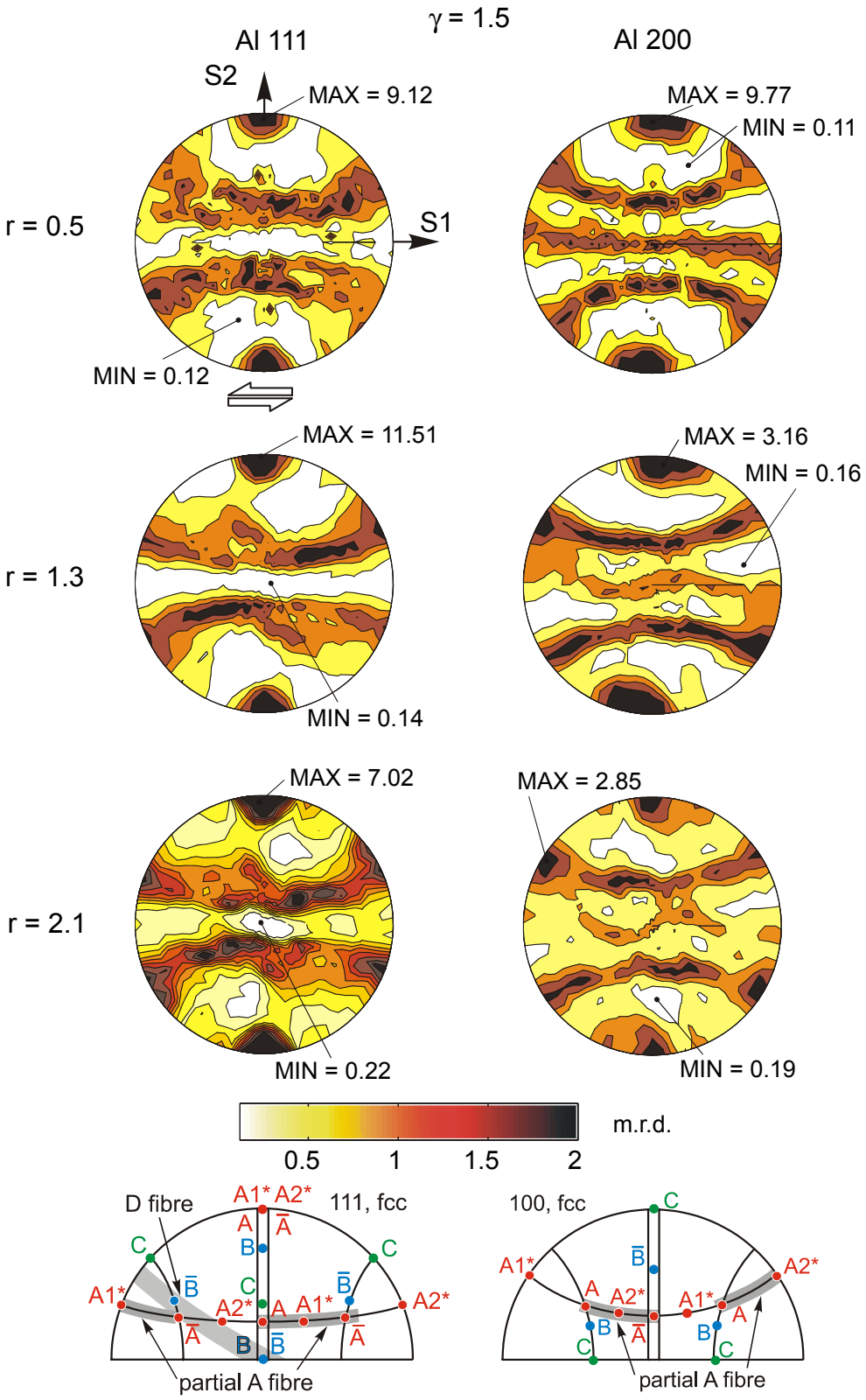

Figure 5.32: Recalculated polefigures in stereographic projection for the radially dependent texture within a solid AlMg3 torsion sample deformed to $\gamma = 1.5$. S3 (i.e. radial) direction: Normal to the paper plane, shear direction indicated by double arrow, polefigures at the bottom show schematically the ideal orientations.

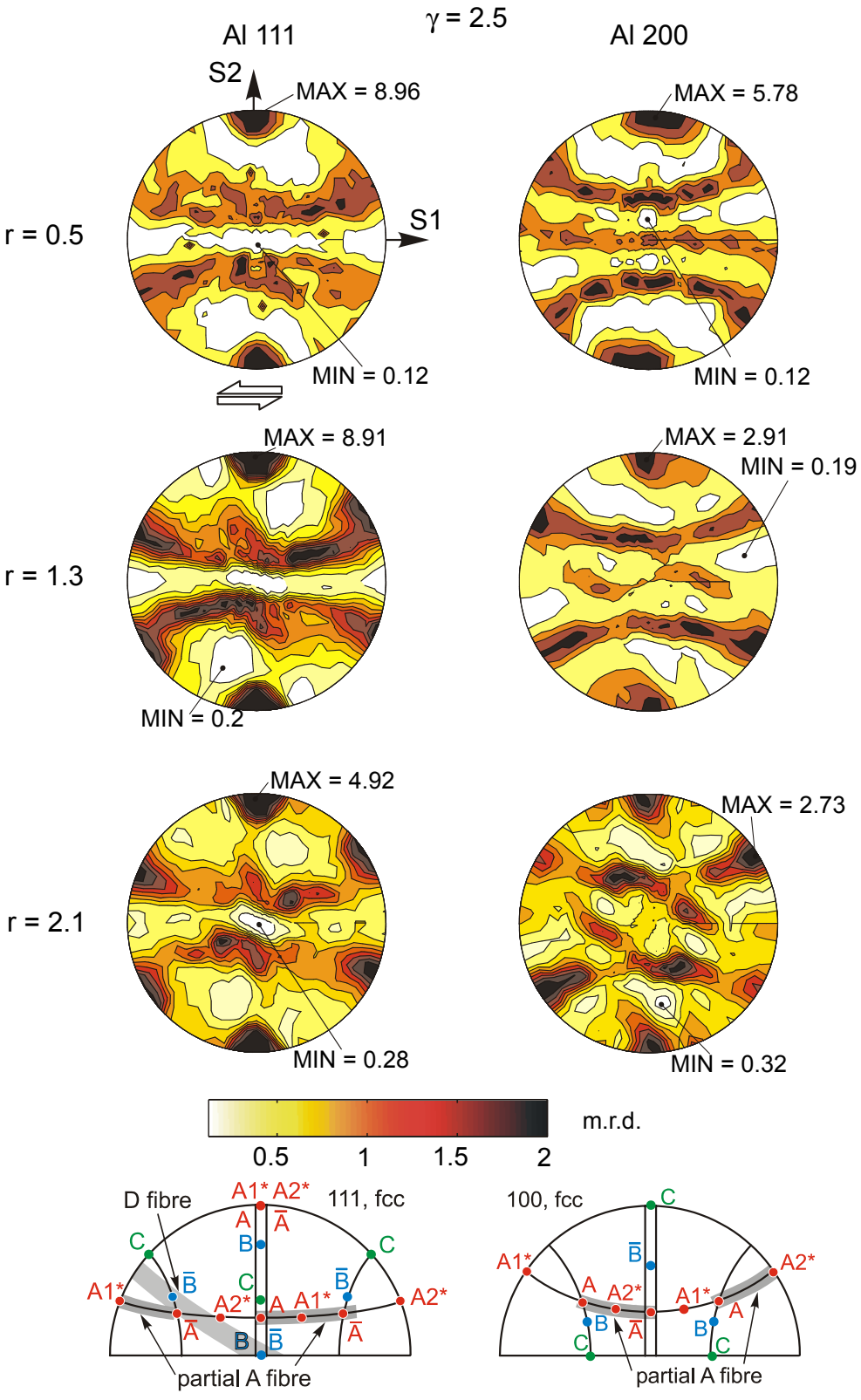

Figure 5.33: Recalculated polefigures in stereographic projection for the radially dependent texture within a solid AlMg3 torsion sample deformed to $\gamma = 2.5$. S3 (i.e. radial) direction: Normal to the paper plane, shear direction indicated by double arrow, polefigures at the bottom show schematically the ideal orientations.

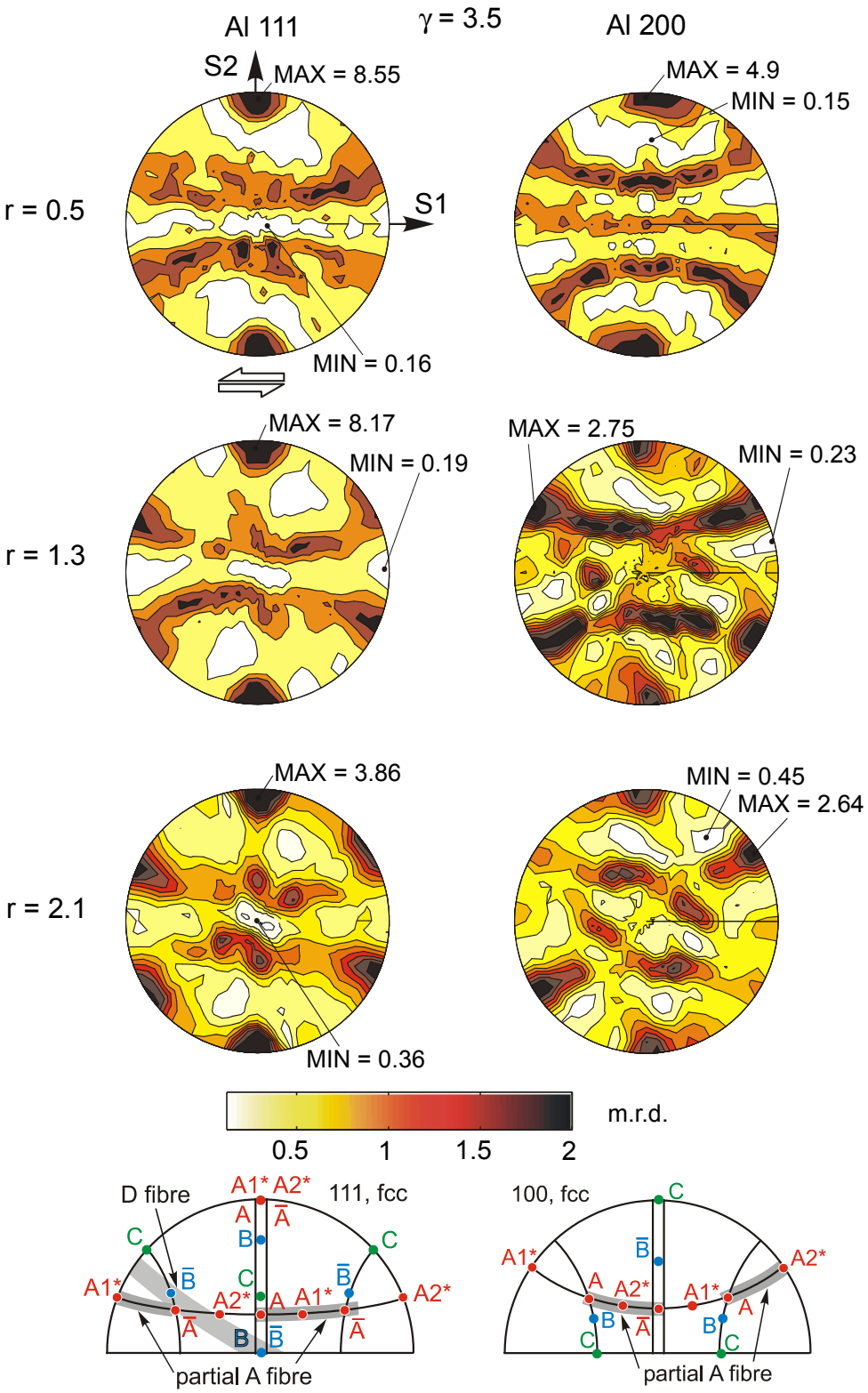

Figure 5.34: Recalculated polefigures in stereographic projection for the radially dependent texture within a solid AlMg3 torsion sample deformed to $\gamma = 3.5$. S3 (i.e. radial) direction: Normal to the paper plane, shear direction indicated by double arrow, polefigures at the bottom show schematically the ideal orientations.

The 111 polefigures show clearly, at low strain, the development of the so-called partial A fibre ({111}<uvw> fibre) (see figure 5.32, r = 1.3 and 2.1mm). With increasing deformation, the A^*_1 and A^*_2 orientations become stronger and the strength of the partial fibre decreases (see figure 5.33, r = 2.1 and figure 5.34, r = 1.3mm). At the highest deformation (figure 5.34 at r = 2.1mm, i.e. actual deformation: 1.3), the A^*_1 orientations are dominant. The band that points from the center of the 111 polefigure towards the 4 and 10 o'clock position could be the so-called D fibre [Koc 1998, p. 189]. Montheillet *et al.* [Mon 1984] reported, for fixed end torsion, the development of the B orientation and observed no D fibre for Al. Here, in the case of free end torsion, the B orientation seems to be absent in all polefigures. However, the poles at the 12 and 6 o'clock positions at the center of the 111 polefigure (most visible at highest deformation) can be interpreted as the C component which is just a special case of the B orientation. Only small indications of a rotation of the texture with increasing strain were found for the 111 polefigures. At $\gamma = 1.5$ and r = 2.1, the texture seems to be slightly rotated ccw (visible in the center at the supposedly C orientation). This rotation seems to decrease with increasing strain when comparing this polefigure to the corresponding one at $\gamma = 3.5$. The reason for these weak indications might be the influence of the initial texture.

However, a clear rotation is observed in the 200 polefigures. In the sequence of 200 polefigures, shown in figure 5.32, the outer part of the polefigure at r = 0.5 indicates a cw rotation of the C orientation. At r = 1.3, the inner polefigure region shows a change of the sense of rotation to ccw for the C orientation. This change of rotation is less visible in the outer part of the same polefigure. This might be due to the strong initial texture. Nevertheless, at higher deformations (figures 5.33 and 5.34) this ccw rotation is also observable at the outer 200 polefigure parts. The observed change of the rotation sense is accompanied by a change of the relation between A^*_1 and A^*_2. At lower deformations, A^*_1 dominates the A^*_2 orientation (see figure 5.32, maximum in 200 polefigure at r = 2.1mm and figure 5.34, maximum at r = 1.3mm). The final texture shows an inversion of the relation: A^*_2 largely dominates the A^*_1 orientation (see chapter 5.2.3.5 for the link between axial stresses and change of texture). The dominance of the A^*_1 and the A^*_2 orientation in the 111 and 200 polefigures, respectively, is in agreement with modelling by Canova *et al.* [Can 1984]. Note that, in this reference the simulations were carried out for positive shear, i.e. opposed to

the present case. In order to make comparisons, the polefigures need to be mirrored along the S2 axis.

Although the polefigures obtained from the experimental data give some detailed insight in the texture development, it should be kept in mind that the interpretations have to be made carefully. Very detailed conclusions drawn on distinct orientations require a larger input of experimental data.

The simulation of the deformation texture was carried out using the VPSC5 code by Lebensohn *et al.* [Leb 1993]. A linear hardening law was chosen using τ_0 = 0.85MPa and θ_0 = 113MPa for the critical shear stress and the hardening constant of AlMg3, respectively [Lan-1]. The components of the macroscopic velocity gradient tensor

$$\begin{pmatrix} -0.0002 & -1 & 0 \\ 0 & 0.0004 & 0 \\ 0 & 0 & -0.0002 \end{pmatrix}$$

were determined from the sample dimensions before and after deformation. The final deformation of $\gamma = 1.3$ was achieved in 64 incremental steps of $\Delta\gamma = 0.02$. This deformation corresponds to an actual deformation at r = 2.1mm of the sample deformed to $\gamma = 1.5$. The simulation was carried out for a set of 5000 grains whose orientations represented the initial 111 / 100 fibre texture. A comparison between the experimental 111 and 200 polefigures for $\gamma = 1.5$ and r = 2.1mm and the simulated ones is presented in figure 5.35. The model is able to predict the principal features of the experimental polefigures such as the partial A fibre in the 111 polefigure, and the intensity relation between the positions at 2 o'clock and 10 o'clock. But the well-known problems with texture modelling are clearly visible. The predicted changes in the pole densities show strong inconsistencies with the experimental data: The decrease of the initial 111 fibre is too weak, the A^*_1 / A^*_2 orientations are too weak and the A / $\overline{A}$ orientations are too strong. In the simulated 200 polefigure the decrease of the initial 100 fibre seems to be too strong and the polefigure maximum is almost twice the experimentally determined one. However, the maxima in both simulated polefigures are situated in equivalent regions compared to the experiment. As in the experiment, the B orientation seems also to be absent in the simulation. The C orientation in the 200 polefigure does not show a rotation as it does in the experiment. The main reasons for this partial failure of the model might be the following:

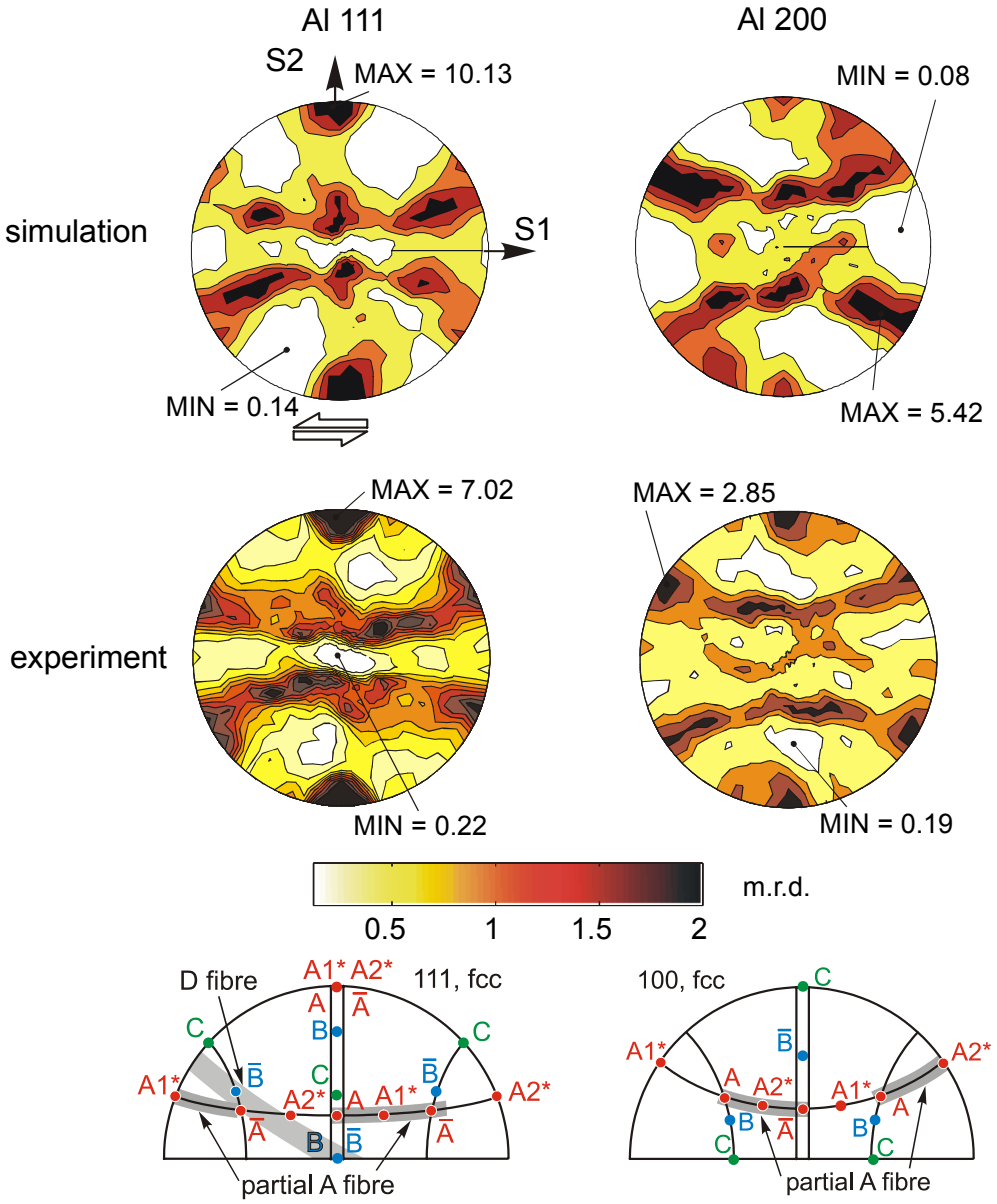

Figure 5.35: Comparison of simulated texture and texture observed in a solid AlMg3 torsion sample deformed to $\gamma = 1.5$ at r = 2.1mm (i.e. actual deformation 1.3). 111 and 200 polefigures are shown in stereographic projection, S3 (i.e. radial) direction: Normal to the paper plane, shear direction indicated by double arrow. The polefigures at the bottom show schematically the ideal orientations.

Most of the available models, the VPSC5 code included, are not able to model the deformation of a material in which a strong deformation gradient is present. They always assume a homogeneous, possibly triaxial, deformation over the sample cross section. Especially within solid torsion samples, the coupling between differently deformed layers seems to be important for a successful modelling. All the examples in the literature always refer just to the surface layer of the torsion sample [Can 1984,

Mon 1984, 1985, Jon 1993]. However, a more extensive study of the modelling is beyond the scope of this work

5.2.3.3 Observed and simulated microstrains within AlMg3

The radially and deformation dependent crystallite microstrains, obtained from the same data set as the polefigures and the macrostrain tensors (see chapters 5.2.3.1 and 5.2.3.1), are shown in figures 5.36 to 5.39.

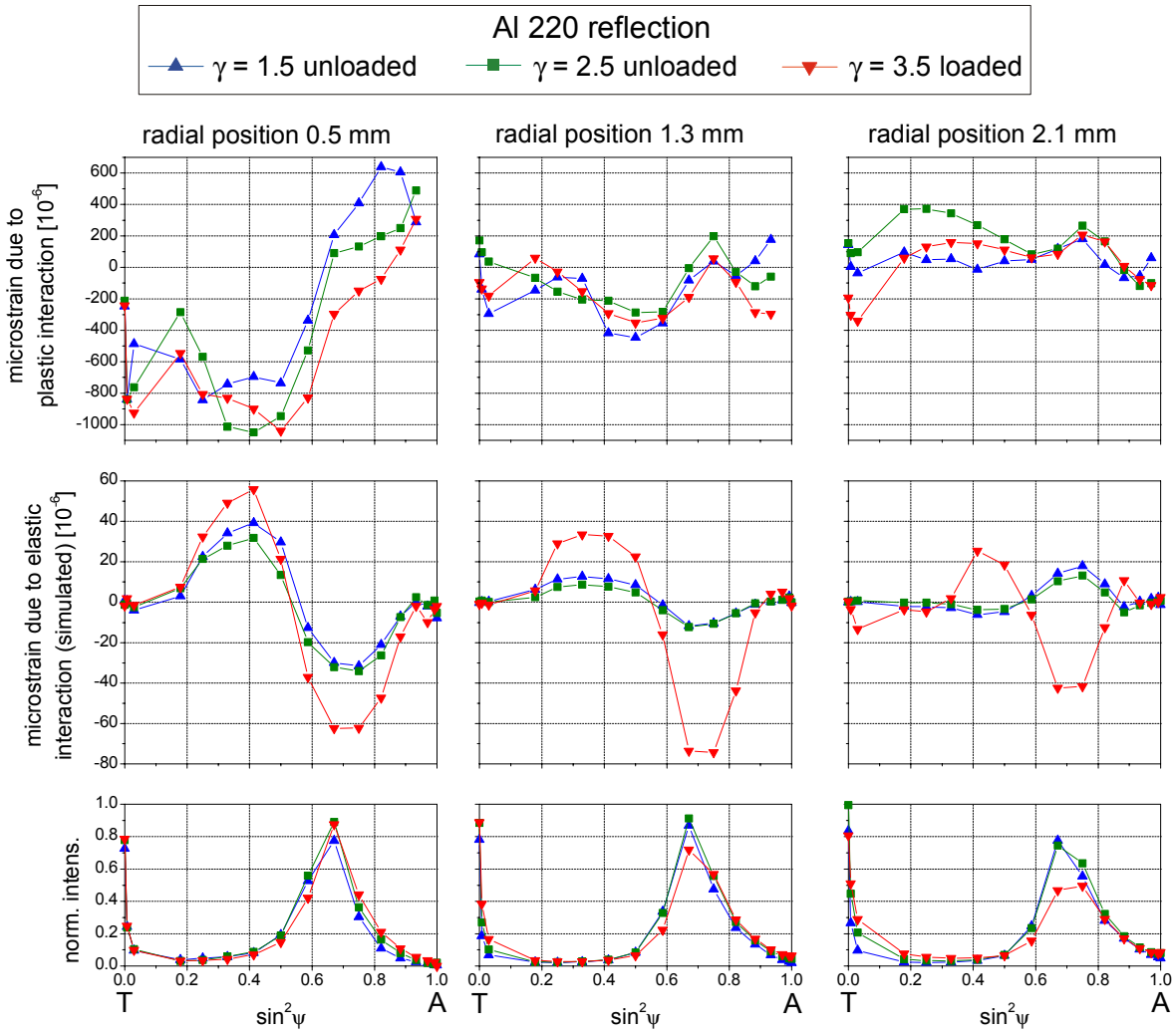

Figure 5.36: Microstrain and intensity distributions at different radial positions within a solid AlMg3 torsion sample at different deformations, for the 220 reflection, T and A indicate the tangential and axial direction respectively, ε^e: Simulated, ε^p: derived from experimentally observed strain by subtracting ε^e. Average experimental uncertainty: $\pm 150 \times 10^{-6}$.

Each of the figures contains the intensity and strain vs. $\sin^2\psi$ plots in axial direction for a specific reflection (Al 220, 222, 331, and 422). The same conventions as for the plots in chapter 5.2.2.1 apply. The crystallite microstrains are separated into the part due to elastic interaction (ε^e) and the part due to plastic interaction (ε^p). This was achieved by simulating the ε^e using the Reuss model in combination with the respective ODF (see chapter 2.4.2). The ε^p are obtained by subtracting the simulated ε^e from the experimentally determined crystallite microstrains (see chapter 4.2.3.2).

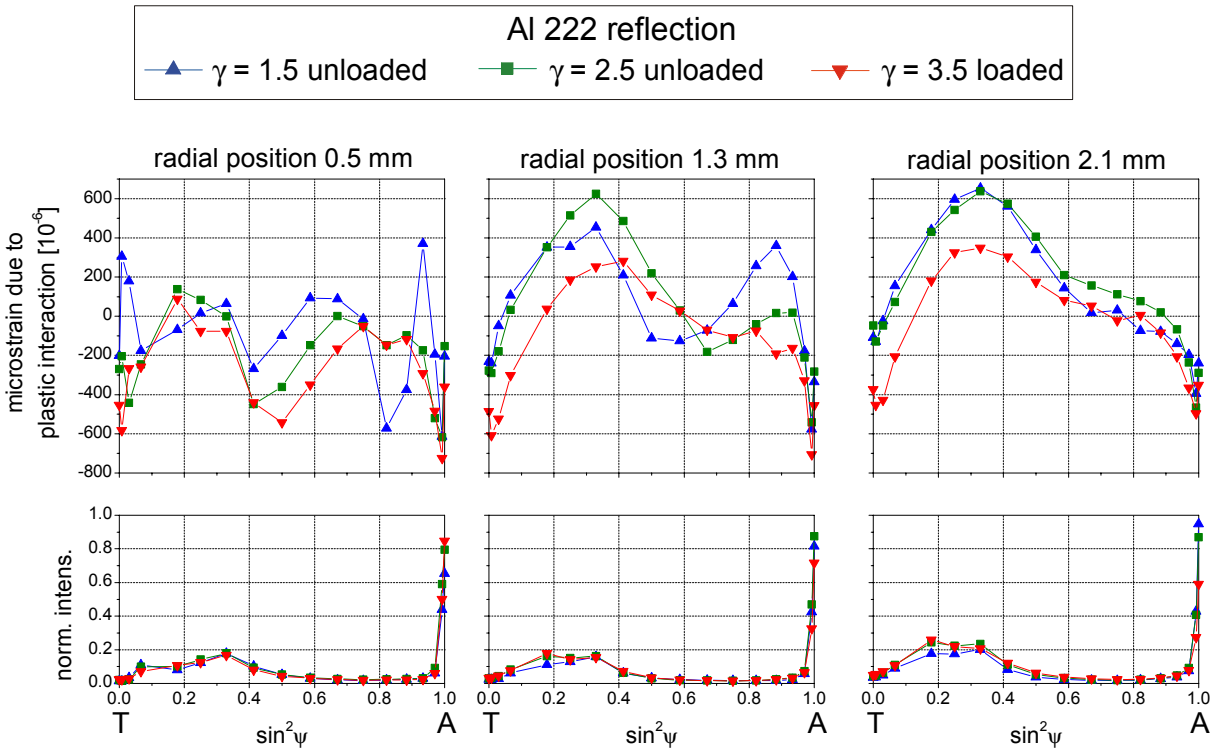

Figure 5.37: Microstrain and intensity distributions at different radial positions within a solid AlMg3 torsion sample at different deformations, for the 222 reflection. T and A indicate the tangential and axial direction, respectively. Average experimental uncertainty: ±150x10^{-6}.

It is obvious that the ε^e have only a minor influence, since they are about one order of magnitude smaller than the ε^p. This can be explained by the elastic quasi-isotropy of Al. In the present case, the crystallite microstrains are largely dominated by the influence of the plastic anisotropy. Therefore, the elastic Reuss model, in combination with the ODF, is not able to predict the experimental observations. The 222 reflection, for example, shows large ε^p with peak to valley values of up to 1200x10^{-6}. The ε^e, however, are zero and therefore not plotted. This is inherent to the

Reuss model which predicts no microstrain due to elastic interaction for the {h00} and {hhh} reflections. Nevertheless, the simulation of the crystallite microstrains due to elastic interaction does permit an estimation of their value and of the influence of the texture. Note that the ε^e for $\gamma = 3.5$ are always much larger since these are calculated, based on the macro load stress and not the macro residual stress.

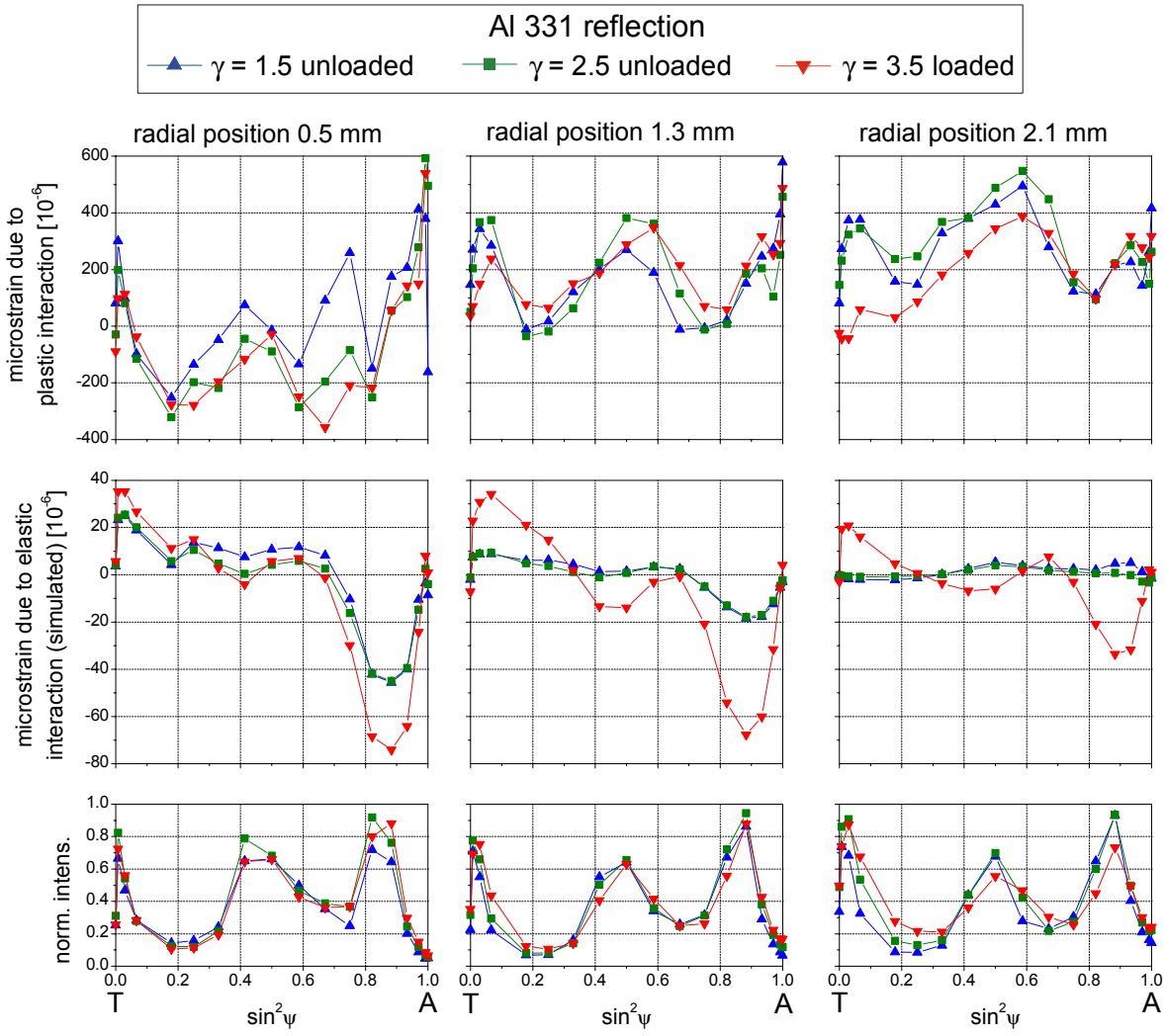

Figure 5.38: Microstrain and intensity distributions at different radial positions within a solid AlMg3 torsion sample at different deformations, for the 331 reflection, T and A indicate the tangential and axial direction, respectively; ε^e: Simulated; ε^p: Derived from experimentally observed strain by subtracting ε^e. Average experimental uncertainty: $\pm 150 \times 10^{-6}$.

The inversion of the crystallite microstrain due to elastic interaction for the highest deformation $\gamma = 3.5$, shown here at r = 2.1 for all hkl concerned, can be explained simply by the fact that the signs of the macrostress tensor at this position are inverted also with respect to the lower deformations (see figure 5.22).

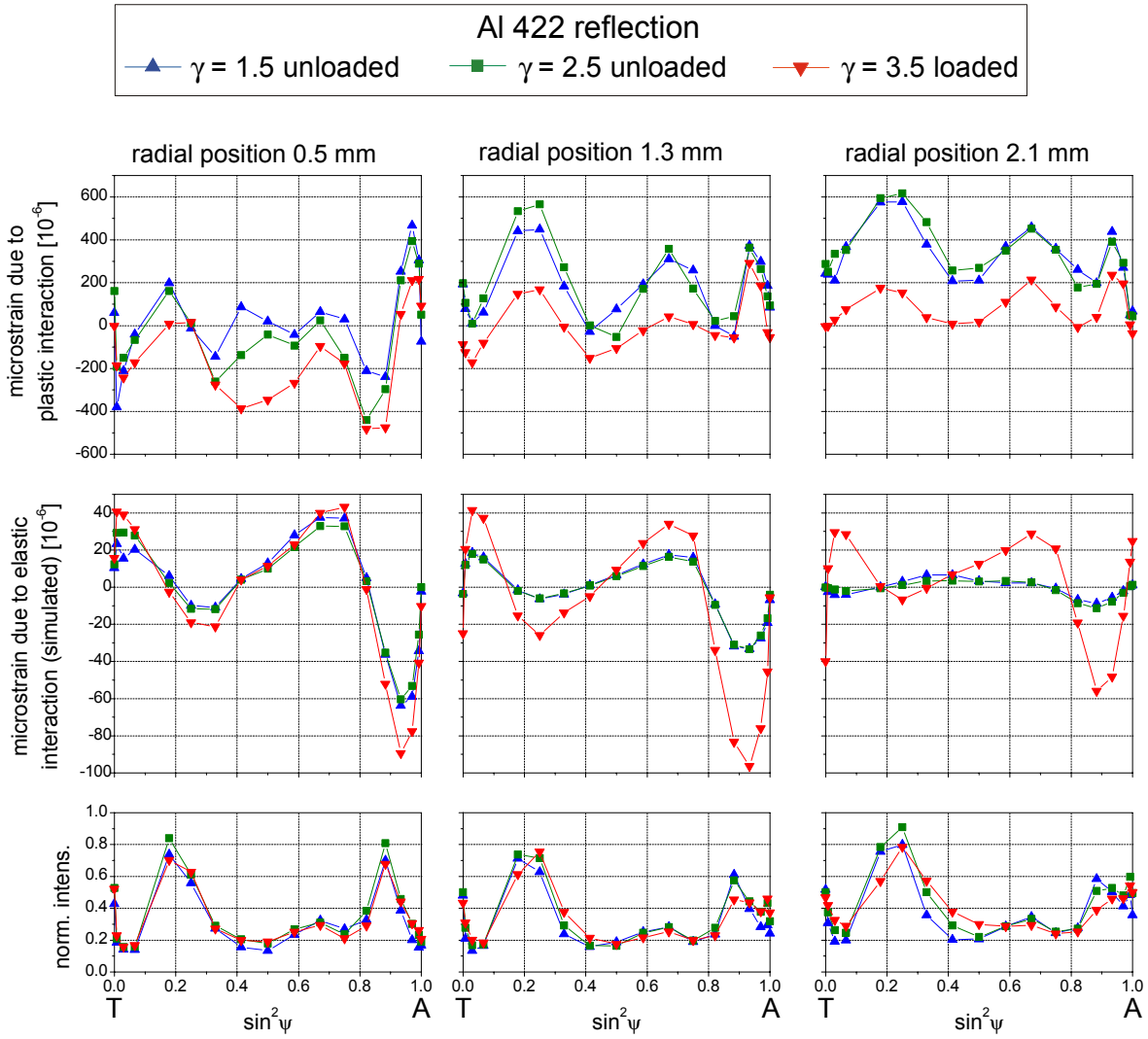

Figure 5.39: Microstrain and intensity distributions at different radial positions within a solid AlMg3 torsion sample at different deformations, for the 422 reflection, T and A indicate the tangential and axial direction respectively; ε^e: Simulated; ε^p: Derived from experimentally observed strain by subtracting ε^e. Average experimental uncertainty: $\pm 150 \times 10^{-6}$.

As already observed for the biaxially deformed samples (see chapter 5.2.2.1), the peak to valley values of the crystallite microstrains mostly decrease with increasing deformation. They are the largest at r = 0.5mm / γ = 1.5 and the lowest at r = 2.1 / γ = 3.5. At the same time sharp crystallite microstrain profiles become smoother with increasing γ (see e.g. figure 5.22, r = 0.5 and 1.3mm). However, at first sight these large changes do not seem to be correlated to a large change in the intensity profiles. But a closer investigation reveals which grain orientations are actually causing these changes in the microstrain profiles. In order to illustrate this, it was calculated which grain orientations are contributing to 80% of the intensity observed in a selected $\sin^2\psi$ range on a specific reflection. The filter value of 80% was chosen in order to enhance the readability of the plots. The grain orientations are represented in the form of inverse pole figures for the S3 (radial) direction. The two orientation triangles 001 / 101 / 111 and 001 / 011 / 111 represent the most general representation for the ODF of cubic crystals when a symbolization, similar to the one first proposed by van Houtte *et al.* [Hou 1976], is employed. It consists of not only indicating the orientation of the S3 axis by a dot but by adding a flag to the dot which indicates the direction in which the S1 (tangential) sample axis is pointing with respect to the 001 point. The orientation of the S2 (axial) direction (i.e. shear plane normal) of the sample coordinate system can then be derived, keeping in mind that it is a right-handed system. Additionally to the direction of the flag its length indicates the pole density at this orientation. The relatively coarse representation is due to the fact that the ODF was only calculated for a 5°x5°x5° raster.

Figure 5.40 shows for the 222 reflection how the pole density of the contributing grains in the $\sin^2\psi$ range of 0.75 to 0.97, for the radial position r = 0.5, changes. The correspondent microstrains (see figure 5.37) exhibit, in this $\sin^2\psi$ range, a sharp peak for γ = 1.5 and a smoother profile for the higher deformations. The corresponding range of the intensity profile displays almost no changes. However, figure 5.40 shows that significant changes take place in the partition of the contributing orientations. The pole densities of the marked orientations increase significantly with increasing deformation, especially from γ = 1.5 to 2.5, while the other orientations remain stable. This suggests that mainly the changes at the marked orientations contribute to the smoothening of the sharp microstrain peak and that, once the texture is more stable, also the crystallite microstrains stay stable. Detailed information of this kind can be especially helpful for the verification of plasticity models.

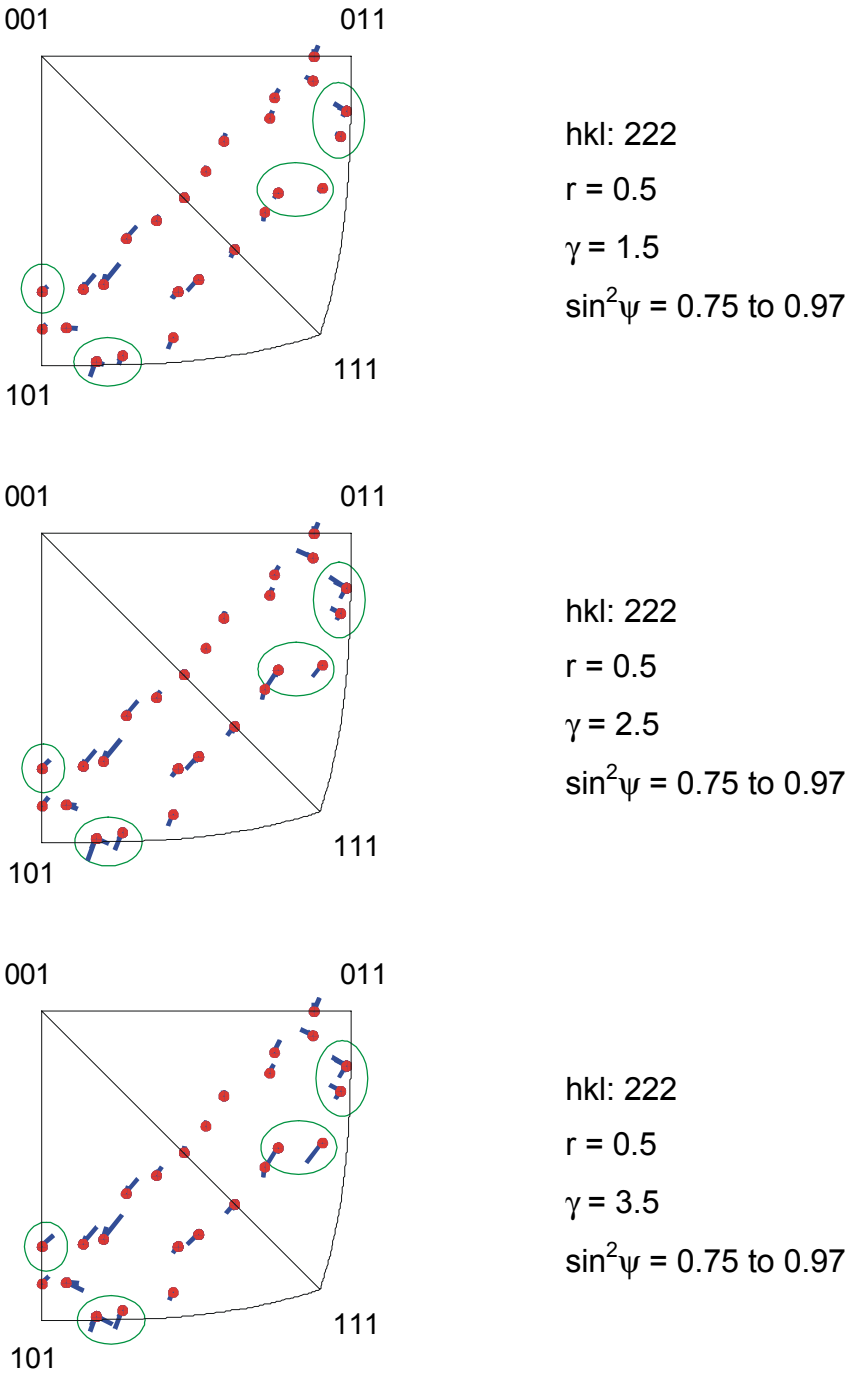

Figure 5.40: Change with increasing deformation γ of the pole density of the grain orientations contributing to the detected signal for the Al 222 reflection in the indicated $\sin^2\psi$ range. The dots in the inverse polefigures indicate the orientation of the S3 axis, the flag indicates the direction of the S1 axis and the length of the flag scales with the pole density.

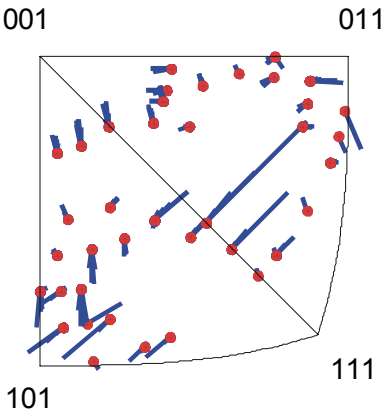

hkl: 422
r = 1.3
γ = 1.5
$\sin^2\psi$ = 0.03 to 0.25

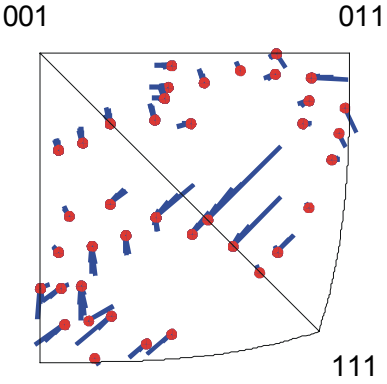

hkl: 422
r = 1.3
γ = 2.5
$\sin^2\psi$ = 0.03 to 0.25

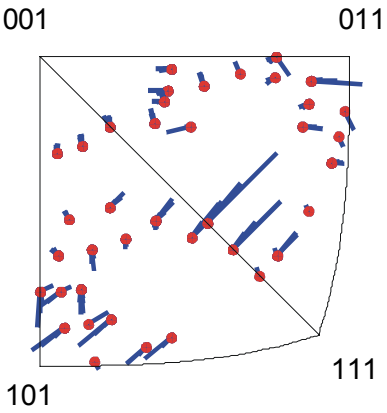

hkl: 422
r = 1.3
γ = 3.5
$\sin^2\psi$ = 0.03 to 0.25

Figure 5.41: Change with increasing deformation γ of the pole density of the grain orientations contributing to the detected signal for the Al 422 reflection in the indicated $\sin^2\psi$ range. The dots in the inverse polefigures indicate the orientation of the S3 axis, the flag indicates the direction of the S1 axis and the length of the flag scales with the pole density.

Figure 5.41 presents a different development of the pole densities. The figure relates to the $\sin^2\psi$ range of 0.03 to 0.25, at r = 1.3mm, of the 422 reflection (see figure 5.39). Again the crystallite microstrain profile becomes smoother and the corresponding intensity profiles show only small changes with increasing deformation. But, contrary to the previous example, basically all orientations exhibit either an increase or a decrease of their pole density. This leads to a significant homogenization of the pole densities and could explain the decrease in the crystallite microstrain. No crystallite microstrains due to elastic interaction should be observable in a random textured sample, however, this is not the case for the microstrains caused by plastic interaction.
Please refer to chapter 5.2.4 for a summary of the microstrains observed for the different deformation modes.

5.2.3.4 In-situ observation of dynamic texture and strain development within AlMg3

The fast data acquisition in this experiment using the conical slit system setup (see chapter 4.2.1.2) permitted the in-situ observation of the dynamic evolution of the texture and the strain tensor within a solid AlMg3 torsion sample. The results are presented in figures 5.42 to 5.44, for the radial position r = 2mm.
Since the deformation was continuous and the acquisition of a complete data set took about 2.5min., each evaluated point actually represents not the texture and strain tensor at a distinct deformation but averages over a deformation of about $\Delta\gamma = 0.35$.
It is obvious that the quality of the texture data is not as good as in the static measurements presented above. This is due to the constraints of the experimental setup (see chapter 4.2). The sometimes not satisfying point symmetry of the polefigures (e.g. punctual maxima close to the center) are certainly artefacts from the ODF calculations. However, though no detailed observations on the texture are possible, the data shows clearly the general development of the texture from the initial 111 / 100 fibre texture to a texture showing typical features of a torsion texture (see chapter 5.2.3.2).

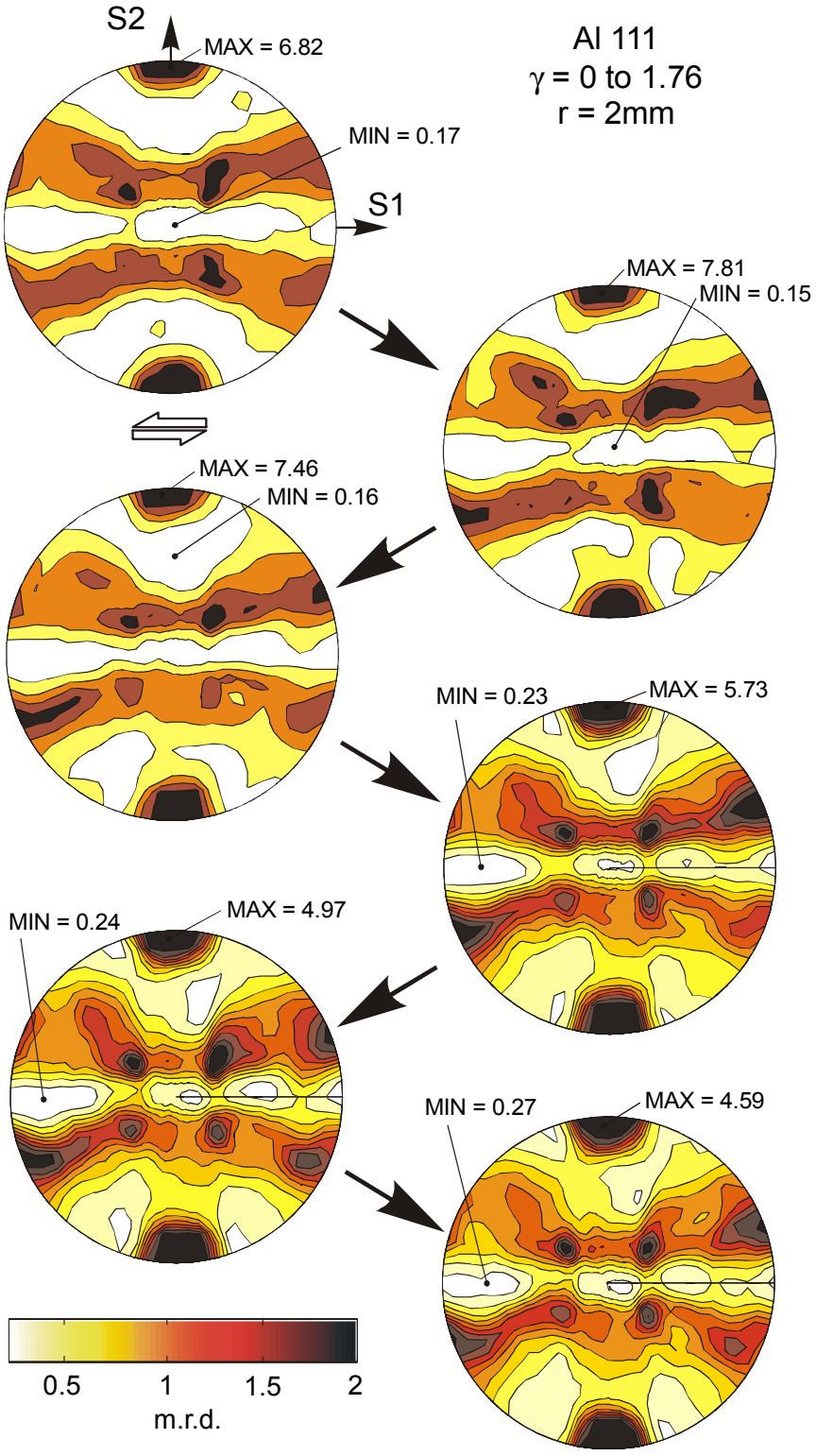

Figure 5.42: Recalculated 111 polefigures in stereographic projection for the dynamic texture evolution observed in-situ within a solid AlMg3 torsion sample at r = 2mm. S3 (i.e. radial) direction always points out of the paper plane, shear direction indicated by double arrow.

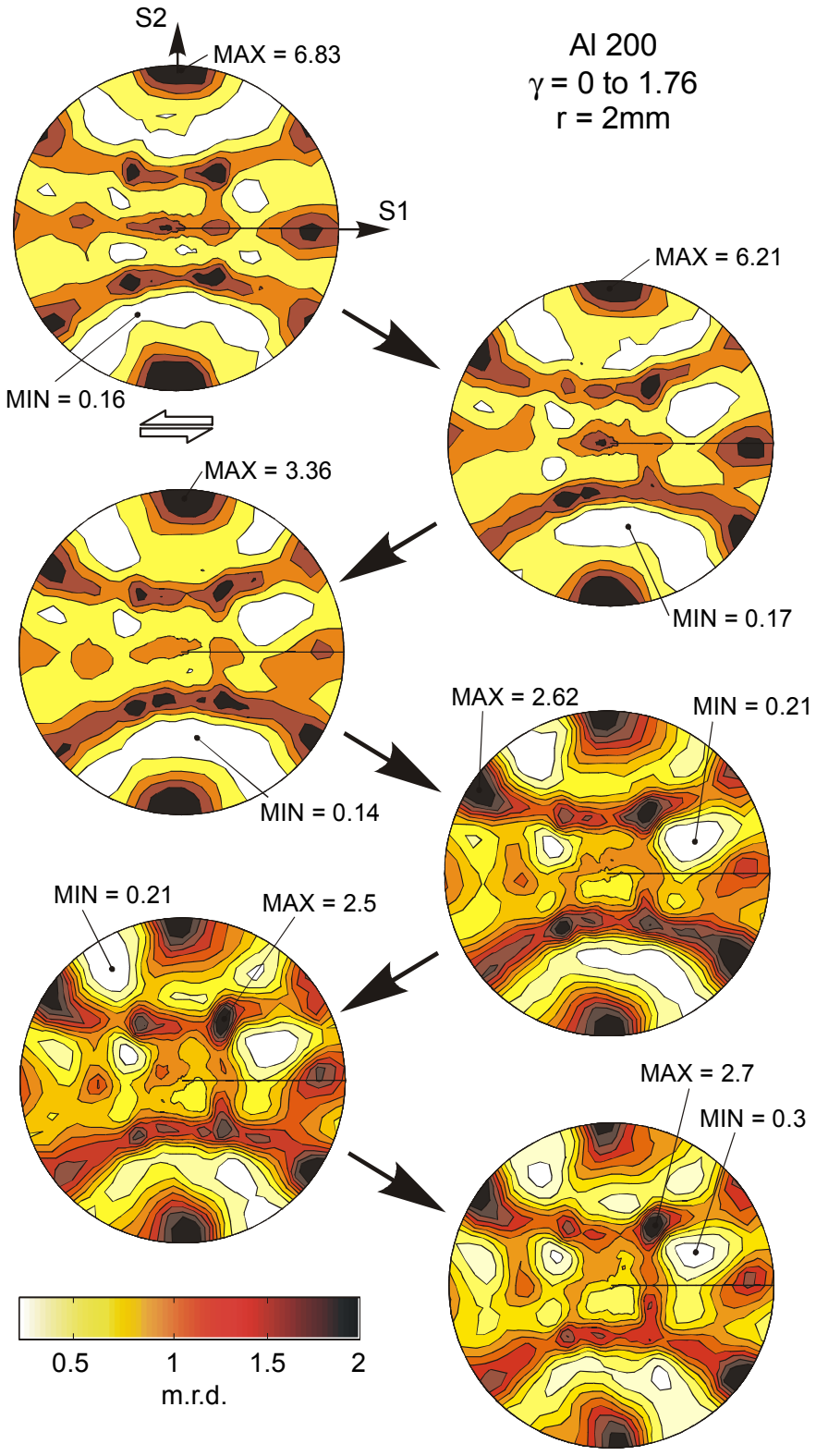

Figure 5.43: Recalculated 200 polefigures in stereographic projection for the dynamic texture evolution observed in-situ within a solid AlMg3 torsion sample at r = 2mm, S3 (i.e. radial) direction always points out of the paper plane, shear direction indicated by double arrow.

The development of the pseudo macrostrain tensor observed on the 220 reflection is presented in figure 5.44. The abscissa shows the actual deformation at r = 2mm. The overall deformation of the sample was $\gamma = 2.2$. The development of the load shear component $\varepsilon 12$ is well observable. Due to the experimental setup the experimental uncertainty is larger than in the static experiments (smaller distance between detector and slit for dynamic in-situ measurements, see chapter 4.2.1.2). The strain tensor at the onset of deformation has to be interpreted very critical (e.g. the axial strain component $\varepsilon 22$). The influence of the friction in the clamps which constrain the axial mobility of the sample might play a major role.

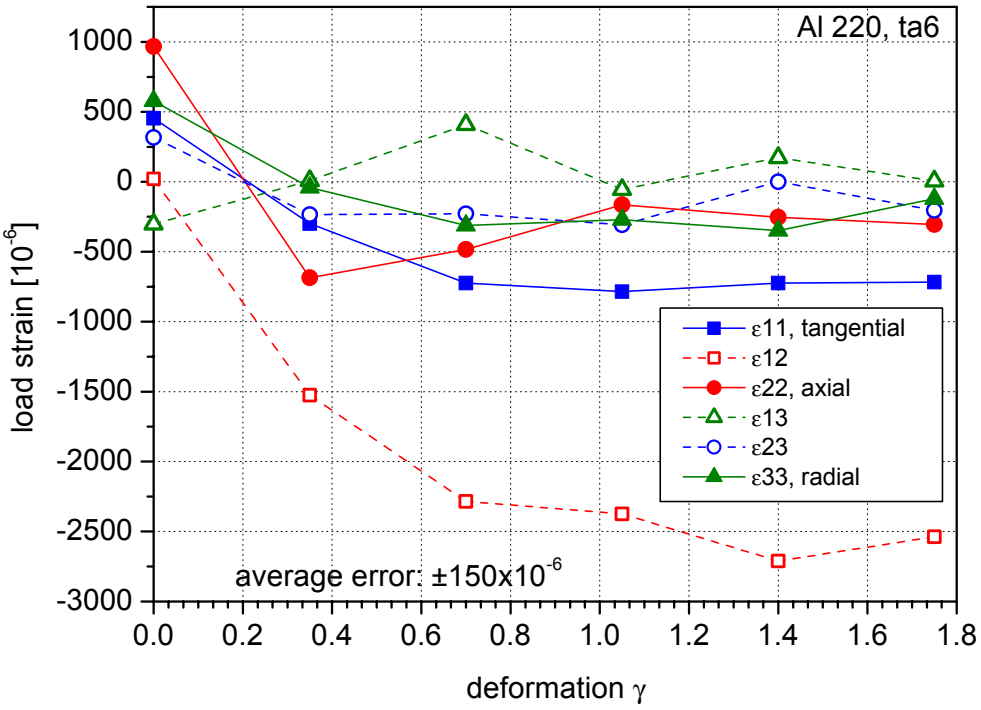

Figure 5.44: Dynamic evolution of the pseudo macrostrain tensor measured in-situ on the Al 220 reflection at r = 2mm. The sample crack occurred shortly after reaching the maximal deformation. The continuous deformation until failure took about 15min.

Neglecting the first data point, the development of the compressive strain in the axial direction indicates that the axial forces and, therefore, the sample elongation are the strongest around $\gamma = 0.35$. Above that deformation, the axial forces decrease until about $\gamma = 1$ and then seem to start again to become stronger. Unfortunately, the sample failed shortly after that turnpoint so it was not possible to verify if this

apparent increase of the compressive strain is just within the experimental uncertainty or a real trend. Montheillet *et al.* [Mon 1985] observed and predicted, for fixed end torsion, an increase of the axial compressive force until $\gamma = 0.9$, above that a decrease and than an increase at about $\gamma = 2.9$. However, their observations represent an integration over the whole sample cross section and not the observations on a distinct radial position within the sample.

5.2.3.5 Observations on the Swift effect within solid torsion samples

Since the Swift (or axial) effect is one of the particular characteristics of torsional deformation, it shall be discussed here by considering the above presented results from the solid torsion samples for the macrostrains, macrostresses, intergranular strains and the texture.

In the solid AlMg3 torsion sample, the axial stress close to the center is constantly decreasing with increasing deformation (from about 40MPa to 20MPa). The compressive residual stresses close to the surface can be explained in the way that the outer regions of the torsion sample tend to elongate due to the texture development, while this elongation is constrained by the inner, almost undeformed regions. The decrease of the axial stresses close to the center would then mean that the inner parts also start to form a torsion texture. In fact, this can be seen in the corresponding polefigures (figures 5.32 to 5.34). Looking at the intergranular strains in axial direction, the tensile intergranular strains for the 220 reflection decrease too with increasing deformation (in average from 250×10^{-6} to 100×10^{-6}). Moreover, the 220 reflection is the only one that shows large tensile intergranular strains and a strong dependence on the deformation.

The axial macrostress component in the solid AlSi25Cu4Mg1 sample increases by $\Delta\sigma 22 = 40$MPa when increasing the deformation from $\gamma = 0.15$ to 0.30. In the same sample, the intergranular strains observed in the axial direction on the 220 reflection increase clearly from on average 50×10^{-6} to on average 80×10^{-6} (see figure 5.31a and b), while the intergranular strains of the other reflections, here, only show changes close to the center. Considering the low deformations $\gamma = 0.15$ and 0.30, of the AlSi25Cu4Mg1 sample and the high deformations $\gamma = 1.5$, 2.5, and 3.5, of the AlMg3 sample the following conclusion can be made: Assuming that the Al phase in the AlSi25Cu4Mg1 sample exhibits a comparable behaviour as the AlMg3, it seems

that the development of axial forces is very strong at the onset of the torsional deformation and reaches a turnpoint around $\gamma = 0.35$. Montheillet *et. al.* [Mont 1984] observed such a turnpoint, in fixed end torsion, at a deformation of about 0.5 (see also chapter 5.2.3.4). The development of the axial forces seems to be closely linked to the strain evolution in the 220 crystal direction, the development of the A^*_1 / A^*_2 texture component, and the cw rotation of the C texture component, as observed for AlMg3. Prior to this cw rotation of the C orientation, there must have occurred a ccw rotation because this component is already rotated ccw in the 111 polefigure for $\gamma = 1.5$ at r = 1.3, which corresponds to an actual deformation of about 0.78. The initial fibre 111 / 100 texture was unfortunately so strong that it was not possible to detect the C orientation at lower deformations.

5.2.4 Summary of the crystallite microstrains occurring at different deformation modes

An overview of the crystallite microstrains observed for the uniaxial, biaxial, and triaxial deformation modes is given in table 5.4. It summarizes the data of the relevant previous chapters (chapters 5.2.1.1, 5.2.1.2, 5.2.2.1, and 5.2.3.3). The table shows the peak to valley values of the microstrain oscillations and the respective largest amplitude of the curve, noted in brackets. The deformations of the torsion samples are also given as natural strain φ in order to allow the comparison with the amounts of compression and tensile deformation. The data for the triaxial deformation originates from the different radial positions within the solid torsion sample, at the deformation step $\gamma = 2.5$. Since the deformation depends linearly on the radial position, the respective actual deformations are given for the three radii r = 0.5, 1.3, and 2.1mm. Note that the microstrains for the sample deformed biaxially to $\gamma = 0.15$ were measured on the positive "ψ branch".
The most striking observation can be observed for the 220 reflection. In uniaxial deformation, this reflection was among the reflections that showed the lowest crystallite microstrains. However, in the case of the biaxial and triaxial deformations, the 220 reflection mostly exhibits the strongest crystallite microstrains. At the lowest triaxial deformation it even shows, with a peak to valley value of 1550×10^{-6}, the largest value of all observed samples and reflections, proving that the microstrains in triaxial deformation are not, in general, negligible. Moreover, the microstrains in the 220 crystal direction show clearly a decrease with increasing triaxial deformation. In contrast to that, in the case of uniaxial deformation the microstrains observed in the

220 direction increase with increasing deformation φ, as is the case for all the other reflections in this deformation mode.

Table 5.4: Overview of the crystallite microstrains observed on different hkl in different deformation modes. The values are given in $1x10^{-6}$ as maximum peak to valley value of the microstrain profile and the maximum microstrain value in brackets.

deform. mode	uniaxial (tens.)	uniaxial (compr.)	biaxial (tt)*	biaxial (tt)*	biaxial (tt)*	triaxial (st)**	triaxial (st)**	triaxial (st)**
deform. φ (γ)	0.25 (-)	0.455 (-)	0.08 (0.15)$^{+}$	0.16 (0.30)	0.21 (0.40)	0.25 (0.5)	0.56 (1.3)	0.79 (2.1)
initial texture	111/100 fibre	111/100 fibre	111/100 fibre	111/100 fibre	111/100 fibre	111/100 fibre	111/100 fibre	111/100 fibre
111/222	400 (200)	1200 (-900)	750 (-400)	800 (450)	750 (400)	750 (-600)	1150 (600)	1100 (600)
200	1000 (-600)	1500 (-900)	950 (620)	1100 (±550)	1000 (±500)	- (-)	- (-)	- (-)
220	500 (-300)	600 (-400)	300 (-280)	1000 (-600)	1000 (-700)	1550 (-1050)	500 (-300)	480 (380)
311	500 (-290)	1100 (600)	380 (210)	600 (-350)	550 (-320)	- (-)	- (-)	- (-)
331	- (-)	- (-)	- (-)	- (-)	- (-)	900 (600)	480 (450)	400 (550)
422	- (-)	- (-)	- (-)	- (-)	- (-)	800 (-420)	580 (580)	550 (600)

*tubular torsion sample; **solid torsion sample

$^{+}$ measured on the positive "ψ branch"

Another interesting development of the crystallite microstrains for the 331 and 422 reflection can be seen for triaxial deformation. With increasing deformation, the microstrains observed on the negative "ψ branch" are shifted in the tensile region which results in the, initially puzzelling, fact that the maximum microstrain (in the brackets) is larger than the respective peak to valley value. The characteristics of the behaviour of the 220 reflection could be seen in connection with the particular development of the axial stresses in the solid torsion sample (see chapter 5.2.3.5) and in the context of C and A* texture components (see chapter 5.2.3.3). However, a more detailed analysis of this aspect would require additional texture measurements and is not intended within the frame of this work.

6 CONCLUSION AND OUTLOOK

The strain state and the texture of AlMg3 and AlSi25Cu4Mg3 samples, which have undergone different uniaxial, biaxial, and triaxial plastic deformations at room temperature, were investigated by energy and angular dispersive x-ray diffraction techniques using high energy synchrotron radiation. The different deformation modes were realized by tension / compression (uniaxial), torsion of tubular samples (biaxial) and the free-end torsion of solid torsion samples (triaxial). In addition to these experiments investigations on the deformation microstructure in the solid torsion samples were carried out using microscopical methods (optical microscopy, TEM).

The choice of the deformation modes emerged from the need of a systematically investigated set of samples made from the same material and covering the basic deformation modes, by going from uni-, through bi- to triaxial deformation (i.e. ranging from the least complex to the most complex deformation). Observations made in the past by various authors have in common that

- they relate only to one deformation mode (mostly uniaxial tension, the least complex case)
- they mostly consider only the sample surface and not the bulk
- they integrate over the whole sample without taking into account deformation gradients when making bulk measurements
- they mostly relate to measurements made only in two or three directions (e.g. axial and transverse direction in tensile deformation).

Techniques

The investigations on the uniaxially and biaxially deformed samples were performed by applying well-established energy and angular dispersive high energy x-ray diffraction techniques. These techniques are sufficient when investigating homogeneously deformed samples (i.e. no strain and texture gradients in the bulk).

It is known that solid torsion samples exhibit a radially dependent deformation and, therefore, a radially dependent texture and strain state, requiring a high spatial resoultion for their local observation. For these investigations a novel strain and texture scanning technique was successfully developed and applied. This technique combines, for the first time, a microfocussed high energy x-ray beam [Schul 1998], a newly developed conical slit system and a large area x-ray detector, allowing the

simultaneous monitoring of up to six independent Debye-Scherrer rings, emanating from the same local gauge volume. The microfocussed high energy beam combined with the appropriate method, actually allows the exploration of length scales in the µm range which are more than two orders of magnitude smaller than those accessible by neutron diffraction. The high photon flux and the penetration depth of the x-ray beam, in combination with the large area detector, permitted unprecedented radially resolved (in-situ) measurements of the local strain tensor and the local texture within solid torsion samples. Due to the fast data acquisition, it was possible also, for the first time, to observe simultaneously the evolution of the local strain tensor and the local texture in a dynamic in-situ deformation within a solid torsion sample. For the experimental data obtained by this technique a complete novel analysis software package was developed.

Texture

The uniaxially deformed AlMg3 samples showed, after compression, a 320 fibre texture [Ari 2001] and, after tension, a 111 / 100 fibre texture. The initial texture in both cases was a 111 / 100 fibre texture. In other words, after tension the deformation texture is similar to the initial one.

The intensity distributions measured for the biaxially deformed tubular AlMg3 torsion samples indicate the persisting dominance of the initial 111 / 100 fibre texture. Since these orientations are also part of the set of ideal orientations in the torsion texture, they are not expected to disappear. However, the intensity maxima in axial direction of the 111 reflection indicate a rotation of ideal orientation A in the sense of the shear.

The results from the radially resolved texture measurements on the solid AlMg3 torsion samples, deformed to a maximum of $\gamma = 3.5$, revealed a clear rotation in the sense of the shear of ideal orientation C. This rotation increases with increasing shear and starts at a deformation below $\gamma = 0.8$. The data indicates that prior to the rotation in the shear direction a counter shear rotation must have occurred. The partial A fiber is observed for lower deformations and becomes weaker with increasing deformation. Contrary to that, the D fibre, not present at low deformations, appears at high deformations in the 111 polefigures. An inversion, at $\gamma = 2.5$, of the dominance of the A^*_1 orientation over the A^*_2 orientation was observed in the 100

polefigures. Essentially, no evidence was found for the presence of the ideal orientation B. These results are in contrast to observations by other authors made at the surface of samples deformed in fixed end torsion [Mon 1984]. They reported the development of the B orientation and did not observe a D fibre in Al samples. Furthermore, their results on the sense of rotation of the C component do not coincide with the experimental results presented in this work. First simulations of the torsional deformation texture using the VPSC5 [Leb 1993] code showed the main features observed in the present experiment but also significant discrepancies which might be caused by the fact that the model does not take into account the deformation gradient within the sample, i.e. the coupeling between neighbouring grains that are subjected to a different deformation tensor.

Microstructure

The TEM investigations permitted the identification of three different deformation microstructures: Uniformly distributed dislocation tangles, first generation microband clusters and so-called chequerboard patterns. Though these types of microstructure are reported by various authors, their observations relate mostly to different deformation modes, such as rolling or tensile deformation. In cases, where results about the deformation microstructure due to torsion are published, the Al-alloy investigated had another composition, making direct comparisons difficult. However, a detailed microstructural analysis was beyond the scope of this work.

Crystallite microstrains

The hkl specific crystallite microstrains were determined as a function of the deformation and the radial position within the solid samples. A comparison of the results from the microstrain measurements on the AlMg3 samples, deformed uni-, bi-, and triaxially, showed large differences in the amount of observed crystallite microstrain. This is most significant for the 220 reflection. In the uniaxially deformed samples, the 220 crystal direction exhibited almost the weakest crystallite microstrains whereas, in the case of biaxial and triaxial deformation, they were the strongest, proving for the first time that the crystallite microstrain development in deformations of higher dimensionality is not negligible.

In the case of uniaxially deformed AlMg3 samples simulations by [Ari 2001] of the texture induced crystallite microstrain using a Taylor-Bishop-Hill-type model showed,

in general, a good agreement with the experimental data. From the strain measurements on the biaxially deformed AlSi25Cu4Mg1 sample it was concluded that, in this case, the crystallite microstrains were essentially zero.

Separation of crystallite microstrains

In the case of the solid AlMg3 torsion samples a separation of the experimentally determined crystallite microstrains into microstrains due to elastic interaction and microstrains due to plastic interaction was suggested. This separation is based on the simulation of the crystallite microstrains due to elastic interaction, using the Reuss model in combination with the ODF determined from the local texture measurements. The microstrains due to elastic interaction are about one order of magnitude smaller than the microstrains due to plastic interaction. Further investigations for selected cases permitted the identification of the grain orientations that are the most affected by the plastic deformation and, therefore, are most likely to cause the changes of the observed microstrain with increasing deformation.

Macrostrains

The high spatial resolution measurements on the solid torsion samples permitted the determination of the radially and deformation dependent pseudo macrostrain tensors. From these results the radially and deformation dependent approximate macrostrain tensors were calculated.

For the solid AlMg3 torsion sample the load strain tensor was determined in-situ at the highest deformation. The axial strain component is the most affected tensor component. At low deformation, large axial tensile residual strains at the sample center and compressive residual strains close to the sample surface were observed. The tensile strains can be explained by the tendency of the higher deformed regions to elongate. However, this elongation is constrained by the lower deformed, central regions, causing the axial strains. With increasing deformation the tensile strains become weaker which could be explained by the texture homegenization.

The calculation of the load torque from the load strain tensor yielded a value about 17% lower than the one measured with an externally applied strain gauge. This indicates that XECs obtained from tensile experiments or calculated with the common models (e.g. Kröner) are not directly applicable for multiaxial deformations. Similar findings were reported by [Bol 1967, Prü 1966].

The investigations on the solid AlSi25Cu4Mg1 torsion samples revealed that the axial strains almost tripled with doubled deformation. However, this is not directly in contradiction with the observations on the AlMg3 sample since the achievable maximum deformation for the AlSi25Cu4Mg1 samples was about ten times lower than the one for the AlMg3 samples. Therefore, the observations can be explained in such a way that the full evolution of the torsion texture, and, therefore, the development of axial strains, had not been achieved yet.

Intergranular strains

The determination of the macrostrains permitted the calculation of the radially and deformation dependent intergranular strains for the solid torsion samples. In the case of the sample made from AlMg3, the strongest intergranular strains and largest variations with increasing deformation were observed for the axial component. However, the similarity between respective intergranular strains at different deformations for a specific hkl is remarkable, also with respect to residual and load intergranular strains. As already observed for the crystallite microstrains, the 220 lattice planes exhibit also the largest values of intergranular strains. These findings differ from the observations of other authors [Pan 1998a] on the intergranular strains in tensile samples. They concluded from their experiments that the 220 lattice planes are the least affected by intergranular strains. Here, the 331 lattice planes were found to be the least affected and therefore represent well the macrostrain state.

Contrary to the observations on the AlMg3 sample, the intergranular strains in axial direction were the weakest, for the sample made of AlSi25Cu4Mg1. The 220 lattice planes showed the weakest and the 200 lattice planes exhibited the strongest, intergranular strains within the Al phase of the sample made of AlSi25Cu4Mg1. Moreover, from the measurements on this sample it could be concluded that the Si phase exhibits mostly large compressive intergranular strains while the Al phase shows tensile intergranular strains. The intergranular strains in the Si phase reached absolute values up to five times larger than the average intergranular strains in the Al phase.

The Swift effect

The development of axial forces due to large torsional deformation, also known as Swift effect, was measured on the solid torsion samples. The strongest axial forces

were observed for the samples made from AlMg3 at the lowest deformation $\gamma = 1.5$. With increasing deformation the axial forces became weaker. In the about ten times lower deformed AlSi25Cu4Mg1 samples, a strong increase of the axial forces with increasing deformation was observed. Assuming that the Al phase of the AlSi25Cu4Mg1 sample exhibits a similar behaviour as the AlMg3 alloy, in terms of the development of axial forces, it seems that the strongest axial forces evolve at the onset of the torsional deformation. This conclusion is corroborated by the dynamic in-situ observations on the deformation of an AlMg3 alloy torsion sample. The compressive strain observed in the axial direction indicates that the axial forces and, therefore, the sample elongation, are the strongest at around $\gamma = 0.35$. Above that deformation the axial forces decrease until about $\gamma = 1$ and then seem to start again to become stronger. The development of the axial forces seems to be closely linked to the strain evolution in the 220 crystal direction, the development of the A^*_1 / A^*_2 texture component, and the cw rotation of the C texture component.

The observations made show discrepancies to observations made by other authors on solid samples in fixed end torsion, integrating over the whole sample and measuring the texture only on the surface [Mon 1984, 1985]. These discrepancies are related to the presence / absence and rotation of ideal orientations (see above) and the relation between the axial forces and the amount of plastic deformation:

They observed the first maximum axial force at a deformation of about $\gamma = 0.9$ and a subsequent decrease of the force until $\gamma = 2.9$.

Outlook

- The limitations of the new strain and texture scanning technique for dynamic in-situ measurements occur mainly due to the detector characteristics, such as the size of the x-ray sensitive area, spatial distortion, PSF, readout time, and its price. In some cases (e.g. axial symmetry of the texture), it could be sufficient to monitor just a quarter of a diffraction ring. In this manner, the detector slit distance could be increased and therefore the sensitvity to 2Θ shifts improved.
- In the present work the strains were essentially measured on groups of grains. The next step, for a more detailed analysis of the plastic deformation, would be the determination of the strain tensor for single grains. This would finally

give access to the knowledge about the strain state in neighbouring grains, and the coupling between them. The knowledge of the strain tensor implies that the orientation of the single grains are known.

- Furthermore, future investigations could focus on the deformation at elevated temperatures. The new technique would allow the direct observation of texture and strain during the occurence of phenomena such as dynamic recrystallisation.
- Additional profile analyses combined, with the results on the crystallite microstrains and the intergranular strains, could contribute to a more thorough explanation of the observed phenomena.
- Future additional (destructive) investigations on the deformation microstructure could involve the mapping of the hardness of grain / subgrains in a sample cross section by nano-indentation. With additional TEM investigations, these results then could be linked to the observations on the radial dependent texture and strain and allow conclusions on the grain orientations, their deformation and their previous residual strain state.
- The determination of the ODF could be improved by measuring polefigures with a higher completeness.

7 REFERENCES

[Ack 1996] VAN ACKER, K.: *Internal stress states in cold worked metals and in metal matrix composites*, PhD thesis at Katholieke Universiteit Leuven, Belgium, 1996, pp. 219

[All 1985] ALLEN, A.J.; HUTCHINGS, M.T.; WINDSOR, C.G.: *Neutron diffraction methods for the study of residual stress fields*, Advances in Physics, Vol. 34, No. 4, 1985, pp. 445-473

[All 1989] ALLEN, A.J.; BOURKE, M.; DAVID, W.I.F.; DAWES, S.; HUTCHINGS, M.T.; KRAWITZ, A.D.; WINDSOR, C.G.: *Effects of elastic anisotropy on the lattice strains in polycrystalline metals and composites measured by neutron diffraction*, Proc. ICRS2, 23-25 Nov. 1988, Nancy, France, G. Beck (ed.), Elsevier, London, UK 1989, pp. 78-83

[Ari 2000a] ARIS, S.: *Simulation von Textur und texturbedingten Kristallitmikrodehnungen kubischer Werkstoffe und Vergleich mit experimentellen Daten*, PhD thesis at Technische Universität Berlin, 2000

[Ari 2000b] ARIS S., MARTINS R.V., MERINO J., PYZALLA A., *Simulation of Deformation Textures and Crystallite Microstrains of Cubic Metals and Comparison to Experimental Results*, Proceedings Materials Week, Munich (2000)

[Bac 1950] BACKOFEN, W.A.: *The torsion texture of copper*, J. Metals, Transactions AIME, 1950, 188, pp. 1454 1458

[Bacz 1996] BACZYNSKI, J.; JONAS, J.J.: *Texture Development During the Torsion Testing of α-Iron and Two IF Steels,* Acta mater., Vol. 44, No. 11, 1996, pp. 4273-4288

[Bay 1992] BAY, B.; HANSEN, N.; HUGHES, D.A.; KUHLMANN-WILSDORF, D.: *Evolution of f.c.c. Deformation Structures in Polyslip*, Acta metall mater., Vol. 40, No. 2, 1992, pp. 205-219

[Beh 1991] BEHNKEN, H.; HAUK, V.: *Berechnung der röntgenographischen Spannungsfaktoren texturierter Werkstoffe - Vergleich mit experimentellen Ergebnissen,* Z. Metallkde., Bd. 82, 1991, pp. 151-158

[Bev 1992] BEVINGTON, P.R.; ROBINSON, D.K.: *Data Reduction and Error Analysis for the Physical Sciences*, New York, 1992[2]

[Bis 1951a] BISHOP, J.F.W.; HILL, R.: *A Theory of the Plastic Distortion of a Polycrystalline Aggregate under Combined Stresses*, Phil. Mag., ser. 7, **42**, 1951, 414-427

[Bis 1951b] BISHOP, J.F.W.; HILL, R.: *A Theoretical Derivation of the Plastic Properties of a Polycrystalline Face-Centered Metal*, Phil. Mag., ser. 7, **42**, 1951, 1298-1307

[BM16] http://www.esrf.fr/exp_facilities/ID16/handbook/handbook.html

[Bol 1967] BOLLENRATTH, F.; FRÖHLICH, W.; HAUK, V.: *Messung von Spannungen und Eigenspannungen mittels Röntgenstrahlen an Torsionsstäben aus verschiedenen Stählen*, Materialprüf., **9**, (1967) Nr. 11, pp. 406-411

[Brag 1913] BRAGG, W.H.; BRAGG, W.L: *The reflection of x-rays by crystals*, Proc. Roy. Soc., 88A, London, 1913, pp. 246-248

[Bra 1983] BRAKMANN, C.M.: *Residual Stresses in Cubic Materials with Orthorhombic or Monoclinic Specimen Symmetry: Influence of Texture on ψ Splitting and Non-linear Behaviour*, J. Appl. Cryst., 16, 1983, pp. 325-340

[Bun 1969] BUNGE, H.J.: *Mathematische Methoden der Texturanalyse*, Akademie-Verlag, Berlin 1969

[Bun 1982] BUNGE, H.J.: *Texture analysis in materials science*, Butterworths, London 1982

[Bun 1997] BUNGE, H.-J.: *X-ray texture analysis in materials and earth sciences*, Eur. J. Mineral., **9**, Nr. 4, 1997, pp. 735-761

[Can 1982] CANOVA, G.R.; SHRIVASTAVA, S.; JONAS, J.J.; G'SELL, C.: *The Use of Torsion Testing to Assess Material Formability*, Formability of Metallic Materials, 2000 A.D. American Society for Testing and Materials, ASTM-STP 753 (1982) 189-210

[Can 1984] CANOVA, G.R.; KOCKS, U.F.; JONAS, J.J.: *Theory of Torsion Texture Development*, Acta metall., Vol. 32, No. 2, 1984, pp. 211-226

[Cha 1995] CHANG, C.H.; KOO, Y.M.: *X-Ray Measurements of Lattice Strains in Textured Low Carbon Steel under Uniaxial Loading*, Metallurgical and Materials Transactions A, 26A, 03/1995, 629-632

[Cla 1998] CLAUSEN, B.; LORENTZEN, T.; LEFFERS, T.: *Self-consistent modelling of the plastic deformation of f.c.c. polycrystals and its implications for diffraction measurements of internal stresses*, Acta mater., Vol. 46, No. 9, 1998, pp. 3087-3098

[Cra 1959] CRANDALL, S.H.; DAHL, N.C.: *Introduction to the mechanics of solids*, McGraw-Hill, New York 1959

[Daw 2001] DAWSON, P.; BOYCE, S.; MACEWEN, S; ROGGE, R.: *On the influence of crystal elastic moduli on computed lattice strains in AA-5182 following plastic straining*, Materials Science and Engineering A, 313, 2001,pp. 123-144

[Day 2000] DAYMOND, M.R.; TOMÉ, C.N.; BOURKE, M.A.M.: *Measured and Predicted Intergranular Strains in Textured Austenitic Steel*, Acta mater. 48 (2000) 553-564

[Del 1982] DELHEZ, R.; DE KEIJSER, TH.H.; MITTEMEIJER, E.J.: *Determination of Crystallite Size and Lattice Distortions through X-Ray Diffraction Line Profile Analysis*, Fresenius Z. Anal Chem, 312, 1982, pp. 1-16

[DIN 1977] DIN ISO 1352: *Steel - Torsional Stress Fatigue Testing*, Beuth Verlag GmbH, Berlin 1977

[DIN 1978] DIN 50106: *Prüfung metallischer Werkstoffe - Druckversuch*, Beuth Verlag GmbH, Berlin 1978

[DIN 1991] DIN 50125: *Prüfung metallischer Werkstoffe - Zugproben*, Beuth Verlag GmbH, Berlin 1991

[DIN 1998] DIN EN 10002: *Metallische Werkstoffe - Zugversuch*, Beuth Verlag GmbH, Berlin 1998

[Dir 1995] DIRRAS, G.F.; BIGET M.-P.; REY, C.: *On the microstructural evolution of cold-rolled Al+5at.%Mg*, Scripta Metall. et Mater., Vol. 33, No. 5, 1995, 755-760

[Döl 1976] DÖLLE, W.; HAUK, V.; MEURS, P.; SESEMANN, H.: *Eigenspannungen nach einachsiger Zugverformung kubisch-flächensentrierter Metalle untersucht an Kupfer unterschiedlicher Verformung und an der Nickel-Kupfer Legierung NiCu30Fe*, Z. Metallkde., 67, 1976, pp. 30-35

[Dri 1978] DRIESEL, W.; FISCHER, K.-F.; PUFF, M.: *Untersuchungen zur Formierung einer <110>-Fasertexture bei gestauchten Aluminiumzylinderproben*, Neue Hütte, 23, 1978, pp. 467-469

[Dub 1990] *Taschenbuch für den Maschinenbau* / Dubbel: Hrsg. BEITZ, W., KÜTTNER, K.-H., Berlin u.a., 1990[17]

[Dul 1996] DULY, D.; BAXTER, G.J.; SHERCLIFF, H.R.; WHITEMAN, J.A.; SELLARS, C.M.; ASHBY, M.F.: *Microstructure and Local Crystallographic Evolution in an Al-1wt%Mg Alloy Deformed at Intermediate Temperature and High Strain-Rate*, Acta Mater. Vol. 44, No. 7, 1996, 2947-2962

[Esh 1957] ESHELBY, J.D.: *The determination of the elastic field of an ellipsoidal inclusion, and related problems*, Proc. Roy. Soc. London A, 241, 1957, pp. 376-396

[Fie 1957] FIELDS, JR., D.S.; BACKOFEN, W.A.: *Determination of Strain-Hardening Characteristics by Torsion Testing*, Proceedings, American Society for Testing Materials, Vol. 57, 1957, pp. 1259-1272

[Gen 1999] GENZEL, C.: Private communication

[Gil 1975] GIL-SEVILLANO,J.; VAN HOUTTE, P.; AERNOUDT, E.: *Deutung der Schertexturen mit Hilfe der Taylor-Analyse*, Z. Metallkunde, Bd. 66, H. 6 (1975) 367-373

[Gila 1994] GILAT, A.; WU, X.; ZHANG, X.T.; BATRA, R.C.: *Dynamic hot forging of a steel connecting rod*, Journal de Physique IV, C8, 4, 1994, pp. C8-533-537

[Ham 1996] HAMMERSLEY, A.P.; SVENSSON, S.O.; HANFLAND, M.; FITCH, A.N.; HÄUSERMANN, D.: *Two-Dimensional Detector Software: From Real Detector to Idealised Image or Two-Theta Scan*, High Pressure Research, Vol. 14, 1996, 235-248

[Hau 1990] HAUK, V.; NIKOLIN, H.-J.; PINTSCHOVIUS, L.: *Evaluation of deformation residual stresses caused by uniaxial plastic strain of ferritic and ferritic-austenitic steels*, Z. Metallkde., 81, 1990, pp. 556-569

[Hau 1991] HAUK, V.: *Die Bestimmung der Spannungskomponente in Dickenrichtung und der Gitterkonstante des spannungsfreien Zustandes*, Härterei-Tech. Mitt., 46, 1991, pp. 52-59

[Hau 1997] HAUK, V.: *Structural and Residual Stress Analysis by Nondestructive Methods*, Amsterdam, 1997

[He 1998] HE,B.B.; SMITH, K.L.: *Fundamental Equation of Strain and Stress Measurement Using 2D Detectors*, Proceedings SEM Spring Conf. on experimental and applied mechanics, Houston, Texas, June 1-3, 1998, pp. 217-220

[Hol 1997] HOLDEN, T.M.; CLARKE, A.P.; HOLT, R.A.: *Neutron Diffraction Measurements of Intergranular Strains in MONEL-400*, Metallurgical and Materials Transactions A, Vol. 28A, 1997, pp. 1-12

[Hon 1979] HONNEFF, H.; MECKING, H.: *A method for the determination of the active slip systems and orientation changes during single crystal deformation*, Proc. ICOTOM 5, Aachen, Germany 1978, **1**, 1979, pp. 265-275

[Hou 1976] VAN HOUTTE, P.; AERNOUDT, E.: *Considerations on the Crystal and the Strain Symmetry in the Strain Symmetry in the Calculation of Deformation Textures with the Taylor Theory*, Materials Science and Engineering, **23**, 1976, pp. 11-22

[Hou 1981] VAN HOUTTE, P.: *Adaptation of the Taylor theory to the typical substructure of some cold rolled fcc metals*, Proc. ICOTOM 6, Tokyo, Japan 1981, pp. 428-433

[Hou 1993] VAN HOUTTE, P.; DE BUYSER, L.: *The Influence of Crystallographic Texture on Diffraction Measurements of Residual Stress*, Acta metall. mater., Vol. 41, No. 2, 1993, pp. 323-336

[Hug 1993] HUGHES, D.A.: *Microstructural Evolution in a Non-Cell Forming Metal: Al-Mg*, Acta metall. mater., Vol. 41, No. 5, 1993, 1421-1430

[Hug 2000] HUGHES, D.A.; LEBENSOHN, R.A.; WENK, H.R., KUMAR, A.: *Stacking fault energy and microstructure effects on torsion texture evolution*, Proc. R. Soc. Lond. A, **456**, 2000, pp. 921-953

[Hugh 1952] HUGHES, D.E.R.: *The Hot-Torsion Test for Assessing Hot-Working Properties of Steels*, J. Iron and Steel Institute, March 1952, pp. 214-220

[Hut 1970] HUTCHINSON, J.W.: *Elastic-Plastic Behaviour of Polycrystalline Metals and Composites*, Proc. R. Soc. London A, 319, 1970, p. 247

[ID11] http://www.esrf.fr/exp_facilities/ID11/handbook/

[ID15A] http://www.esrf.fr/exp_facilities/ID15A/handbook/handbook.html

[Jon 1993] JONAS, J.J.: *Modelling the Length Changes that Take Place During Torsion Testing*, Int. J. Mech. Sci., 35, 1993, pp. 1065-1077

[Juu 2000] JUUL JENSEN, D.; KVICK, Å; LAURIDSEN, E.M.; LIENERT, U.; MARGULIES, L.; NIELSEN, S.F.; POULSEN, H.F.: *Plastic Deformation and Recrystallization Studied by the 3D X-Ray Microscope*, Mat. Res. Soc. Symp. Proc. Vol. 590 (2000) 227-240

[Kas 1989] KASSNER, M.E.; MYSHLYAEV, M.M.; MCQUEEN, H.J.: *Large-strain Torsional Deformation in Aluminum at Elevated Temperatures*, Materials Science and Engineering, A108, 1989, pp. 45-61

[Koc 1981] KOCKS, U.F.; CANOVA, G.R.: *How many slip systems and which?*, In: Proc. 2nd Risø Int. Symp. Metall. Mater. Sci., Risø, Denmark, 1981, HANSEN, N.; HORSEWELL, A.; LEFFERS, T.; LILHOLT, H. (Eds.), Risø Nat. Lab., Roskilde 1981, pp. 35-44

[Koc 1998] KOCKS, U.F.; TOMÉ, C.N.; WENK, H.-R.: *Texture and Anisotropy*, Cambridge, 1998

[Kor 1986] KORBEL, A.; MARTIN, P.: *Microscopic Versus Macroscopic Aspect of Shear Bands Deformation*, Acta metall., Vol. 34, No. 10, 1986, 1905-1909

[Krö 1958] KRÖNER, E.: *Berechnung der elastischen Konstanten de Vielkristalls aus den Konstanten des Einkristalls*, Z. Physik, 151, 1958, pp. 504-518

[Lal 1974] LALLEMENT, G.; OYTANA, C.: *Étude physique des variations de longueur avec la torsion des métaux*, Rheol. Acta, 13, 1974, pp. 467-476

[Lan 1] *Landolt-Börnstein: Numerical Data and Functional Relationships in Science and Technology*, 6th Ed. IV/2-Material Values and Mechanical Behaviour of Metallic Industrial Materials Part a-c, BORCHERS, H.; SCHMIDT, E. (Eds), Springer-Verlag, Berlin, 1963-1965

[Leb 1993] LEBENSOHN, R.A.; TOMÉ, C.N.: *A Self-Consistent Anisotropic Approach for the Simulation of Plastic Deformation and Texture Development of Polycrystals: Application to Zirconium Alloys*, Acta metall. mater., Vol. 41, No. 9, 1993, pp. 2611-2624

[Lie 2000a] LIENERT, U., POULSEN, H.F., MARTINS, R.V., KVICK. Å.: *A High Energy Microscope for Local Strain Measurements within Bulk Materials*, Proceedings of the ECRS-5 conference, 28-30 Sept. 1999, (Noordwijkerhout, The Netherlands), ed. Böttger, A.J., Delhez, R., and Mittemeijer, E.J., Mat. Sci. Forum Vols. 347-349, 2000, pp. 95-100

[Lie 2000b] LIENERT U., GRIGULL S., KVICK Å., MARTINS R.V., POULSEN H.F.: *Three Dimensional Strain Measurements in Bulk Materials with high Spacial Resolution*, Proc. ICRS-6, Oxford, United Kingdom (2000), Vol. 2, 1050-1057

[Lie 2000c] LIENERT U., MARTINS R., GRIGULL S., PINKERTON M., POULSEN H.F., KVICK Å., *High spatial resolution strain measurements within bulk materials by slit-imaging*, Mat. Res. Soc. Symp. Proc. Vol. 590 (2000), pp. 241-246

[Lie 2000d] LIENERT, U.: private communication, november 2000

[Lie 2001] LIENERT, U.; POULSEN, H.F.; KVICK, Å.: *Mesoscale structural characterization within bulk materials by high-energy x-ray microdiffraction*, AIAA Journal, 39, (5), 2001, pp. 919-923

[Mac 1961] MACHERAUCH, E.; MÜLLER, P.: *Das $\sin^2\psi$-Verfahren der röntgenographischen Spannungsmessung*, Z. f. angew. Phys., 13, 1961, p. 305

[Mac 1973] MACHERAUCH, E.; WOHLFAHRT, H.; WOLFSTIEG, U.: *Zur zweckmäßigen Definition von Eigenspannungen*, Härterei-Technische-Mitteilungen, Band 28, Heft 3, 1973, p. 201-211

[Marga 1986] MARGARITONDO, G.: *Introduction to synchrotron radiation*, Oxford University Press, Oxford (UK) 1986

[Marg 2001] MARGULIES, L.; WINTHER, G.; POULSEN, H.F.: *In Situ Measurement of Grain Rotation During Deformation of Polycrystals*, Science, 291, 2001, pp. 2392-2394

[Mart 1998] MARTINS, R.V.: *Entwurf und Inbetriebnahme einer Torsions- und Heizvorrichtung zur in-situ Spannungsanalyse in einem Neutronendiffraktometer*, diploma thesis, Technische Universität Berlin, 1998

[Mart 1999] MARTINS R.V., KVICK Å., LIENERT U., POULSEN H.F., PYZALLA A., *High energy synchrotron strain scanning on highly plastically deformed torsion samples*, Proceedings of the 20th Risø International Symposium on Materials Science, Risø Nat. Lab., Roskilde, Denmark (1999) 411-416

[Mart 2000] MARTINS R.V., LIENERT U., MARGULIES L., PYZALLA A., *Residual strain tensor determination within highly plastically deformed torsion samples using high energy synchrotron radiation*, Proc. Meca-Sens, Reims 2000, France, J. Neutron Research, 9, pp. 249-254

[Mat 1982] MATTHIES, S.; VINEL, G.W.: Phys. Status Solidi B, 112, 1982, K111-120

[Mon 1984] MONTHEILLET, F.; COHEN, M.; JONAS, J.J.: *Axial Stresses and Texture Development during the Torsion Testing of Al, Cu and α-Fe*, Acta metall., Vol. 32, No. 11, 1984, pp. 2077-2089

[Mon 1985] MONTHEILLET, F.; GILORMINI, P.; JONAS, J.J.: *Relation between Axial Stresses and Texture Development during Torsion Testing: A Simplified Theory*, Acta metall., Vol. 33, No. 4, 1985, pp. 705-717

[Mül 1999] MÜLLER, K.B., WINSEMANN, U., Aluminium 75 (1999), 4, pp. 314-320, (part 1) and Aluminium 75 (1999), 6, pp. 531-536 (part 2)

[Mug 1983] MUGHRABI, H.: *Dislocation wall and cell structures and long-range internal stresses in deformed metal crystals*, Acta metall., 31, 1983, pp. 1367-1379

[Nak 1987] NAKAYAMA, Y.; MORII, K.: *Microstructure and Shear Band Formation in Rolled Single Crystals of Al-Mg Alloy*, Acta metall., Vol. 35, No. 7, 1987, 1747-1755

[Neu 1993] *Neutron and Synchrotron Radiation for Cindensed Matter Studies*, Vol I, BARUCHEL, J.; HODEAU, J.L.; LEHMANN, M.S.; REGNARD, J.R.; SCHLENKER, C.,(Eds.), Springer/Les Éditions de Physique, Les Ulis 1993

[Nie 2000] NIELSEN, S. F.; WOLF, A.; POULSEN, H. F.; OHLER, M.; LIENERT, U.; and OWEN, R. A.: *A conical slit for three-dimensional XRD mapping*,J. Synchrotron Rad., 7, 2000, 103-109

[Nin 1994] NING, J.; AIFANTIS, E.C.: *On anisotropic finite deformation plasticity, Part II., A two-component model*, Acta Mechanica, **106**, 1994, pp. 73-85

[Noy 1987] NOYAN, I.C.;COHEN, J.B.: *Residual Stress. Measurement by Diffraction and Interpretation*, Berlin, 1987

[Nye 1985] NYE, J.F.: *Physical Properties of Crystals*, Oxford 1985[2], Oxford University Press

[Pan 1997] PANG, J.W.L.; HOLDEN, T.M.; MASON, T.E.: *In Situ Generation of Intergranular Strains in Zircaloy under Uniaxial Loading*, Proc. ICRS 5, 16-18 june 1997, Linkøping, Sweden 1997, pp. 610-615

[Pan 1998a] PANG, J.W.L.; HOLDEN, T.M.; MASON, T.E.: *In Situ Generation of Intergranular Strains in an Al7050 Alloy*, Acta. mater., **46**, No. 5 (1998), 1503-1518

[Pan 1998b] PANG, J.W.L.; HOLDEN, T.M.; MASON, T.E.: *The development of intergranular strains in a high strength steel*, J. Strain Analysis, 33, 5, 1998, pp. 373-383

[Pan 1999] PANG, J.W.L.; HOLDEN, T.M.; TURNER, P.A.; MASON, P.E.: *Intergranular stresses in Zircaloy-2 with rod texture*, Acta metall., 47, 1999, pp. 373-383

[Pea 1994] material data sheets, Peak Werkstoff GmbH, 1994

[Pet 1994] PETZOW, G.: *Metallographisches Ätzen*, Stuttgart, 1994[6]

[Por 1970] PORTEVIN, P.A.: *étude de l'influence du chrome sur la forgeabilité d'aciers à 0,07 - 0,08 % C*, Revue Métall., 67, 1970, 761-774

[Pou 2001] POULSEN, H.F.; JUUL JENSEN, D.; TSCHENTSCHER, T.; WCISLAK, E.M.: *Quantification of minority texture components by high energy x-rays*, Textures and Microstructures, Vol. 35, nr. 1,2001, pp. 39-54

[Poy 1912] POYNTING, J.H.: *On the Changes in the Dimensions of a Steel Wire when Twisted, and on the Pressure of Distortional Waves in Steel*, Proc. Roy. Soc., A 86, 1912, pp. 534-561

[Pre 1992] PRESS, W.H.;FLANNERY, B.P.;TEUKOLSKY, S.A.;VETTERLING, W.T.: *Numerical recipes in C*, Cambridge 1992

[Prü 1966] PRÜMMER, R; MACHERAUCH, E.: *Die Auswirkung der elastischen Anisotropie auf die röntgenographische Spannungsmessung an Stahlproben*, J. Soc. of Materials Science, 15, Japan, 1996, pp. 45-50

[Pyz 2000a] PYZALLA, A.: *Methods and Feasibility of Residual Stress Analysis by High-Energy Synchrotron Radiation in Transmission Geometry Using a White Beam*, J. Nondestructive Eval., Vol. 19, No. 1, 2000, pp. 21-31

[Pyz 2000b] PYZALLA, A., MÜLLER, K.B., WEGENER, J.: *Influence of Extrusion Parameters on the Microstructure and Properties of an Al-Si Alloy*, Z. Metallkd., 91, 2000, 10, pp. 831-837

[Pyz 2000c] PYZALLA, A.; BRODMANN, M.; LEE, P.L.; HAEFFNER, D.: *Microstructure, texture and residual microstrains in MgAl8Zn deformed at very high strain rates*, Magnesium alloys and their applications 2000, Wiley-VCH 2000, pp. 125-130

[Pyz 2001] PYZALLA, A.: *Analyse stark plastisch verformter Werkstoffe mit Beugungsverfahren*, Habilitation, Ruhr-Universität Bochum, 2001

[Reu 1929] REUSS, A.: *Berechnung der Fließgrenze von Mischkristallen auf Grund der Plastizitätsbedingung für Einkristalle*, Z. Angew. Math. u. Mech., **9**, 1,1929, pp. 49-58

[Rei 1999] REIMERS, W.; PYZALLA, A.; BRODA, M.; BRUSCH, G.; DANTZ, D.; SCHMACKERS, T.: *The use of high energy synchrotron radiation for residual stress analyses*, J. Mat. Sci. Letters, 18, 1999, pp. 581-583

[Roe 1965] ROE, R.J.: *Description of Crystallite Orientation in Polycrystalline Materials, General Solution to Polefigure Inversion*, J. Appl. Phys., 36, 1965, pp. 2024-2031

[Ron 1967] RONAY, M.: *On Second-Order Strain Accumulation in Aluminum in Reversed Cyclic Torsion at Elevated Temperatures*, Int. J. Solids Structures, Vol. 3, 1967, pp. 167-176

[Ros 1968] ROSE, W.; STÜWE, H.-P.: *Der Einfluß der Textur auf die Längenänderung im Torsionsversuch*, Z. Metallkde, **59**, 1968, pp. 396-399

[Sac 1928] SACHS, G.: *Zur Ableitung einer Fließbedingung*, Zeitschrift d. VDI, Bd. 72, Nr. 22, 1928, 734-736

[Sch 1935] SCHMID, E.; BOAS, W.: *Kristallplastizität*, Springer Verlag, Berlin 1935

[Schul 1998] SCHULZE, C.; LIENERT, U.; HANFLAND, M.; LORENZEN, M.; ZONTONE, F.: *Microfocusing of hard X-rays with cylindrically bent crystal monochromators*, J. Synchrotron Rad., 5, 1998, pp. 77-81

[Schu 1991] SCHUMANN, H.: *Metallographie*, Leipzig, 1991[13]

[Schw 1991] SCHWARZER, R.A.: *Texture Analysis by Electron Dffraction*, Steel Research, 62, 1991, pp.-542-547

[Shr 1982] SHRIVASTAVA, S.C.; JONAS, J.J.; CANOVA, G.: *Equivalent strain in large deformation torsion testing: Theoretical and practical considerations*, J. Mech. Phys. Solids, Vol. 30, No. 1/2, 1982, pp. 75-90

[Swi 1947] SWIFT, H.W.: *Length changes in metals under torsional overstrain*, Engineering, 163, 1947, pp. 253-257

[Tay 1938] TAYLOR, G.I.: *Plastic Strain in Metals*, J. Inst. Met., **62**, 1938, 307-324

[Tom 1991] TOMÉ, C.N.; LEBENSOHN, R.A.; KOCKS, U.F.: *A Model for Texture Development Dominanted by Deformation Twinning: Application to Zirconium Alloys*, Acta mettal. mater., Vol. 39, No. 11, 1991, pp. 2667-2680

[Tom 1997] TOMÉ, C.N.; HOLDEN, T.M.; TURNER, P.A.; LEBENSOHN, R.A.: *Interpretation of intergranular stress measurements in Monel-400 using polycrystal models*, Proc. ICRS 5, 16-18 june 1997, Linkøping, Sweden 1997, pp. 40-45

[Tót 1992] TÓTH, L.S.; JONAS, J.J.; DANIEL, D.; BAILEY, J.A.: *Texture Development and Length Changes in Copper Bars Subjected to Free End Torsion*, Textures and Microstructures, Vol. 19, 1992, pp. 245-262

[Ver 1998] VERDIER, M.; JANECEK, M.; BRÉCHET, Y.; GUYOT, P.: *Microstructural evolution during recovery in Al-2.5%Mg alloys*, Materials Science and Engineering, A248 (1998), 187-197

[Voi 1928] Voigt, W.: Lehrbuch der Kristallphysik, Nachdruck, 1. Auflage, Teubner, Berlin/Leipzig 1928

[Wan 2000] WANNER, A; DUNAND,D.C.: *Synchrotron X-Ray Study of Elastic Phase Strains in the Bulk of an Externally loaded Cu/Mo Composite*, Mat. Res. Soc. Proc. Vol. 590 (2000)

[Was 1962] WASSERMANN, G.; GREWEN, J.: *Texturen metallischer Werkstoffe*, Springer, Berlin 1962

[Web 1998] WEBSTER, P.J.; VAUGHAN, G.B.M.; MILLS, G.; KANG, W.P.: *High Resolution Synchrotron Strain Scanning at BM16 at the ESRF*, Mat. Sc. Forum, Vols. 278-281, 1998, pp. 323-328

[Weg 2001] WEGENER, J.: *Mikrostruktur, Textur und Eigenspannungen von stranggepressten und reibrührgeschweißten aushärtbaren Aluminiumlegierungen*, PhD thesis at Technische Universität Berlin, 2001

[Wen 1985] WENK, H.R.: *Preferred orientation in deformed metals and rocks: An introduction to modern texture analysis*, Academic Press, New York (USA) 1985

[Wen 1998] WENK, H.-R.; MATTHIES, S.; DONOVAN, D.; CHATEIGNER, D.: *BEARTEX: a Windows-based program system for quantitative texture analysis*, J. Appl. Cryst., **31**, 1998, pp. 262-269

[Wit 1980] WITZEL, W.; HEMMINGER, W.: *Torsions-Wechselverformung von rekristallisiertem Kupfer bis zu großen Gesamtverformungen*, Z. Metallkunde, Bd. 71 (1980) H. 9, 599-604

[Wit 1982a] WITZEL, W.: *Warmtorsionsversuche mit Reinaluminium (I)*, Aluminium, **58**, Heft 10, Okt. 1982, pp. 588-592

[Wit 1982b] WITZEL, W.: *Warmtorsionsversuche mit Reinaluminium (II)*, Aluminium, **58**, Heft 11, Okt. 1982, pp. 664-669